Plasma Enhanced Atomic Layer Deposition of Thin Film YSZ Electrolytes

by

Wenfei Zhang

A thesis submitted in partial fulfillment of the requirements for the degree of

Doctor of Philosophy

in

Materials Engineering

Department of Chemical and Materials Engineering
University of Alberta

Abstract

In order to keep the performance of solid oxide fuel cells (SOFCs) at intermediate operating temperature range (500℃ - 700℃), thin and fully dense yttria-stabilized zirconia (YSZ) electrolytes are desired to provide shorter oxygen ion transport distance and prevent fuel crossover and internal currents losses. Atomic layer deposition (ALD) is one of the promising fabrication candidates, yielding conformal and pin-hole free thin films due to its self-saturation reaction. For YSZ thin films, Y_2O_3 concentration, grain size, thickness, and ALD recipe setup are critical to their conductivity. All reported studies in the literature used the ALD recipe with various Y_2O_3 and ZrO_2 ALD cycles in one ALD super-cycle to manipulate the Y_2O_3 concentrations. With this method, annealing is required to homogenize the distribution of Y_2O_3, during which the properties of thin films are possibly compromised. A recipe with both yttrium and zirconium precursor pulses in one ALD cycle was developed in this study. Plasma enhanced ALD (PEALD) YSZ thin films using tetrakis-dimethylamido zirconium ($Zr(NMe_2)_4$), Tris(methylcyclopentadienyl)yttrium ($Y(MeCp)_3$) and oxygen gas as precursors were grown on p-type Si(100) at 150℃. Several characterization techniques, including in-situ spectroscopic ellipsometry (i-SE), X-ray photoelectron spectroscopy (XPS), X-ray diffraction (XRD), atomic force microscopy (AFM), and four-point conductivity measurements were utilized to characterize the

optical, chemical, morphological and electrical performance of the YSZ electrolyte thin films. As-deposited YSZ thin films were dense and with high refractive indices (2.15 to 2.3 at 550nm), showing an outstanding oxygen ionic conductivity (0.2 S/cm at 600℃) with low activation energy (0.98 eV obtained from 400℃ to 600℃). The true size effect was considered to be responsible, introducing the intrinsic modification of the local physical properties in the vicinity of the grain boundaries. The true size effect was compromised due to the coarse grains of thick YSZ thin films, and consequently they exhibited poorer conductivity. From the results it has been found that the ALD recipe setup affects the structural and electrical properties of YSZ thin films. Annealing improved the conductivity of samples using YOZO and ZOYO recipes due to the homogenization of Y_2O_3 distribution. However, the conductivity of samples using YZO and ZYO recipes decreased after annealing because of the weakened true size effect.

To my wife, Yajing, who has always been there supporting me and inspiring me to do better.

And to my parents, Xiaolin and Xiaoping, and to my brother, Wenjin.

Acknowledgments

First and foremost I would like to thank my supervisors, Dr. Ken Cadien, and Dr. Jingli Luo. This thesis would have never come to existence without the support from them. Working under their supervision has been a wonderful experience and an excellent opportunity to learn from their expertise, insights and attitude towards research. I would also like to thank the examining committee members, Dr. Douglas Ivey and Dr. Sean Barry for their constructive comments on my thesis. I would like to extend my gratitude to Dr. Hongbo Zeng and Dr. Hyun-Joong Chung for their advice on my candidacy report.

I am grateful to Dr. Triratna Muneshwar and Dr. Amir Afshar for their encouragement and support. I would like to thank Dr. Bin Hua for his help with the electrical test. I also would like to thank my other fellow colleagues, especially Mengmeng Miao, Korel Dawkins, Hamidreza Pirayesh, Michael Clark, Elham Rafie, Yaqian Zhang and Subiao Liu, for many insightful discussions and ideas.

I would like to thank Dr. Shihong Xu, Dr. Nancy Zhang, Dr. Anqiang He, and Stephanie Bozic from nanoFab for their help and assistance on materials characterization.

Table of Contents

List of Tables

List of Figures

List of Symbols and Abbreviations

SOFCs: Solid Oxide Fuel Cells

YSZ: Yttria Stabilized Zirconia

8YSZ: YSZ with 8 mol% Y_2O_3

10YSZ: YSZ with 10 mol% Y_2O_3

3YSZ: YSZ with 3 mol% Y_2O_3

ALD: Atomic Layer Deposition

CVD: Chemical Vapor Deposition

PEALD: Plasma-enhanced ALD

OCV: Open Circuit Voltage

IT-SOFCs: Intermediate-temperature SOFCs

i-SE: In-situ Spectroscopic Ellipsometery

MSE: Mean Square Error

GPC: Growth Per Cycle

XPS: X-Ray Photoelectron spectroscopy

XRD: X-Ray Diffraction

AFM: Atomic Force Microscopy

SCL: Space Charge Layer

EIS: Electrochemical Impedance Spectroscopy

DFT: Density Function Theory

VASP: Vienna Ab initio Simulation Package

Chapter 1

Introduction

1.1 Background

With the increasing degradation of the environment due to carbon dioxide emissions, the development and adoption of clean energy is increasingly important and urgent. A fuel cell is an energy conversion device which converts chemical energy of fuels directly into electrical energy without combustion, showing a much more efficient conversion compared with other methods. Solid oxide fuel cells (SOFCs) have emerged as a promising candidate for high efficiency fuel cells, outstanding fuel flexibility, and long life expectancy [1].

The electrolyte is one essential component of SOFCs. Its main functions include preventing the two electrodes (anode and cathode) from electronic contact and providing an oxygen ion or proton transport path to keep the overall electrical balance [2]. Yttria stabilized zirconia (YSZ) is one of the most commonly used electrolyte materials for oxygen ionic transport. YSZ with 8 mol% Y_2O_3 (8YSZ) has been found to exhibit the highest oxygen ionic conductivity due to the stabilization of the cubic phase of zirconia. The fluorite structure of this cubic phase exhibits good oxygen ionic conductivity due to its high capacity for oxygen vacancies at tetrahedral sites[1].

Atomic layer deposition (ALD) is derivative of chemical vapor deposition (CVD). During ALD, precursors are introduced into the reaction chamber independent of each other to prevent any gas phase reaction and to limit the reactions to the surface of the substrate [3]. The major advantage of ALD is the deposition of conformal and pin-hole free thin films. According to the functions of electrolyte materials mentioned above, ALD is a promising candidate fabrication technique. Furthermore, the high conformity and thin ALD electrolyte films provide a possibility of operating SOFCs in a lower temperature, with the benefits of longer lifetime, and lower cost with the possibility of using cheaper construction materials [1].

1.2 Objectives of This Work

The use of ALD thin YSZ films for SOFC electrolytes has been studied in literature [4-6]. However, as the thickness of YSZ decreases to nanometer scale, the effects of grain size, grain boundary, thickness, and the yttrium oxide concentration in YSZ on oxygen ionic conductivity are still contentious.

In this thesis, an in-depth study of thin film YSZ fabricated by plasma-enhanced ALD (PEALD) is presented. The main research goals are:

- Develop a novel yttrium oxide PEALD process that enables low % yittria compositions by using a low vapor pressure precursor.

- Develop the ALD recipe parameters for YSZ and study the effect of recipe variations on its ionic conductivity.
- Identify the effect of yttrium oxide concentration in nanocrystalline YSZ thin films on oxygen ionic conductivity for the intermediate temperature range (400°C - 600°C).
- Investigate the effect of ALD pulse sequence in recipes on conductivities of ALD YSZ.
- Study the effects of grain size, grain boundary and thickness of YSZ electrolytes on oxygen ionic conductivity.

1.3 Outline of Thesis

YSZ thin film electrolytes for SOFCs fabricated by PEALD has been studied. tetrakis(dimethylamido)zirconium(IV) ($Zr(NMe_2)_4$) and (tri-methylcyclopentanol)yttrium ($Y(MeCp)_3$) were selected to be the precursors for zirconium and yttrium, respectively.

Chapter 2 is a literature review on fundamentals of SOFC and ALD, mainly focused on the oxygen ionic conduction mechanism of the electrolyte material YSZ and factors that affect its conductivity.

Chapter 3 outlines the experimental procedure, including sample preparation, the ALD system, and the characterization techniques.

Chapter 4 describes the ALD parameter recipe development of yttrium oxide using precursor $Y(MeCp)_3$ in the low vapor pressure condition. A model has been presented to study the effect of precursor ampoule temperature on ALD reactions.

Chapter 5 investigates the ionic conductivity of PEALD YSZ thin films and the effects of film thickness and microstructures on ionic conductivities.

Chapter 6 discusses the property variations of YSZ thin films fabricated by ALD recipes with different pulsing sequence.

Chapter 7 summarizes the overall conclusions obtained from this work.

Chapter 8 introduces possible future research directions.

1.4 References

[1] Stambouli, A. B., & Traversa, E. (2002). Solid oxide fuel cells (SOFCs): a review of an environmentally clean and efficient source of energy. Renewable and sustainable energy reviews, 6(5), 433-455.

[2] Steele, B. C., & Heinzel, A. (2001). Materials for fuel-cell technologies. Nature, 414(6861), 345-352.

[3] Foroughi-Abari, A., & Cadien, K. (2012). Atomic layer deposition for nanotechnology. In Nanofabrication (pp. 143-161). Springer Vienna.

[4] Putkonen, M., Sajavaara, T., Niinistö, J., Johansson, L. S., & Niinistö, L. (2002). Deposition of yttria-stabilized zirconia thin films by atomic layer

epitaxy from β-diketonate and organometallic precursors. Journal of Materials Chemistry, 12(3), 442-448.

[5] Bernay, C., Ringuedé, A., Colomban, P., Lincot, D., & Cassir, M. (2003). Yttria-doped zirconia thin films deposited by atomic layer deposition ALD: a structural, morphological and electrical characterisation. Journal of Physics and Chemistry of Solids, 64(9), 1761-1770.

[6] Sik Son, K., Bae, K., Woo Kim, J., Suk Ha, J., & Hyung Shim, J. (2013). Ion conduction in nanoscale yttria-stabilized zirconia fabricated by atomic layer deposition with various doping rates. Journal of Vacuum Science & Technology A: Vacuum, Surfaces, and Films, 31(1), 01A107.

Chapter 2

Literature Review

2.1 Electrolytes of SOFCs

A SOFC consists of two electrodes sandwiched around a hard ceramic electrolyte [1]. For oxygen ionic conduction SOFCs shown in Figure 2.1, hydrogen gas and oxygen gas are supplied on the anode and cathode side, respectively. Oxygen ions are produced on the cathode side from the reaction between oxygen molecules and electrons. The electrolyte layer functions as the transport passage for oxygen ions. When oxygen ions arrive at the anode side, hydrogen molecules react with oxygen ions, producing water and electrons. Electric power is generated when electrons travel through the circuit.

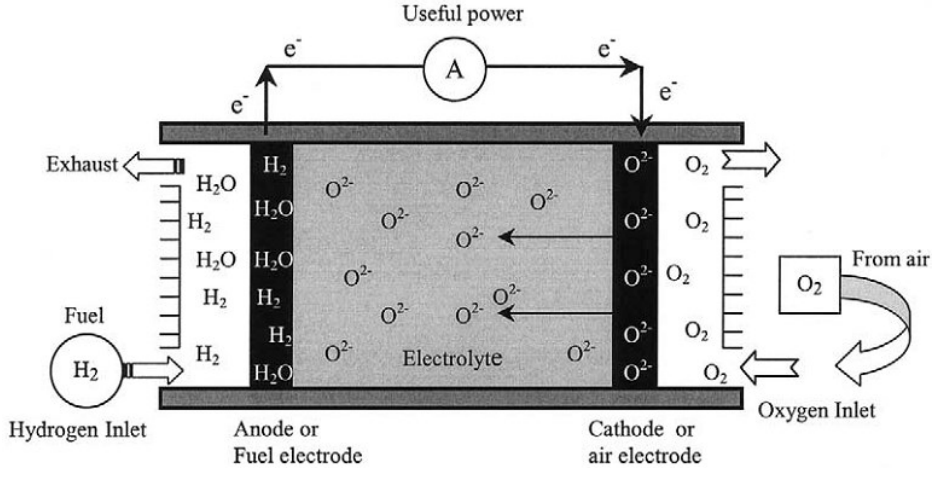

Figure 2.1 Schematics of oxygen ionic conduction SOFCs [1].

The cell open circuit voltage (OCV, E_o) is the electromotive force of an SOFC, and it can be calculated from the free energy change ΔG of the electrochemical reaction or from the partial pressure of the oxygen at the cathode $P_o(c)$ and at the anode $P_o(a)$ [2]:

$$E_o = -\Delta G / nF = (RT / nF) \ln P_o(c) / P_o(a) \quad (2.1)$$

where R is the gas constant, T is the absolute temperature, F is the Faraday constant, and n is the electron equivalent of oxygen (n=4). At 1000°C the OCV is approximately 1V when using pure hydrogen fuel and air. However, when operating SOFCs, the measured voltage is always lower than the theoretically calculated OCV because of the following four types of irreversibility [3].

1. **Activation losses.** The reactions taking place on the electrode surfaces are slow. As a result, a proportion of the OCV is lost to drive the chemical reaction that transfers electrons between the cathode and the anode. The activation losses could be reduced by raising the cell temperature, using more effective catalysts, and increasing electrode roughness and reactant concentrations.
2. **Fuel crossover and internal currents losses.** If the fuel or electrons pass through the electrolyte, fuel crossover and internal currents irreversibility happens. Therefore, a high gas-tightness of the electrolyte is necessary to decrease this irreversibility.

3. **Ohmic losses**. The ohmic resistance of the electronic and ionic transport path is the cause of ohmic losses. For electronic ohmic losses, using electrodes with the highest possible electronic conductivity materials is a solution. For ionic ohmic losses, reducing the electrolytes thickness or choosing materials with high conductivity can improve it.
4. **Mass transport or concentration losses.** When there is a change of reactant concentration at the surface of electrodes, this type of irreversibility occurs. From equation (2.1) we can see that a change in reactant concentration leads to a variation of partial pressure, leading to a lower voltage.

Electrolytes are the critical components of SOFCs, determining the operating temperatures [1]. From the irreversibility section mentioned above, it can be seen that electrolytes play an important role in reducing the fuel crossover and the internal currents and ohmic losses. Correspondingly, an ideal oxygen ionic electrolyte has the following properties [1,3]:

1. High oxygen ionic conductivity
2. Low or no electronic conductivity
3. Good thermal and chemical stability
4. Low thickness to reduce ohmic losses
5. Completely dense to maximize conductivity and minimize reactants cross-over

Goodenough [4] has provided a comprehensive review of oxide ion electrolytes, the materials used and the conduction mechanisms. There are two main types of electrolytes, fluorites and perovskites. In this thesis, only YSZ, one of the most popular fluorite-structured electrolyte materials, is investigated.

2.2 Yttria-stabilized Zirconia (YSZ)

YSZ is ideal to be electrolyte material due to its purely oxygen ionic conduction (with no electronic conduction) [1]. In pure zirconium oxide, oxygen vacancies exist as intrinsic defects, which provide oxygen ions paths to transport. However, the amount of intrinsic oxygen vacancies is very limited, and that is why yttrium oxide is introduced into zirconium oxide, forming YSZ. The mechanism [3] of oxygen ionic conduction in YSZ is shown in Figure 2.2(a). When Zr^{4+} ions are substituted with Y^{3+} ions, extrinsic oxygen vacancies are generated in the fluorite crystal structure acting as the conduction passage for oxygen ions.

According to the phase diagram [5] Figure 2.2(b), 8YSZ is the zirconia with the minimum yttrium oxide concentration to be fully stabilized, showing the highest ionic conductivity.

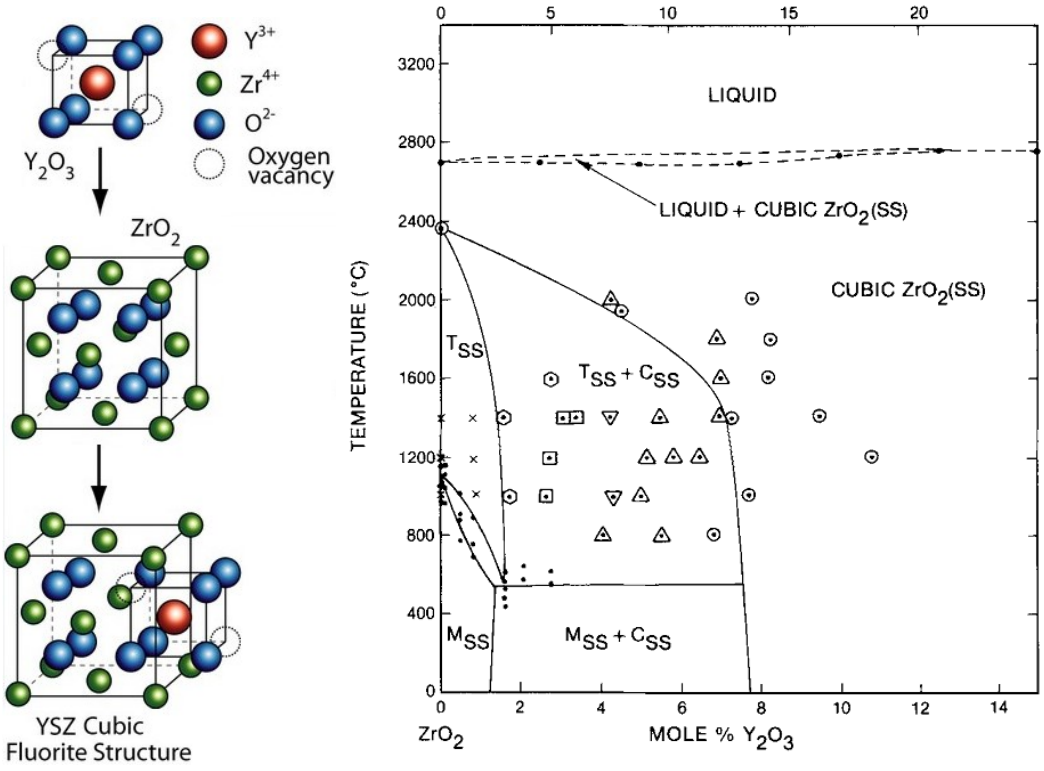

(a)YSZ structure [5] (b) Phase diagram of the System ZrO_2-Y_2O_3 [6]

Figure 2.2 Oxygen ionic conduction mechanism of YSZ.

Peters [7] developed the explanation why 8YSZ exhibits the highest oxygen ionic conductivity. When the concentration of Y_2O_3 is lower than 8 mol%, more oxygen vacancies are created with increasing the concentration of Y_2O_3, which is also the conduction mechanism of YSZ. When increasing the Y_2O_3 concentration above 8 mol%, the strong Coulombic interactions among oxygen vacancies act as a barrier for oxygen ionic conduction, leading to a lower conductivity.

2.3 Intermediate Temperature SOFCs

As we mentioned in section 2.1, raising the SOFC cell operating temperature can reduce the activation losses and increase reaction rates. However, high temperature is also a challenge for the construction, durability, cost, and lifetime of SOFCs [1,3]. Decreasing the operating temperature of SOFCs to intermediate temperature (IT-SOFCs) range from 500°C to 750°C [8] or even lower has attracted much attention in both academia and industry.

Since the oxygen ionic conductance of electrolytes decreases when the operating temperature goes down, the main focus of IT-SOFCs is to improve the electrolyte conductance. There are two main ways to achieve this [9]. The first way is to reduce the thickness of electrolyte, shortening the distance that ions need to travel. The second one is to improve the ionic conductivity of the electrolyte.

2.4 Atomic Layer Deposition (ALD)

To fulfill the requirements in IT-SOFC operating temperature range, a fabrication technique, with the capacity to produce hermetic thin film electrolytes with no pin-holes, is required. Mingde [10] and Beckel [11] published very comprehensive studies of the available electrolyte fabrication methods, including

tape casting, slurry coating, CVD, sol-gel, sputtering, plasma spraying, and ALD. More detailed information can be found in the references [10, 11].

ALD is a thin film deposition technique that has attracted much attention in both industry and academia [12]. Compared with other techniques, the major advantage of ALD is conformal and pin-hole free thin film production due to its self-saturation reaction, which perfectly matches the requirements of electrolytes in SOFCs. A schematic diagram [13] of the ALD process is shown in Figure 2.3. A pulse of precursor A is introduced into the reaction chamber, during which the precursor A molecules are first physi-sorbed and then chemi-sorbed on the substrate. An inert gas purge follows to eliminate the precursor A residues. Precursor B molecules are then pulsed into the reaction chamber and react with precursor A molecules on the substrate surface. Another inert gas purge is used to remove byproducts and precursor residues. After the ALD cycle, a single layer of the needed material is obtained. The thickness of materials can be controlled by repeating the ALD cycles as long as desired.

In ALD research, a recipe parameter optimization is done to make sure the reaction occurs as we expected. The key parameters include the deposition temperature, precursor A pulse time, precursor A purge time, precursor B pulse time, and precursor B purge time.

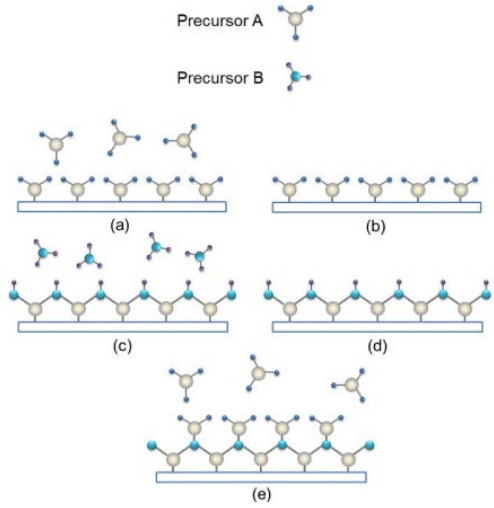

Figure 2.3. The schematic of ALD [13]: (a) precursor A is introduced into the reaction chamber; (b) unabsorbed precursor A is purged; (c) precursor B is introduced and react with precursor A only on the substrate surface; (d) excess precursor B and by-products are purged; (e) next cycle begins by introducing precursor A.

Choosing a suitable deposition temperature range plays a very important role in ALD growth saturation. The purpose of optimizing substrate temperature is to identify the "ALD window". When the ALD window is obtained, further optimization can be done within the ALD window. If the reaction happens outside the ALD window, incomplete reaction, condensation, incomplete reaction, desorption, or thermal decomposition will occur, as shown in Figure 2.4 [14].

The incomplete reaction happens when the substrate temperature is too low and the thermal energy is not high enough to overcome the activation barrier for the surface reaction. As a result, a portion of precursor molecules fail to react with the substrate, leading to a low growth per cycle (GPC).

The condensation appears when the precursor molecules condense on the substrate at low temperature. The achieved high GPC consists of the growth from ALD reaction and condensed precursor molecules.

The decomposition takes place in the case that the thermal energy is high enough to break the bonds within the precursor molecules. Consequently, the reaction becomes not self-saturated with a high GPC.

The precursor molecules would desorb at high substrate temperature if they are only physical adsorbed on the substrate. In this case, a fraction of precursor molecules leave the substrate before any chemical reaction happens, and a low GPC is obtained.

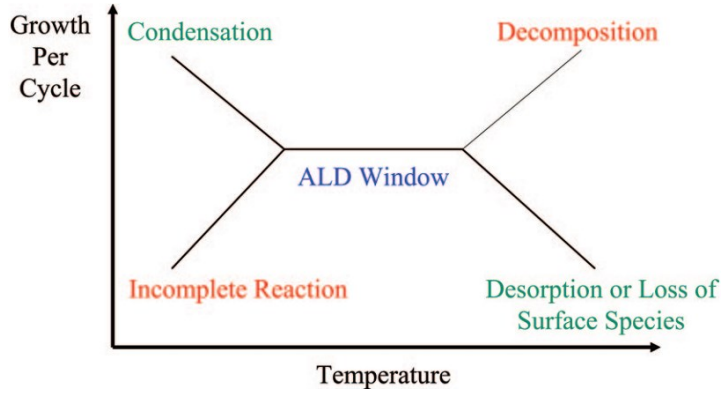

Figure 2.4. Schematic of possible behavior in different deposition temperature ranges [14].

Long enough pulse time and purge time are desired to complete the self-saturated ALD reaction. The pulse time ensures full precursor coverage of substrate surface, and the purge time is responsible for removing all the extra

precursors and by-products from the reaction chamber. However, too long pulses result in precursor and inert gases waste.

2.5 Factors that affect ionic conductivity of YSZ

There are many factors that influence the properties of fabricated YSZ. In this section, the effects of yttrium oxide concentration in YSZ, grain size, the thickness of YSZ thin films, and the crystalline defects in YSZ microstructures are discussed. According to the schematic of four components of materials science and engineering [15] (Figure 2.5), by using different ALD processing parameters, some specific structures of YSZ can be obtained, resulting in a high ionic conductivity property, and ultimately leading to a better SOFC performance.

Figure 2.5. Four components of materials science and engineering [15].

2.5.1 Effect of yttrium oxide concentration

For conventionally fabricated bulk YSZ at operating temperatures around 1200°C, it has been widely accepted that the 8YSZ exhibits the highest ionic conductivity. In Section 2.2, the mechanism of 8YSZ having the highest ionic conductivity has been presented.

However, the phase diagram is possibly different for nanometer scale YSZ thin film electrolytes, which is desired for ITSOFC in order to achieve the high conductance. Yashima [16] proposed that the phase diagram (Ruh [6]) omitted meta-stable phases in ZrO_2-Y_2O_3 system, which are more likely to be presented at lower temperature levels. Son [17] claimed that 10YSZ is the optimum yttrium oxide doping ratio when ALD is utilized as the fabrication technique. According to his research, the inhomogeneous doping in the vertical direction of ALD fabricated YSZ thin films is the cause of this shift in optimum yttrium oxide concentration in YSZ. Ramamoorthy [18] found that 3YSZ gave the highest ionic conductivity for nanocrystalline YSZ, in contrast to 8YSZ for coarser-grained YSZ. They also showed that the grain boundary effect is dominant when YSZ is nanocrystallized, resulting in the lowest overall activation energy of 3YSZ even though it had the tetragonal rather than cubic crystal structure. Fabbri [19] further showed that the space charge region has a greater effect on lightly doped YSZ than that in highly doped YSZ leading to the highest ionic conductivity in 3YSZ.

2.5.2 Effect of thickness

Thickness affects the conductance of YSZ thin films according to Ohm's law. Conductance, G, is determined by ion conductivity, σ, surface area, A, and thickness, L.

$$G = \sigma \frac{A}{L} \tag{2.2}$$

Reducing the thickness of YSZ leads to a higher conductance. However, the effect of thickness on the conductivity has not been thoroughly investigated. Gilardi [18] studied the effect of thickness from 70 nm to 300 nm on ionic conductivity. They found that the sample with thickness of 70 nm shows the highest conductivity at 500ºC. Other research by Kosacki [19] found that ionic conductivity is independent of thickness when thickness is high, and when thickness gets less than 60 nm, an exceptionally high ionic conductivity was found. Kosacki attributes the improvement to the contribution from interface conductivity. The total conductivity was expressed by a rule of mixtures model as shown in equation (2.3) [19].

$$\sigma^n = \sigma_s^n f_s + \sigma_b^n (1 - f_s) \tag{2.3}$$

where σ_s is the interface or grain boundary conductivity, f_s is the volume fraction occupied by the interfacial conduction path (interface thickness divided by total thickness), σ_b is the lattice or grain conductivity, and n is a parameter that depends on the morphology, roughness, strain, and the setup, in the range from -1 to 1. However, Karthikeyan [20] fabricated 17 nm thin YSZ films and found no significant improvement of ionic conductivity. On the contrary, Huang [21] investigated the effect of thickness of conductivity at 550°C, 600°C, and 650°C and found remarkable increasing in conductivity with thickness less than

17 nm. The effect of thickness on ionic conductivity is still controversial, and therefore needs further investigation.

2.5.3 Effect of grain size

Grain boundaries in YSZ are usually treated as blocking layers for oxygen ionic conduction with high activation energies due to the defect segregation in grain boundaries [7]. However, when the thickness scales down to the nanometer scale, the effect of grain boundaries is not decided in the literature.

Kosacki [21] observed an increase in ionic conductivity when grain size reduces to 20 nm. This was attributed to size-dependent grain boundary segregation. When the grain size reduces to 20 nm, oxygen ions are easier to diffuse through the grain boundary areas. Similar results were observed by some other researchers [19, 22-24]. Aoki [25] concluded that the change of grain boundaries from blocking layers to enhancing is due to the dilution of ionic blocking impurities resulting from the reduced grain size.

However, De Souza [26] found grain boundaries hinder oxygen ions transport even when grain size is reduced to the nanometer scale. Kim [27] demonstrated that oxygen vacancies are immobile in grain boundaries, and that the immobility increases with decreasing the grain size. Several researchers [28-31] have concluded that grain boundaries are blocking oxygen ions transport due to impurities, even in the nanometer scale grain size.

Peters [32] made a summary of the grain size effects on oxygen ionic conductivity. There are two effects, trivial size effect and true size effect, as shown in the schematic Figure 2.6.

The trivial size effect is the effect of higher density of grain boundaries resulting from smaller grain size in the materials, which leads to a higher proportion of grain boundary conduction in total oxygen ion transport. If the conductivity of grain boundaries can be improved significantly, the trivial size effect will lead to a high conductivity for nano-crystalline YSZ.

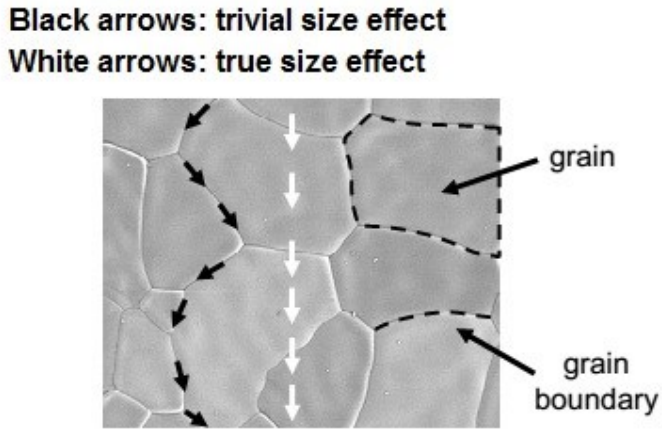

Figure 2.6. Schematic of the two effects of reducing grain size on oxygen ionic conduction [31].

The true size effect involves intrinsic modification of the local physical properties in the vicinity of the grain boundaries. In this model a grain boundary consists of a grain boundary core and two space charge layers (SCLs). It can be

seen from Figure 2.7 that when the core is depleted with positively charged oxygen vacancies, the concentration of oxygen vacancies in SCLs will increase. In the cases that the SCLs thickness is comparable to the grain size of nano-crystalline YSZ, the oxygen vacancies concentration within grains would increase significantly, leading to a higher conductivity.

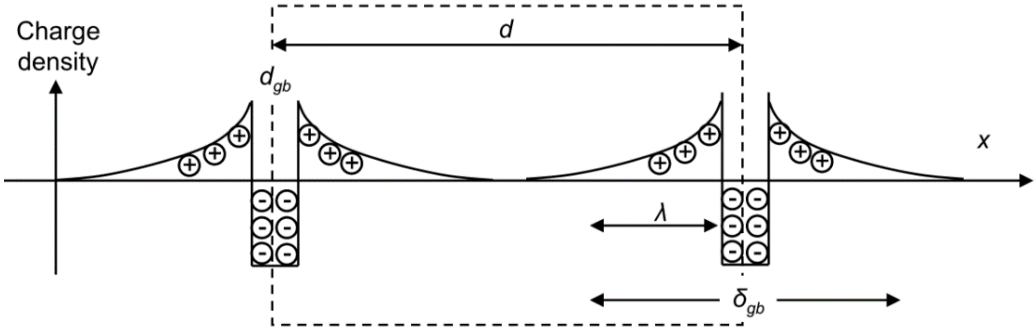

Figure 2.7. True size effect when grain boundary cores are depleted with positively charged oxygen vacancies [31].

2.6 References

[1] Stambouli, A. B., & Traversa, E. (2002). Solid oxide fuel cells (SOFCs): a review of an environmentally clean and efficient source of energy. Renewable and sustainable energy reviews, 6(5), 433-455.

[2] Yamamoto, O. (2000). Solid oxide fuel cells: fundamental aspects and prospects. Electrochimica Acta, 45(15), 2423-2435.

[3] Larminie, J., Dicks, A., & McDonald, M. S. (2003). Fuel cell systems explained (Vol. 2). Chichester, UK: J. Wiley.

[4] Goodenough, J. B. (2003). Oxide-ion electrolytes. Annual review of materials research, 33(1), 91-128.

[5] https://en.wikipedia.org/wiki/Yttria-stabilized_zirconia

[6] RUH, R., Mazdiyasni, K. S., Valentine, P. G., & Bielstein, H. O. (1984). Phase Relations in the System ZrO2 ‐ Y2O3 at Low Y2O3 Contents. Journal of the American Ceramic Society, 67(9).

[7] Peters, C. (2009). Grain-size effects in nanoscaled electrolyte and cathode thin films for solid oxide fuel cells (SOFC) (Vol. 15). KIT Scientific Publishing.

[8] Brett, D. J., Atkinson, A., Brandon, N. P., & Skinner, S. J. (2008). Intermediate temperature solid oxide fuel cells. Chemical Society Reviews, 37(8), 1568-1578.

[9] Wu, F., Wu, J. N., Banerjee, S., Blank, O., & Banerjee, P. (2013). Frontiers in applied atomic layer deposition (ALD) research. In Materials Science Forum (Vol. 736, pp. 147-182). Trans Tech Publications.

[10] Liang, M., Yu, B., Wen, M., Chen, J., Xu, J., & Zhai, Y. (2008). The Fabrication Technique of YSZ Electrolyte Film. Progress in Chemistry, 20(7/8).

[11] Beckel, D., Bieberle-Hütter, A., Harvey, A., Infortuna, A., Muecke, U. P., Prestat, M., ... & Gauckler, L. J. (2007). Thin films for micro solid oxide fuel cells. Journal of Power Sources, 173(1), 325-345.

[12] Muneshwar, T., & Cadien, K. (2015). Influence of atomic layer deposition valve temperature on ZrN plasma enhanced atomic layer deposition growth. Journal of Vacuum Science & Technology A: Vacuum, Surfaces, and Films, 33(6), 060603.

[13] Foroughi-Abari, A., & Cadien, K. (2012). Atomic layer deposition for nanotechnology. In Nanofabrication (pp. 143-161). Springer Vienna.

[14] George, S. M. (2009). Atomic layer deposition: an overview. Chemical reviews, 110(1), 111-131.

[15] Callister, William D., (2009). Materials Science and Engineering: An Introduction, 8th Edition. Wiley.

[16] Yashima, M., Kakihana, M., & Yoshimura, M. (1996). Metastable-stable phase diagrams in the zirconia-containing systems utilized in solid-oxide fuel cell application. Solid State Ionics, 86, 1131-1149.

[17] Sik Son, K., Bae, K., Woo Kim, J., Suk Ha, J., & Hyung Shim, J. (2013). Ion conduction in nanoscale yttria-stabilized zirconia fabricated by atomic layer deposition with various doping rates. Journal of Vacuum Science & Technology A: Vacuum, Surfaces, and Films, 31(1), 01A107.

[18] Gilardi, E. (2016). Interface effects in Y2Zr2O7 thin films.

[19] Kosacki, I., Rouleau, C. M., Becher, P. F., Bentley, J., & Lowndes, D. H. (2005). Nanoscale effects on the ionic conductivity in highly textured YSZ thin films. Solid State Ionics, 176(13), 1319-1326.

[20] Karthikeyan, A., Chang, C. L., & Ramanathan, S. (2006). High temperature conductivity studies on nanoscale yttria-doped zirconia thin films and size effects. Applied physics letters, 89(18), 183116.

[21] Kosacki, I., Suzuki, T., Petrovsky, V., & Anderson, H. U. (2000). Electrical conductivity of nanocrystalline ceria and zirconia thin films. Solid State Ionics, 136, 1225-1233.

[22] Cheikh, A., Madani, A., Touati, A., Boussetta, H., & Monty, C. (2001). Ionic conductivity of zirconia based ceramics from single crystals to nanostructured polycrystals. Journal of the European Ceramic Society, 21(10), 1837-1841.

[23] Brossmann, U., Knoner, G., Schaefer, H. E., & Wurschum, R. (2004). Oxygen diffusion in nanocrystalline ZrO 2. Reviews on Advanced Materials Science, 6(1), 7-11.

[24] Knöner, G., Reimann, K., Röwer, R., Södervall, U., & Schaefer, H. E. (2003). Enhanced oxygen diffusivity in interfaces of nanocrystalline ZrO2· Y2O3. Proceedings of the National Academy of Sciences, 100(7), 3870-3873.

[25] Aoki, M., Chiang, Y. M., Kosacki, I., Lee, L., Tuller, H., & Liu, Y. (1996). Solute Segregation and Grain ‐ Boundary Impedance in High ‐ Purity

Stabilized Zirconia. Journal of the American ceramic society, 79(5), 1169-1180.

[26] De Souza, R. A., Pietrowski, M. J., Anselmi-Tamburini, U., Kim, S., Munir, Z. A., & Martin, M. (2008). Oxygen diffusion in nanocrystalline yttria-stabilized zirconia: the effect of grain boundaries. Physical Chemistry Chemical Physics, 10(15), 2067-2072.

[27] Kim, S., Jain, P., Avila-Paredes, H. J., Thron, A., van Benthem, K., & Sen, S. (2010). Strong immobilization of charge carriers near the surface of a solid oxide electrolyte. Journal of Materials Chemistry, 20(19), 3855-3858.

[28] Tuller, H. L. (2000). Ionic conduction in nanocrystalline materials. Solid State Ionics, 131(1), 143-157.

[29] Boulc'h, F., Djurado, E., & Dessemond, L. (2004). Dopant segregation and space charge effect in nanostructured tetragonal zirconia. Journal of The Electrochemical Society, 151(8), A1210-A1215.

[30] Guo, X., & Maier, J. (2001). Grain boundary blocking effect in zirconia: a Schottky barrier analysis. Journal of the Electrochemical Society, 148(3), E121-E126.

[31] Chen, X. J., Khor, K. A., Chan, S. H., & Yu, L. G. (2002). Influence of microstructure on the ionic conductivity of yttria-stabilized zirconia electrolyte. Materials Science and Engineering: A, 335(1), 246-252.

[32] Peters, C. (2009). Grain-size effects in nanoscaled electrolyte and cathode thin films for solid oxide fuel cells (SOFC) (Vol. 15). KIT Scientific Publishing.

Chapter 3

Experimental Procedure and Characterization Techniques

3.1 Introduction

This chapter describes experimental procedures and characterization methods. The features of the ALD 150-LX system are discussed, and then followed by sample preparation, including substrate preparation and pre-deposition treatment. The characterization techniques utilized for ALD thin films are discussed in the later part.

3.2 ALD 150-LX system

All ALD depositions were performed in a commercial ALD system, ALD-150LX (Kurt J. Lesker Inc.), schematically shown in Figure 3.1. It can accommodate four different precursors using thermal ALD or PEALD. Inert gas (Ar when there is a deposition and N_2 when there are no depositions) is continuously flowing through the reactor gas line and chamber to prevent condensation of precursors or byproducts on the reactor walls. Considering the trade-off [1] between gas interdiffusion and entrainment, the pressure in the

chamber was kept at 1 torr during the deposition. All the gas flows were controlled by electronic mass flow controllers (MKS Instruments). A remote inductively coupled plasma (ICP) source was utilized in the system as shown in Figure 3.1. The maximum power of the plasma was 600W with a ramping rate of 6000W/s.

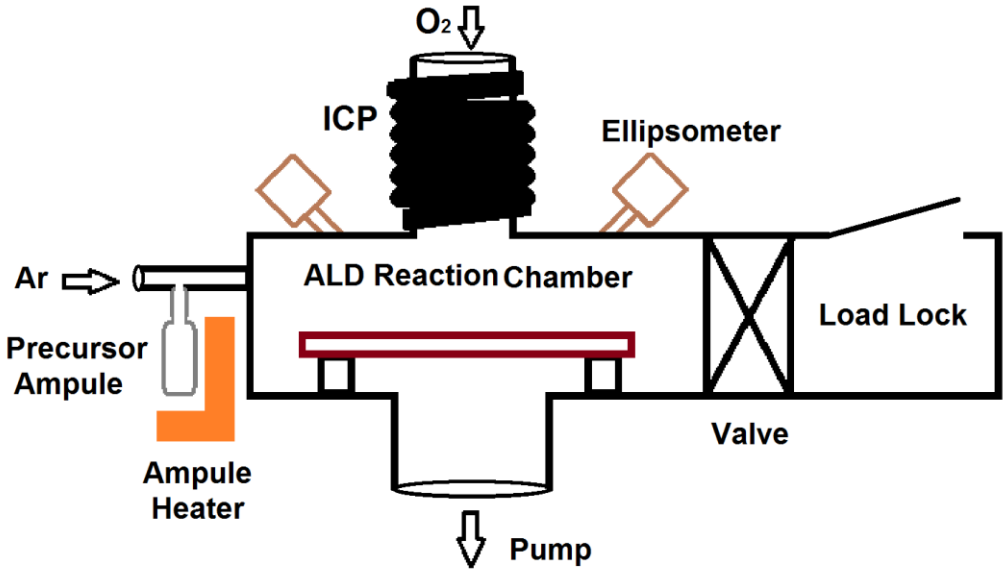

Figure 3.1 Schematic of ALD-150LX (Kurt J. Lesker Inc.).

Precursor materials used for zirconium oxide and yttrium oxide were $Zr(NMe_2)_4$ and $Y(MeCp)_3$ (from Strem Chemicals Inc..), respectively. They were kept in stainless steel ampoules at 110°C and 75°C, to provide high enough vapor pressures for ALD reactions. In order to avoid condensation of precursor materials, the ALD valves and the gas lines were heated as well, as shown in Table 3.1.

Table 3.1 Temperature set-points for precursors

Precursor	$T_{ampoule}$ (°C)	T_{valve} (°C)	T_{line} (°C)
$Zr(NMe_2)_4$	75	95	110
$Y(MeCp)_3$	110	120	130

3.3 Sample Preparation

Lightly doped p-type Si(100) wafers were used as substrate. They were diced into 15mm×20mm pieces using a dicing saw (Disco DAD 321). The substrates were cleaned using piranha solution (a mixture of H_2SO_4 and H_2O_2 with the volume ratio of 3:1) for 15 minutes to eliminate any organic contaminations. After cleaning, substrates were stored in sealed containers prior to deposition.

When substrates were transferred into the process chamber, they were exposed to oxygen plasma before the deposition in order to enable desorption of surface contaminations and condition the substrate surface for PEALD process.

3.4 Characterization methods

Various techniques were used to characterize the ALD growth and material properties of PEALD Y_2O_3 and YSZ thin films. In-situ spectroscopic

ellipsometery was performed to optimize the recipe of PEALD parameters by identifying thickness under different conditions as shown in Figure 3.1. Four-point electrical tests were conducted to measure the oxygen ionic conductivity of PEALD YSZ thin films. Concentrations of yttrium oxide and impurity levels in PEALD YSZ thin films were studied using x-ray photoelectron spectroscopy (XPS). The crystal structure of the ALD films was investigated using x-ray diffraction (XRD). Atomic force microscopy (AFM) was utilized to measure roughness and grain size of PEALD YSZ thin films.

3.4.1 In-situ Spectroscopic Ellipsometery (i-SE)

Spectroscopic ellipsometry (SE) is an optical measurement technique that allows determination of thickness and optical properties of thin films by characterizing light reflection (or transmission) from the sample [2]. SE measures two parameters, amplitude ratio ψ and phase difference Δ between p-polarized (parallel to the incident plane) and s-polarized (perpendicular to the incident plane) reflected lights.

$$\rho = \frac{r_p}{r_s} = tan\psi \cdot e^{i\Delta} \tag{3.1}$$

r_p and r_s are the complex amplitude reflection coefficients of reflected lights p-component and s-component [2]. The measured amplitude ratio ψ and phase difference Δ were utilized to fit the thickness and optical parameters in an optical

model iteratively. By lowing the mean square error (MSE) and keeping the fit parameters physically reasonable, the thickness and optical properties can be obtained. Thus, SE is a very powerful tool for in-situ characterization.

In this thesis, a research SE tool J.A.Woollam M-2000DI was used to in-situ characterize ALD films during growth. The incident angle was fixed at 70°, and the photon energy range was from 0.735eV to 6.464eV. The location of this SE tool in the ALD system is shown in Figure 3.1. An physical model built specifically for the present study is shown in Figure 3.2. There are three layers in this model, and they are the silicon wafer substrate, native oxide of silicon and the ALD grown layers (yttrium oxide, zirconium oxide, or YSZ). A Cauchy model was used to parametrize the dielectric function of the ALD layers. The upper limit of the photon energy was set to be 4.5 eV since the band gaps of yttrium oxide and zirconium oxide are about 5.5 eV [3] and from 5eV to 7 eV [4], respectively. The acquired ellipsometric data was analyzed using CompleteEASE software (version 4.48) from J. A. Woollam with built-in models for dielectric function and a dielectric constant library for standard materials. During the ALD process, the sample thickness was fit every five cycles. In almost all cases, the initial growth ALD thickness versus number of cycles curve is not linear. In the beginning of the ALD, it is heterodeposition stage in which the material is deposited on the substrate; while after the first stage the material is grown on itself, which is called homodeposition stage. The GPC difference between

heterodeposition and homodeposition leads to the substrate-enhanced or the substrate-inhibited growth pattern, as shown in Figure 3.3. The linear fits to obtain growth GPC were conducted in the straight region of thickness versus the number of cycles curve in the homodeposition stage.

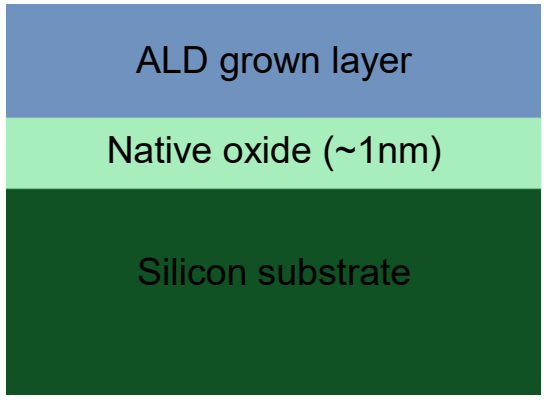

Figure 3.2. Multi-layered model for i-SE characterization.

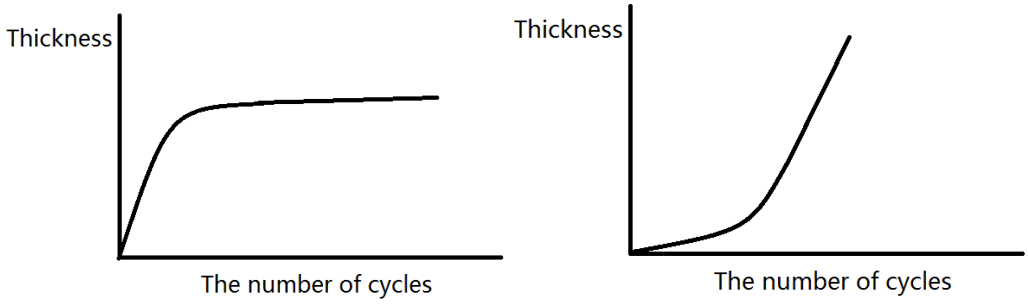

(a) Substrate-enhanced growth (b) Substrate-inhibited growth

Figure 3.3. Schematics of substrate-enhanced and substrate-inhibited ALD growth patterns.

3.4.2 Four-Point Ionic Conductivity Test

Four-point conductivity measurements are commonly used to measure the electrical properties of solids and thin films in material science and semiconductor industries due to easy sample preparation and high accuracy. A schematic of test setup is shown in Figure 3.4. Four Ag wires were attached to the sample with Ag paste. A Keithley model 2400 series sourcemeter was used to provide a constant current for the measurement. The distances of 1&2, 2&3, 3&4 were kept the same. At the test temperatures, when applying a constant current, I, through the outer contacts 1 and 4, a voltage drop, ΔU, across the inner contacts 2 and 3, was recorded. Then the conductivity of the tested sample can be calculated by equation 3.2.

$$\sigma = \left(\frac{ln2}{\pi d}\right)\frac{I}{U_{23}} \tag{3.2}$$

where σ is the conductivity, d is the thickness of samples, U_{23} is the measured voltage difference between inner contacts 2 and 3.

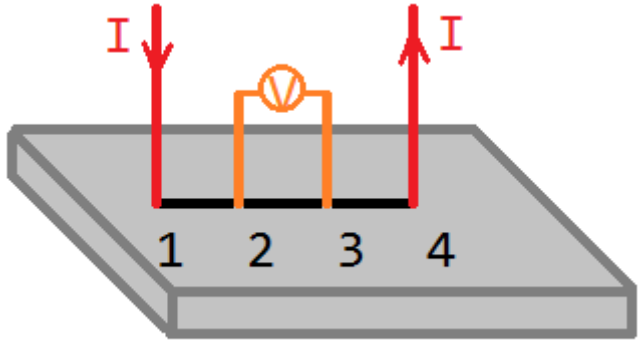

Figure 3.4. The schematic of four-point ionic conductivity test.

The activation energy of ionic conduction can be indirectly obtained from conductivity results [5] as follows. The conductivity σ is determined from the majority carrier concentration n, the carrier's charge q, and the mobility of carrier μ.

$$\sigma = nq\mu \tag{3.3}$$

The mobility is a function of the carrier charge q, temperature T, and diffusivity D.

$$\mu = \frac{qD}{RT} \tag{3.4}$$

where R is the gas constant. We also know that the dependence of diffusivity on absolute temperature T follows the Nernst equation, which is

$$D = D_0 \exp(-\frac{Q_d}{RT}) \tag{3.5}$$

where D_0 is an approximately temperature-independent pre-exponential, and Q_d is the activation energy for diffusion. Combining equation (3.3) (3.4), and (3.5), we can have

$$\sigma = \frac{nq^2}{RT} D_0 exp(-\frac{Q_d}{RT}) \tag{3.6}$$

Taking logarithms to the base 10 of equation (3.6) yields

$$\log(\sigma T) = \log\left(\frac{nq^2 D_0}{R}\right) - \frac{Q_d}{2.3R}(\frac{1}{T}) \tag{3.7}$$

Because n, q, D_0, R, and Q_d are all constants, the activation energy Q_d can be obtained by plotting logarithmic σT versus (1/T).

3.4.3 X-Ray Diffraction (XRD)

X-Ray Diffraction (XRD) is a method to investigate the crystal structure of materials using Bragg's law [6]:

$$2dSin\theta = n\lambda \tag{3.8}$$

where d is the interspacing between atomic planes, θ is the incident angle, λ is the wavelength of the beam.

A Rigaku Ultima IV XRD system for the studies using 0.15418 nm Cu-Kα radiation (40 kV, 44mA). A thin film attachment was utilized to study the crystallinity of the thin ALD samples. During operation, the scan speed was set to 2 degrees per minute with a sampling width of 0.05 degree. The glancing angle, omega, was set 0.5 to ignore the peaks from silicon substrates, and the scan range was from 10 degrees to 80 degrees.

3.4.4 X-Ray Photoelectron Spectroscopy (XPS)

X-Ray photoelectron spectroscopy (XPS) is a commonly used qualitative and quantitative chemical analysis technique for surface characterization. XPS is capable of investigating elemental composition and chemical state of elements [6]. A monochromatic X-ray beam (Al-Kα) was applied to the sample surface. The photons are absorbed by sample surface, and electrons are emitted according to the photoelectric effect [7].

The detector receives the energy of the emitted electrons, and then the data is presented as a graph of intensity (usually expressed as counts or counts per second) versus binding energy of the electron. The detected kinetic energy of the electron is dependent on the photon energy of the X-rays employed and therefore is not an intrinsic property. The binding energy of the electron is a parameter that identifies the electron. The relationship between the kinetic energy, $E_{kinetic}$, and the binding energy, $E_{binding}$, is according to Ernest Rutherford's equation:

$$E_{binding} = E_{photon} - E_{kinetic} - W \tag{3.9}$$

where E_{photon} is the photon energy, and W is the work function of the spectrometer.

Every element has a characteristic set of peaks at specific binding energies from which the qualitative analysis can be accomplished. The peak intensities represent the quantitative information of each element. Also, the chemical state influences the locations of peaks, leading to shifts to higher or lower binding energy levels.

In this thesis, XPS measurements were performed using an Axis Ultra Spectrometer (Kratos Analytical) to study the elemental compositions and chemical bonding of ALD thin films. A monochromatic Al-Kα radiation (hν = 1486.71 eV) was used during the measurements under ultrahigh vacuum condition (5×10^{-10} torr). CasaXPS software was utilized to analyze the XPS data. Calibrations were conducted by using C 1s peak at 284.8eV. For quantification

analysis, Shirley type background was used for both zirconium and yttrium. The relative sensitivity factors for zirconium 3p peak and yttrium 3p peak were 7.78 and 7.19, respectively. The concentration of yttrium oxide can be obtained from yttrium and zirconium atomic percentages. Using the same method, a bulk 8YSZ sample with ~8.7 mol% Y_2O_3 was measured three times as a standard. The standard measurement result was 11.9±0.3 mol%. The quantification analysis results were calibrated according to this standard measurement.

3.4.5 Atomic Force Microscopy (AFM)

In atomic force microscopy (AFM) a micro-fabricated sharp solid force probe is used to scan the surface of samples, measuring the surface height [8]. When the probe is brought into proximity of a sample's surface, a deflection occurs due to forces between the probe tip and the sample. AFM can be operated in three modes: contact mode, tapping mode, and non-contact mode. In this thesis, a Veeco Dimension 3100 AFM tool was used in the tapping mode to characterize the roughness and grain size of YSZ thin films. The grain size was measured by the classical line intersection method with Image J. In this method, five lines were used to intersect with the grain boundaries. Average grain size was calculated by the ratio of line length and the number of grains. The root mean square (RMS) roughness, calculated using the following equation:

$$\mathrm{RMS} = \sqrt{\frac{\sum Z_i^2}{N}} \tag{3.10}$$

where Z_j is the height at point i, N is the total number of points.

3.5 References

[1] George, S. M. (2009). Atomic layer deposition: an overview. Chemical reviews, 110(1), 111-131.

[2] Fujiwara, H. (2007). Spectroscopic ellipsometry: principles and applications. John Wiley & Sons.

[3] Xu, R., Selvaraj, S. K., Azimi, N., & Takoudis, C. G. (2013). Growth Characteristics and Properties of Yttrium Oxide Thin Films by Atomic Layer Deposition from Novel Y (iPrCp) 3 Precursor and O3. ECS Transactions, 50(13), 107-116.

[4] Chang, J. P., Lin, Y. S., & Chu, K. (2001). Rapid thermal chemical vapor deposition of zirconium oxide for metal-oxide-semiconductor field effect transistor application. Journal of Vacuum Science & Technology B: Microelectronics and Nanometer Structures Processing, Measurement, and Phenomena, 19(5), 1782-1787.

[5] Callister, William D., (2009). Materials Science and Engineering: An Introduction, 8th Edition. Wiley.

[6] Sardela, M. (Ed.). (2014). Practical Materials Characterization. Springer.

[7] Watts, J. F., & Wolstenholme, J. (2003). An introduction to surface analysis by XPS and AES. Wiley.

[8] Haugstad, Greg. (2012). Atomic force microscopy: understanding basic modes and advanced applications. John Wiley & Sons.

Chapter 4

Y_2O_3 PEALD in Low Vapor Pressure Condition of Precursor

4.1 Introduction

ALD [1] is a deposition technique that has attracted much attention in both industry and academia due to its ability to produce high uniformity and conformal films. During the ALD process, the reactant gases (which are called precursors) of two sequential reactions are pulsed into the reaction chamber alternately [2]. Each cycle forms one atomic layer on the surface of the substrate, and a given thickness of the film material with high precision is achieved as the cycles are repeated as many times as desired. ALD has been employed to fabricate composite thin films including nanolaminates, alloys, mixed oxides, and doped materials [3]. The properties of these films were optimized by adjusting the number of each component's ALD cycles in the process recipes.

When choosing an ALD precursor, its vapor pressure is one important factor [2]. Generally, high vapor pressure is required in order to provide enough precursor molecules to fully cover the surface of the substrate. However, for low concentration components in composite materials, choosing precursors with low vapor pressure or lowering precursor temperature might introduce benefits of

lower cost and better properties. For example, yttria-stabilized zirconia (YSZ) is a commonly used electrolyte material in solid oxide fuel cells (SOFCs), and the yttrium oxide concentration in YSZ is usually lower than 10 mol%.

For yttrium oxide ALD, $Y(MeCp)_3$ has been widely used as the precursor material as summarized in Table 4.1. Many studies [4-16] have utilized water or ozone as the oxygen source. The GPC range obtained by most researchers [4-7] using continuous flow systems is from 0.7 Å - 1.9 Å/cycle, except for the case of 3.5 Å/cycle obtained by researchers [8-16] who used the "exposure mode" [8], in which all inlets and outlets of the reactor chamber closed for some time to allow sufficient surface reaction. Oxygen plasma was used as the oxygen source by Cho [17-19], with GPCs of 1.2 Å - 1.9 Å. No matter which oxidant was used, the ampoule temperature was set at high levels.

In this chapter, yttrium oxide ALD using $Y(MeCp)_3$ and oxygen plasma was experimentally studied. In the past, process parameters design has been mainly focused on the pulse and purge times of precursors [18-19], while ampoule temperature was ignored. In our investigation, a model is presented to describe the effect of ampoule temperatures on ALD reactions. As a result, the reaction is not self-limiting but provides a way achieve low yttria compositions in YSZ with potential benefits of a reduced cost and enhanced properties.

.

Table 4.1. Summary of yttrium oxide ALD using $Y(MeCp)_3$ in the literature

Oxygen source	$T_{ampoule}$ (°C)	GPCs(Å/cycle)	Reference
Water	190	1.2	4
Water	110	1.2-1.3	5
Ozone	110	1.2	6
Water	110	0.7-1.2	7
Water	190	3.5	8-16
Oxygen plasma	145	1.2-1.9	17-19

4.2 Experimental Parameters

A schematic diagram of the pulsing sequence for an ALD cycles is shown in Figure 4.1. In the first half reaction, $Y(MeCp)_3$ molecules are introduced into the reaction chamber using short pulses (pulse time of the precursor, t_1) when the ampoule valve is pulsed open. After a purge time (t_2), residual $Y(MeCp)_3$ molecules are removed from the reactor. During the second half reaction, oxygen gas is introduced into the reaction chamber, followed by the 600W ICP plasma ignition (pulse time of the oxygen plasma, t_3). Finally, another purge time (t_4) is used to remove the remaining oxygen.

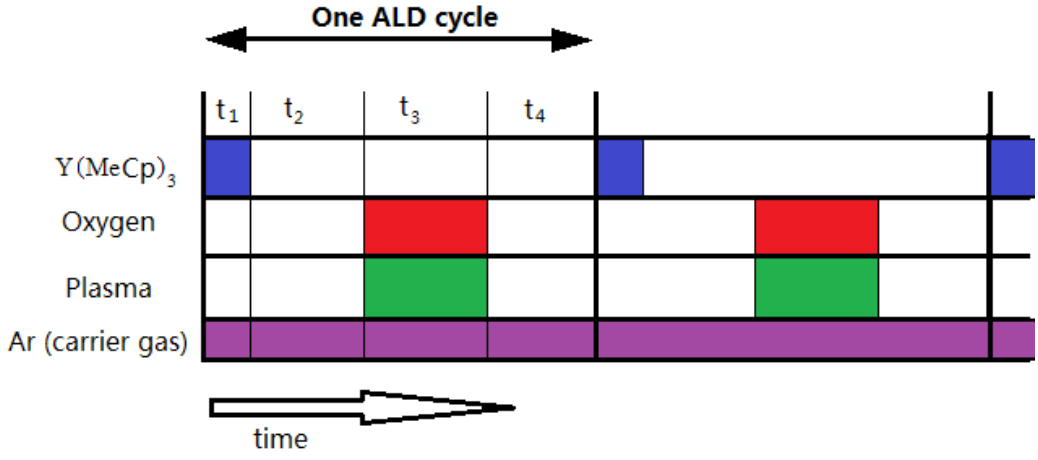

Figure 4.1. The pulsing sequence of ALD cycles.

During ALD, the substrate temperature (T_{sub}) plays an important role in ALD growth since T_{sub} helps to overcome the activation barrier for surface reaction and avoids condensation, incomplete reaction, desorption, or thermal decomposition from occurring [20], as described in section 2.4. In order to optimize an ALD process recipe, as detailed illustrated in earlier work [21], sufficiently long pulses (t_1 and t_3) of $Y(MeCp)_3$ and O_2 plasma are necessary to realize self-limiting surface saturation, so that T_{sub} can be determined. Purge times (t_2 and t_4) after each precursor pulse ensure that by-products and unreacted precursors are completely removed, preventing CVD gas reactions.

After T_{sub} is achieved, minimum pulses and purges (t_1, t_2, t_3, and t_4) are used to reduce material and time consumptions. This process is usually called recipe

optimization. The ALD recipe optimization parameter ranges, used for yttria ALD optimization, are given in Table 4.2.

Table 4.2. Y_2O_3 PEALD recipe optimization, including deposition temperature (T_{sub}), $Y(MeCp)_3$ pulse time (t_1) and the following purge time (t_2), oxygen plasma pulse time (t_3) and the following purge time (t_4)

Optimized parameter	**Range**	**ALD Cycle[a] t_1-t_2-t_3-t_4 (s)**	**T_{sub}[a]**
T_{sub}	50°C - 275°C	10 - 15 - 30 - 10	variable
t_1	1s - 20s	variable - 15 - 30 - 10	T_{sub}*
t_2	5s - 60s	t_1* - variable - 30 - 10	T_{sub}*
t_3	5s - 60s	t_1* - t_2* - variable - 10	T_{sub}*
t_4	5s - 60s	t_1* - t_2* - t_3* - variable	T_{sub}*

[a]The optimized parameter was marked with *

4.3 Results and Discussion

4.3.1 Y_2O_3 growth saturation

The data from the optimization process described in Table 4.2 is shown in Figure 4.2, where substrate temperature, pulse widths and purge times are plotted versus GPC. In Figure 4.2(a) GPC versus substrate temperature (50°C to 275°C) is shown. Below 150°C the GPC declined to ~0.075 Å/cycle, indicating that there

may not enough thermal energy available to drive the surface chemical reactions to completion. Between 150℃ to 225℃, a steady GPC of 0.11 Å/cycle was obtained. Above 225℃, the GPC dropped to lower values due to desorption. The optimized substrate temperature window of 150℃ to 225℃ is consistent with the literature [4, 5]. For the rest of the recipe optimization, the deposition temperature was fixed at 200℃. In Figure 4.2(b), the GPC increased with increasing precursor pulse width, t_1, in the range of 1s to 4s and saturated beyond 4s. Therefore, in the following experiments t_1 was fixed at 4s. During the optimization of oxygen plasma pulse time (t_3), the GPC increased when $0<t_3<10$s, followed by a relatively slow increasing after 10s, as seen in Figure 4.2(d). The initial rapid increase is probably due to the insufficient oxygen plasma dose, and the following slower rise after t_3=10s was attributed to the fact that more $Y(MeCp)_3$ vapor molecules sublimed and were effused out from the ampoule. In the following experiments, oxygen plasma exposure of 30s was used.

In the optimizations of purge time t_2 and t_4, unusual GPC curve patterns were observed. According to the self-limiting nature of ALD, GPC should be high when the purge time is too short due to CVD gas reactions. As the purge time increases, less residual gas is left in the chamber, and GPC would decrease and then saturate. However, in Figure 4.2(c) and (e) GPC did not saturate, but continuously increased with elongated purge times. This suggests that the sublimation of $Y(MeCp)_3$ in the ampoule, during vapor replenishing time

(t_2+t_3+t_4), plays an important role. As t_2+t_3+t_4 gets longer the vapor pressure in ampoule has more time to recover which means that there are more molecules in the precursor pulse, leading to higher GPC. Although 15s for t_2 and 10s for t_4 are long enough to remove the residual $Y(MeCp)_3$ and oxygen plasma respectively, t_2=30s and t_4=20s are used for following experiments.

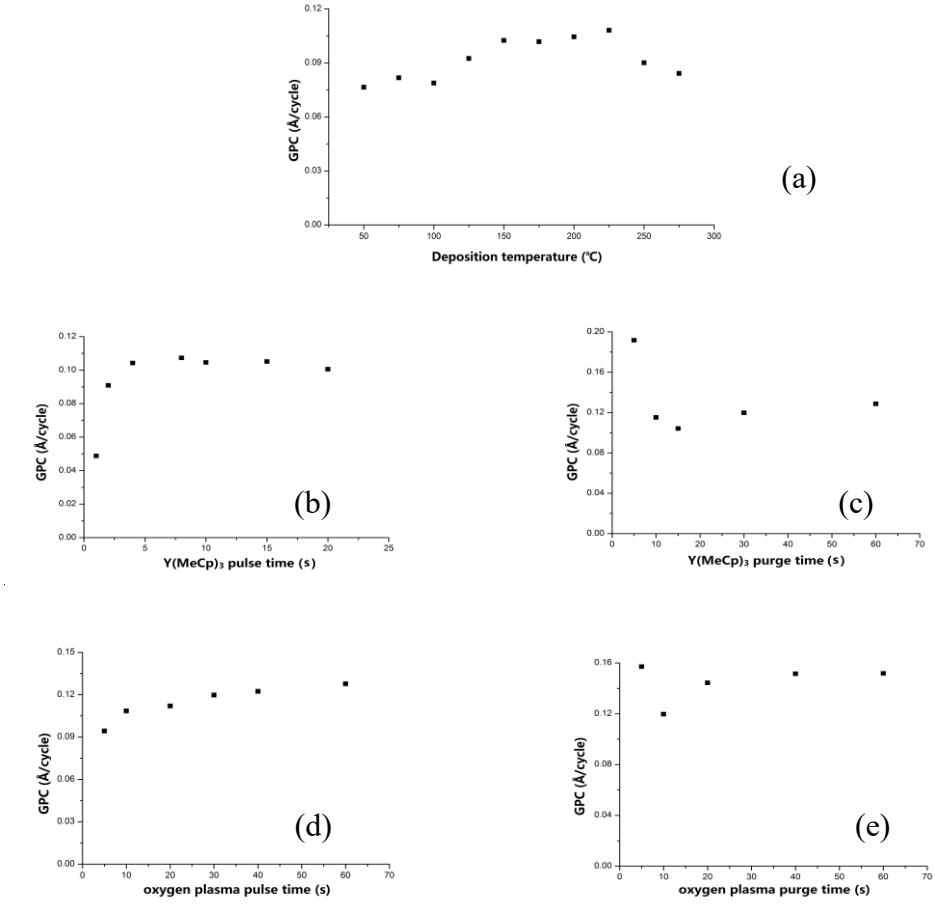

Figure 4.2. Y_2O_3 ALD growth saturation curves dependent on (a) substrate temperature T_{sub} ; (b) $Y(MeCp)_3$ pulse time t_1 ; (c) $Y(MeCp)_3$ purge time t_2 ; (d) oxygen plasma pulse time t_3 ; and (e) oxygen plasma purge time t_4.

The GPC obtained with the optimized recipe (t_1=4s, t_2=30s, t_3=30s, t_4=20s) was ~0.15 Å, much lower than those in the references in Table 4.1. Many investigators [4, 8-19] used higher precursor temperatures, leading to increased amount of precursor per unit pulse width. Although some references [5-7] used the same ampoule temperature setup for $Y(MeCp)_3$, the recipes being used were not optimized and may have introduced the possibility that CVD-like gas reactions were involved. For example, only 1s purge time was used to remove residues of 0.7s $Y(MeCp)_3$ pulse in Ref. [5], ozone was used as the oxidant in Ref. [6] and a bubbler (instead of an ampoule) was used in Ref. [7]. Considering the concentration of yttrium oxide in YSZ is usually lower than 10 mol% as mentioned in the section of introduction, the yttrium oxide GPC of 0.15 Å is high enough for applications to YSZ electrolyte materials. Furthermore, low GPC may enable access to lower concentration of yittria in zirconia than is commonly available in ALD.

4.3.2 Optical properties

The dispersion relationship used to analyze samples were briefly introduced in section 3.4.1. The dispersion functions of the Si(100) substrate and native oxide were loaded from the library of the software CompleteEASE. The n(λ) functions of Y_2O_3 thin films were approximated by Cauchy's polynomials

$$n(\lambda) = a + \frac{b}{\lambda^2} + \frac{c}{\lambda^4} \tag{4.4}$$

Figure 4.3 shows the dispersive n(λ) functions of Y_2O_3 thin films when deposition temperature varied from 100℃ to 225℃, with thickness of 2.4±0.3 nm. A bulk Y_2O_3 curve [22] is shown for comparison.

The results clearly showed that thin film samples have noticeably lower refractive indices than bulk materials. This is due to the thickness of the films, and has been observed in the literature [23]. The refractive index at 600 nm wavelength as a function of deposition temperature is shown in Figure 4.4. The lowest refractive index level of the sample deposited at 100℃ is accordant with a low density and a high porosity [24, 25], probably resulting from the incomplete reaction at this temperature. In the ALD window (150℃ to 225℃), there is a rising trend of refractive index as a consequent of the structures with coarser grains and fewer defects at high temperature. The refractive index of sample deposited at 125℃ is higher than those at either 100℃ or 150℃, probably because the incomplete ALD reaction at 125℃ leads to a dense structure.

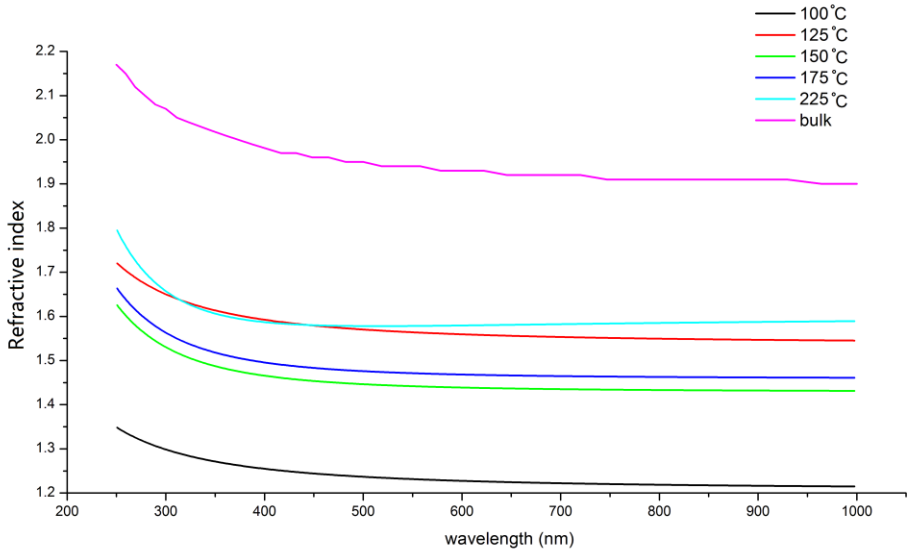

Figure 4.3. Ellipsometry measurements of the refractive index as a function of the wavelength λ.

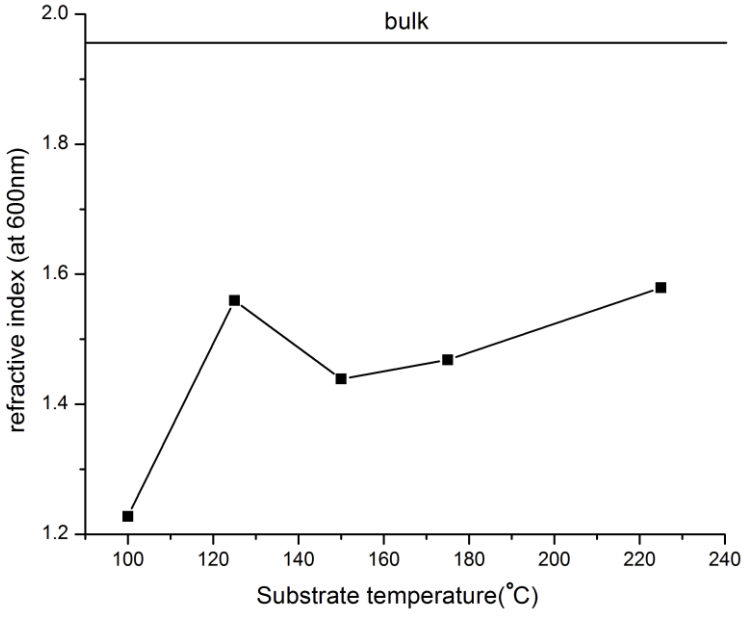

Figure 4.4. Refractive index versus substrate temperature at 600 nm wavelength.

4.3.3 Modeling of $Y(MeCp)_3$ vapor in ampoule

Three assumptions were made in the modeling of effusion and sublimation: (1) All the vapor gases are assumed to be ideal, (2) We only considered the effusion of $Y(MeCp)_3$ vapor molecules, and the inert gas Ar in the ampoule does not affect the effusion of $Y(MeCp)_3$. Considering the enormous size and weight differences between $Y(MeCp)_3$ and Ar, it is a plausible assumption, and (3) The effusion and sublimation process are governed by Knudsen effusion equation and sublimation equation.

The Knudsen effusion rate is given by the equation below [26]:

$$\frac{dm_{effusion}}{dt} = A * \sqrt{\frac{M_{molecule}}{2\pi RT}} * P \tag{4.1}$$

in which, A is the area of the effusing hole, $M_{molecule}$ is the molecular weight of the gas that is effusing, R is the ideal gas constant, T is the temperature, P is the vapor pressure in the ampoule.

The sublimation rate of precursor in the ampoule is described as [27]

$$\frac{dm_{sublimation}}{dt} = e^{-\frac{M_{molecule}u_0^2}{2RT}} * \sqrt{\frac{M_{molecule}}{2\pi RT}} * S * \left(P_{eq} - P\right), \tag{4.2}$$

where S is the surface area of the solid precursor material in the ampoule, $P_{equilibrium}$ is the pressure at temperature T, u_0 is the threshold velocity for the precursor molecules to evaporate, and the other parameters are mentioned above.

During the ALD process, the pressure inside the ampoule is changing with time during every ALD cycle if the vapor pressure of the metal precursor is low.

When precursor materials were initially installed into ampoules in a glove box at room temperature, the inert gas atmosphere is normally higher than 760 torr. For the first-time usage, the pressure within the ampoule is significantly higher than the line pressure (1 torr in our study). Therefore, the first-time usage is conducted to balance the pressure between line and the ampoule. After that, the ampoule pressure is slightly higher than the line pressure and ready to do ALD. The pressure change during ALD cycles is shown in Figure 4.5. Before the valve was open, the pressure inside the ampoule, P, is the sum of line pressure (P_{line}) and the equilibrium partial pressure of precursor vapor (P_{eq}). Once the valve is opened, $Y(MeCp)_3$ vapor molecules effuse out of the ampoule and into the Ar gas line, lowering the vapor partial pressure in the ampoule (P_p) resulting in a total pressure P very close to P_{line}. Increasing the valve opening time (t_1), the difference between P and P_{line} becomes more negligible. When the valve is closed, the $Y(MeCp)_3$ vapor pressure begins to increase. With enough time ($t_2+t_3+t_4$) P_P would recover to P_{eq}.

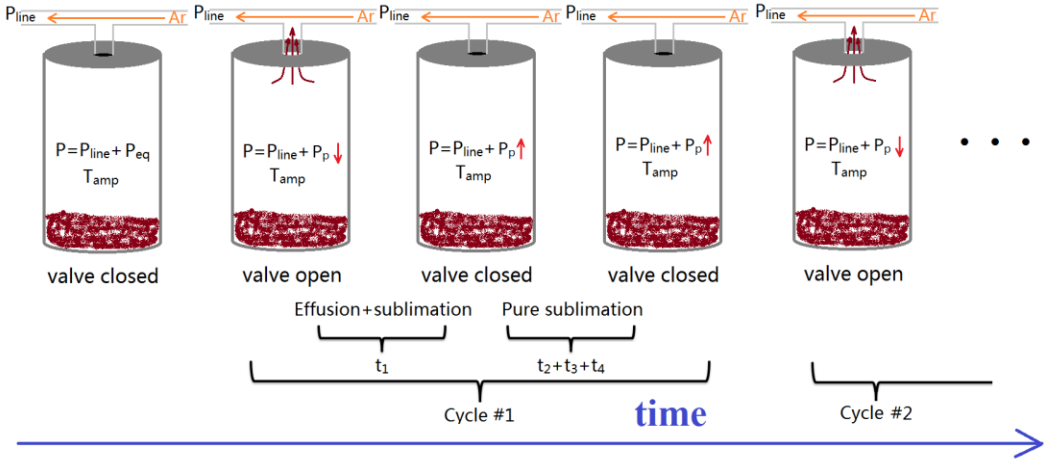

Figure 4.5. The ampoule pressure change with time as the ALD valve opens and closes during ALD cycles.

During the pulse time (t_1), effusion and sublimation occur at the same time. Based on equations (4.1) and (4.2), the mass change of $Y(MeCp)_3$ vapor inside the ampoule (dm) is the mass difference between effusion and sublimation, according to the following equation:

$$\mathrm{dm} = \left[e^{-\frac{M_{molecule} u_0^2}{2RT}} * \sqrt{\frac{M_{molecule}}{2\pi RT}} * S * \left(P_{eq} - P\right) - A * \sqrt{\frac{M_{molecule}}{2\pi RT}} * P \right] * dt \qquad (4.3)$$

During the remaining time ($t_2+t_3+t_4$) in every ALD cycle when the valve is closed, only sublimation occurs, so equation (4.2) can be used to describe the process during $t_2+t_3+t_4$. Thus, the relationship of time and $Y(MeCp)_3$ vapor mass inside the ampoule could be described by equations (4.3) and (4.2) during t_1 and $t_2+t_3+t_4$, respectively. Some known constants in equations (4.1) - (4.3) are as

followed. The molecular weight of $Y(MeCp)_3$ ($M_{molecule}$) is 325.9 g/mol. The area of the effusing orifice (A) is $3.2x10^{-5}$ m^2. The volume of the ampoule (V) is $5.0x10^{-5}$ m^3. The surface area of the solid precursor in the ampoule (S) is $7.6x10^{-4}$ m^2. The threshold velocity of molecules (u_0) is 24.4 m/s. The vapor pressures of $Y(MeCp)_3$ at different temperatures, obtained from Air Liquide [28], are shown below in Table 4.3.

Table 4.3. Vapor pressures of $Y(MeCp)_3$ at different temperatures [28]

Temperature (°C)	**Vapor pressure (torr)**
110	0.025
130	0.085
150	0.300
170	1.000
190	3.000

As mentioned in the discussion on the recipe optimization, the time between $Y(MeCp)_3$ pulses appear to affect GPC. The variations in the number of molecules effusing from the ampoule with cycles were determined by model calculations using the equations above. Although the correlation of the number of molecules and GPC is not simply linear, it is clear that more molecules would yield higher GPC when the substrate surface is not saturated. In Figure 4.6(a)-(c), t_1, t_4, and the ampoule temperature were the variables, respectively.

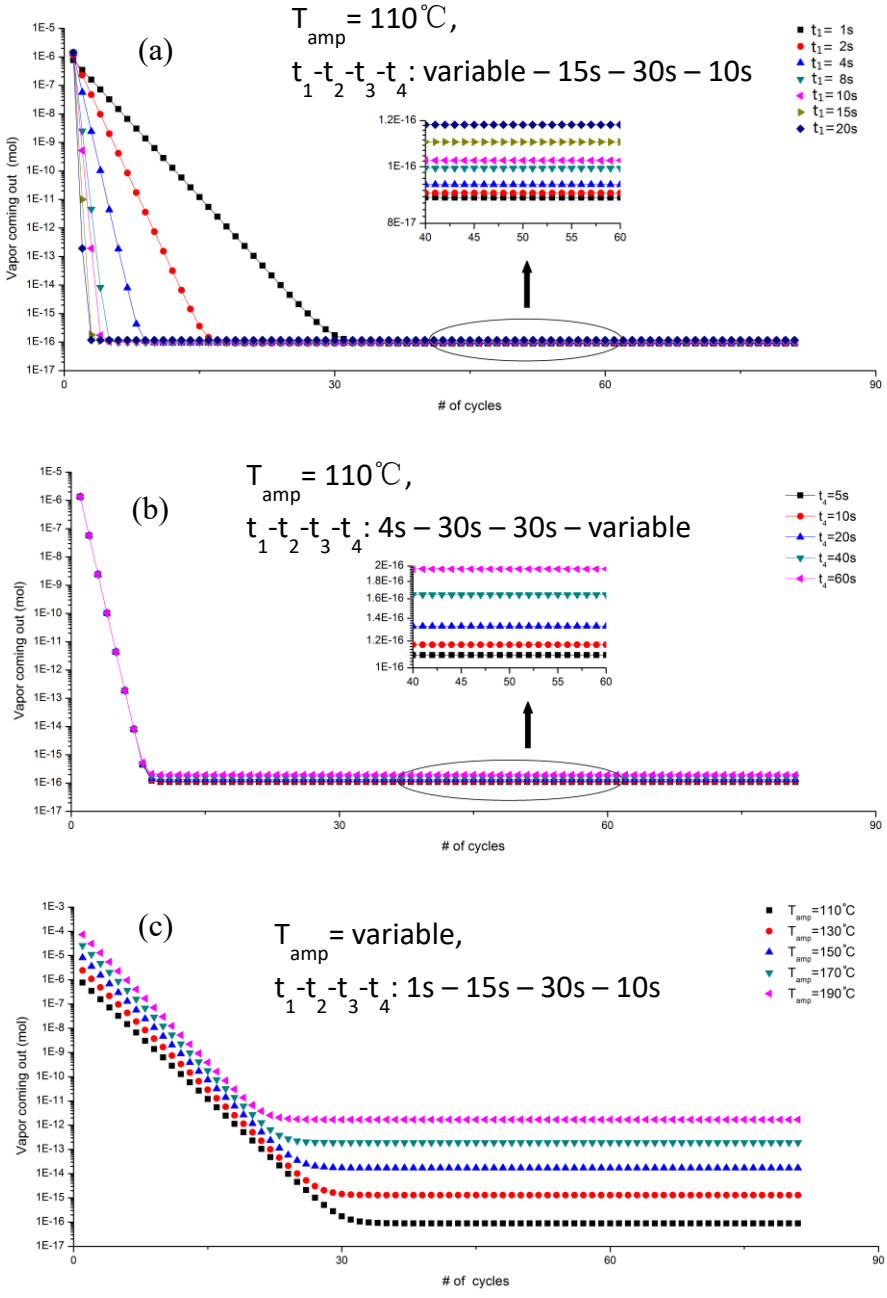

Figure 4.6. Variation of the molecule numbers effusing from the ampoule with cycles. (a) t_1, precursor pulse as the variable; (b) t_4, plasma purge as the variable; (c) ampoule temperature as the variable.

In Figure 4.6(a), a pattern is observed that is contrary to what is generally observed, that is, a longer pulse time leads to higher GPC. Here, a shorter pulse time (for example 1s) leads to a higher flux of molecules (which should lead to higher GPC if saturation has not been reached) to the substrate compared with a longer pulse time (for example 20s) during the first 30 cycles. This is explained by the fact that longer pulse times deplete the vapor pressure of $Y(MeCp)_3$ inside the ampoule more quickly, as seen in Figure 4.7. However, after the ~30th cycle the vapor coming out in all cases reached saturated values (Figure 4.6 (a-c)). At the same time, the ampoule pressures reached to a steady state.

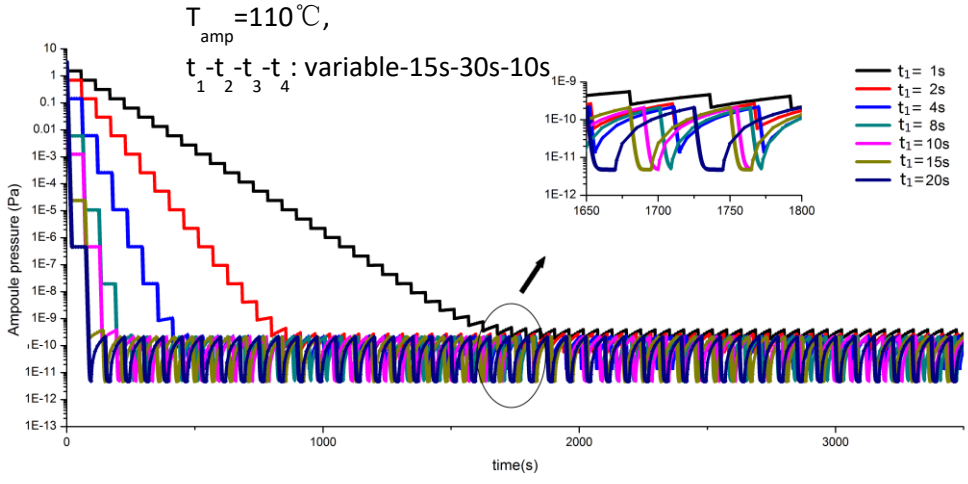

Figure 4.7. The modeling variations of precursor vapor pressure inside the ampoule with time when $Y(MeCp)_3$ pulse time (t_1) is the variable.

Figure 4.8 shows the experimental data obtained when t_1 was being optimized, and a similar pattern can be observed. The GPC of 20s pulse time was higher

than that of 4s pulse time in the first several cycles due to the ampoule vapor is abundant. From the eighth cycle to about fortieth cycle, the GPC of 4s pulse time is higher because the precursor vapor of 20s is consumed. This confirms the conclusion that calculating GPCs should be conducted after a number of initial cycles (~30) have passed so that ampoule vapor pressure has reached steady state. In the literature, GPC is often calculated using a simple method of differences in thickness divided by the total number of cycles (starting from the first cycle). This may lead to erroneous GPC values and could explain some of the results in which growth rate (Å/cycle) and total thickness decreased with increasing precursor pulse time, for example [29, 30].

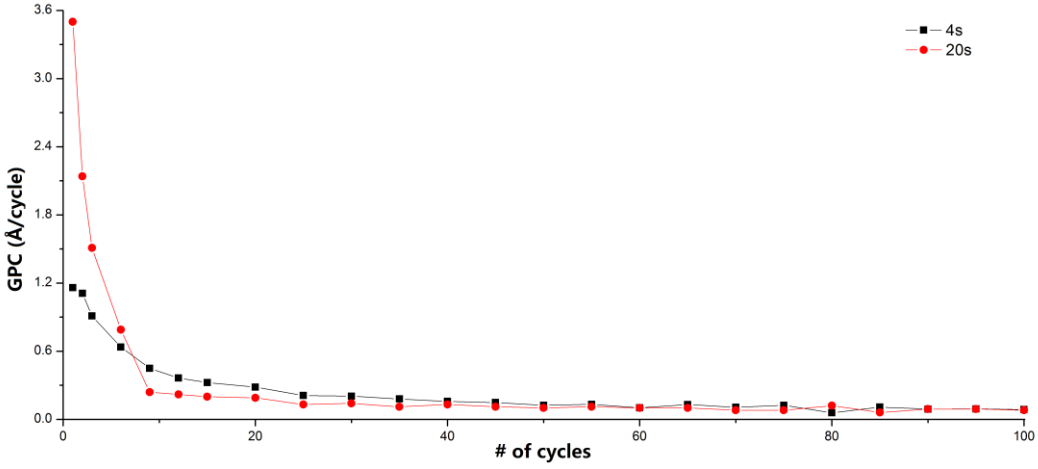

Figure 4.8. GPC variation with number of cycles in the optimizing t_1 cases of t_1= 4s and 20s.

The effect of t_2, t_3 and t_4 on precursor vapor pressure inside the ampoule is similar, and Figure 4.6(b) shows only the modeling results for t_4. A longer t_4 provided more time for the sublimation of the precursor, leading to higher vapor pressure in the ampoule and more molecules emanating from the ampoule per pulse resulting in a higher GPC. This is consistent with the experimental results shown in Figure 4.2.

Figure 4.6(c) shows the effect of ampoule temperature. Elevated ampoule temperatures provide higher vapor pressures not only for the initial pulse, but also at steady state. This illuminates why the GPC for Y_2O_3 PEALD varies over a wide range in the literature. From the modeling results, it is clear that in order to increase the GPC, increasing ampoule temperature is much more efficient than increasing precursor pulse time. A longer purge time providing a higher level of pressure recovery also works, but is not time-efficient.

It is noteworthy that the above statements are not valid for precursors with high vapor pressures. Trimethylaluminum (TMA), for example, is a high vapor pressure precursor and accordingly the number vapor molecules emanating from the ampoule is stable at high levels when the ampoule temperature and pulse time are only 20°C and 0.1s, respectively. The TMA curve is superimposed on the plot of Figure 4.6(c), as shown in Figure 4.9. It is clear that increasing the ampoule temperature of TMA would not improve GPCs of the saturated self-limiting ALD reaction but there would be a significant waste of precursor materials.

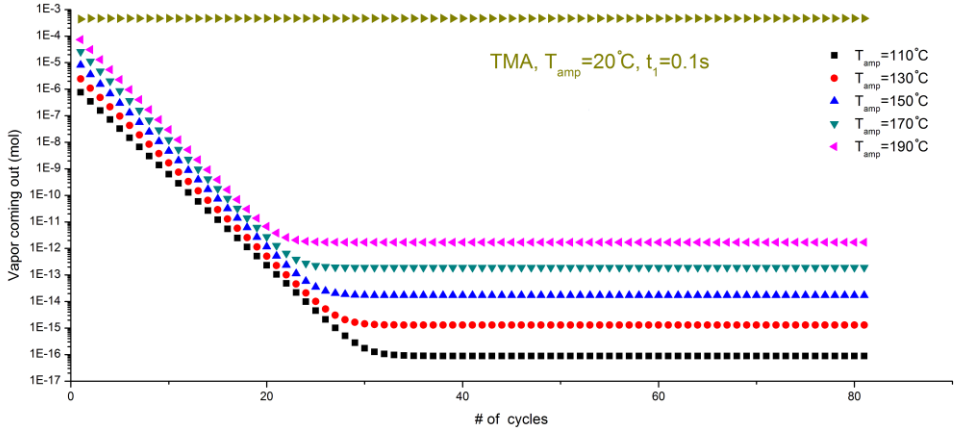

Figure 4.9. Variations of precursor vapors emanating from the ampoule with number of cycles of TMA, as a comparison to the $Y(MeCp)_3$.

High vapor pressure precursors are ideal for ALD nanolaminate composites application, but not suitable for ALD mixed or doped composites applications. In cases that high vapor pressure precursors are utilized, post-annealing is usually desired to form homogeneous mixed or doped composites, which is not necessary when using low vapor pressure precursors. Also, it is easy to obtain low concentration components in ALD composites by manipulating the pulse widths of precursors when using low vapor pressure ones.

4.4 Conclusions

We have investigated PEALD Y_2O_3 for YSZ composite thin films using $Y(MeCp)_3$ as the low vapor pressure precursor with ampoule temperature at 110℃. In-situ thickness characterization obtained from spectroscopic

ellipsometry during the growth was used to calculate GPCs. The GPC obtained with the optimized recipe was ~0.15 Å. Thin film samples in this study shown lower refractive index than that of bulk materials. When increasing deposition temperature within the ALD window (150℃ to 225℃), a rising trend of samples' refractive index is obtained because the structures at high temperature have coarser grains and fewer defects. A model based on Knudsen effusion and sublimation was introduced to describe the variation of precursor pressures inside the ampoule and number of vapor molecules emanating from ampoule during a pulse.

To conclude, the calculated results were consistent with experimental observation, proving that it is applicable in ALD studies of composite materials using precursors in low vapor conditions. Noteworthy, calculating GPCs of low vapor pressure precursors should be conducted after a number of initial cycles (~30) have passed so that ampoule vapor pressure has reached the steady state. Elongating other pulses that are part of the cycle provides a longer recovery time for precursor ampoule pressure, resulting in an improved GPC.

4.5 References

[1] Muneshwar, T., & Cadien, K. (2015). Influence of atomic layer deposition valve temperature on ZrN plasma enhanced atomic layer deposition growth.

Journal of Vacuum Science & Technology A: Vacuum, Surfaces, and Films, 33(6), 060603.

[2] Foroughi-Abari, A., & Cadien, K. (2012). Atomic layer deposition for nanotechnology. In Nanofabrication (pp. 143-161). Springer Vienna.

[3] Elam, J. W., & George, S. M. (2003). Growth of ZnO/Al2O3 alloy films using atomic layer deposition techniques. Chemistry of Materials, 15(4), 1020-1028.

[4] Shim, J. H., Park, J. S., An, J., Gür, T. M., Kang, S., & Prinz, F. B. (2009). Intermediate-temperature ceramic fuel cells with thin film yttrium-doped barium zirconate electrolytes. Chemistry of Materials, 21(14), 3290-3296.

[5] Niinistö, J., Putkonen, M., & Niinistö, L. (2004). Processing of Y2O3 thin films by atomic layer deposition from cyclopentadienyl-type compounds and water as precursors. Chemistry of materials, 16(15), 2953-2958.

[6] Niinistö, J., Kukli, K., Sajavaara, T., Ritala, M., Leskelä, M., Oberbeck, L., ... & Schröder, U. (2009). Atomic layer deposition of high-permittivity yttrium-doped HfO2 films. Electrochemical and Solid-State Letters, 12(1), G1-G4.

[7] Roessler, T., Gluch, J., Albert, M., & Bartha, J. W. (2010). Electrical characterisation of HfYO MIM-structures deposited by ALD. Thin Solid Films, 518(16), 4680-4683.

[8] Shim, J. H., Chao, C. C., Huang, H., & Prinz, F. B. (2007). Atomic layer deposition of yttria-stabilized zirconia for solid oxide fuel cells. Chemistry of Materials, 19(15), 3850-3854.

[9] Su, P. C., Chao, C. C., Shim, J. H., Fasching, R., & Prinz, F. B. (2008). Solid oxide fuel cell with corrugated thin film electrolyte. Nano letters, 8(8), 2289-2292.

[10] Chao, C. C., Park, J. S., Tian, X., Shim, J. H., Gür, T. M., & Prinz, F. B. (2013). Enhanced oxygen exchange on surface-engineered yttria-stabilized zirconia. ACS nano, 7(3), 2186-2191.

[11] Chao, C. C., Hsu, C. M., Cui, Y., & Prinz, F. B. (2011). Improved solid oxide fuel cell performance with nanostructured electrolytes. ACS nano, 5(7), 5692-5696.

[12] Su, P. C., & Prinz, F. B. (2012). Nanoscale membrane electrolyte array for solid oxide fuel cells. Electrochemistry Communications, 16(1), 77-79.

[13] Shim, J. H., Kang, S., Cha, S. W., Lee, W., Kim, Y. B., Park, J. S., ... & An, J. (2013). Atomic layer deposition of thin-film ceramic electrolytes for high-performance fuel cells. Journal of Materials Chemistry A, 1(41), 12695-12705.

[14] Chao, C. C., Kim, Y. B., & Prinz, F. B. (2009). Surface modification of yttria-stabilized zirconia electrolyte by atomic layer deposition. Nano letters, 9(10), 3626-3628.

[15] Motoyama, M., Chao, C. C., An, J., Jung, H. J., Gür, T. M., & Prinz, F. B. (2013). Nanotubular array solid oxide fuel cell. ACS nano, 8(1), 340-351.

[16] Shim, J. H., Chao, C. C., Huang, H., & Prinz, F. B. (2007). Atomic layer deposition of yttria-stabilized zirconia for solid oxide fuel cells. Chemistry of Materials, 19(15), 3850-3854.

[17] Cho, G. Y., Noh, S., Lee, Y. H., Ji, S., & Cha, S. W. (2014). Study of Y2O3 thin film prepared by plasma enhanced atomic layer deposition. ECS Transactions, 64(9), 15-21.

[18] Yu, W., Ji, S., Cho, G. Y., Noh, S., Tanveer, W. H., An, J., & Cha, S. W. (2015). Atomic layer deposition of ultrathin blocking layer for low-temperature solid oxide fuel cell on nanoporous substrate. Journal of Vacuum Science & Technology A: Vacuum, Surfaces, and Films, 33(1), 01A145.

[19] Ji, S., Cho, G. Y., Yu, W., Su, P. C., Lee, M. H., & Cha, S. W. (2015). Plasma-enhanced atomic layer deposition of nanoscale yttria-stabilized zirconia electrolyte for solid oxide fuel cells with porous substrate. ACS applied materials & interfaces, 7(5), 2998-3002.

[20] George, S. M. (2009). Atomic layer deposition: an overview. Chemical reviews, 110(1), 111-131.

[21] Muneshwar, T., & Cadien, K. (2015). Low temperature plasma enhanced atomic layer deposition of conducting zirconium nitride films using tetrakis

(dimethylamido) zirconium and forming gas (5% H2+ 95% N2) plasma. Journal of Vacuum Science & Technology A: Vacuum, Surfaces, and Films, 33(3), 031502.

[22] Nigara, Y. (1968). Measurement of the optical constants of yttrium oxide. Japanese Journal of Applied Physics, 7(4), 404.

[23] Motamedi, P., Dalili, N., & Cadien, K. (2015). A route to low temperature growth of single crystal GaN on sapphire. Journal of Materials Chemistry C, 3(28), 7428-7436.

[24] Alarcon-Flores, G., Aguilar-Frutis, M. I. G. U. E. L., García-Hipolito, M. A. N. U. E. L., Guzman-Mendoza, J., Canseco, M. A., & Falcony, C. (2008). Optical and structural characteristics of Y2O3 thin films synthesized from yttrium acetylacetonate. Journal of Materials Science, 43(10), 3582-3588.

[25] Wiktorczyk, T., Biegański, P., & Serafińczuk, J. (2016). Optical properties of nanocrystalline Y 2 O 3 thin films grown on quartz substrates by electron beam deposition. Optical Materials, 59, 150-156.

[26] Hollahan, J. R. (1962). Molecular effusion: Its newer features and applications. J. Chem. Educ, 39(1), 23.

[27] Miyamoto, S. (1933). A theory of the rate of sublimation. Transactions of the Faraday Society, 29(140), 794-797.

[28] https://www.electronics-airliquide.com/our-brands/aloha

[29] Kukli, K., Ritala, M., Pore, V., Leskelä, M., Sajavaara, T., Hegde, R. I., ... & Aspinall, H. C. (2006). Atomic Layer Deposition and Properties of Lanthanum Oxide and Lanthanum-Aluminum Oxide Films. Chemical Vapor Deposition, 12(2-3), 158-164.

[30] Triyoso, D. H., Hegde, R. I., Grant, J. M., Schaeffer, J. K., Roan, D., White Jr, B. E., & Tobin, P. J. (2005). Evaluation of lanthanum based gate dielectrics deposited by atomic layer deposition. Journal of Vacuum Science & Technology B: Microelectronics and Nanometer Structures Processing, Measurement, and Phenomena, 23(1), 288-297.

Chapter 5

Plasma Enhanced ALD of Low Yttria Concentration YSZ Thin Films with High Oxygen Ionic Conductivity

5.1 Introduction

As mentioned in chapter 2, lowering the operating temperature of SOFCs into IT-SOFCs range has attracted much interest worldwide for benefits of longer lifetime, and lower cost with the possibility of using cheaper construction materials [1]. One of the major challenges in this IT range is the ohmic loss of electrolytes, which makes it critical to increase their ionic conductivity [2]. Decreasing the thickness of electrolytes can lead to quicker ion diffusion and lower ohmic losses [3], and it is crucial to keep thin electrolytes fully dense to minimize reactant cross-over [4] at the same time. As a thin film technique, yielding conformal and pinhole-free films, ALD has been considered as a promising candidate [5].

Plentiful efforts [6-30] using ALD have been made to investigate YSZ, which is the most popular zirconia-based electrolyte material in SOFCs for its high ionic conductivity, good stability and outstanding compatibility with electrode materials [31, 32]. Most of the researchers [7-29] used $Y(MeCp)_3$ as the yttrium

precursor and $Zr(NMe_2)_4$ as the zirconium precursor. Others used $Y(thd)_3$ [6, 7] or $Y(EtCp)_3$ [30] and Cp_2ZrCl_4 [6], $Cp_2Zr(CH_3)_2$ [6], $Zr(thd)_4$ [6], or $ZrCl_4$ [7] as precursors. In all cases [6-30], the concentrations of yttrium oxide in YSZ were controlled by the ratio of yttrium oxide cycles and zirconium oxide cycles in one ALD super-cycle. The fact that vapor pressure of yttrium precursors is usually very low requires a high temperature condition of the yttrium precursor ampoule to provide enough amounts of vapor for reactions. For example, the ampoule temperature of the most commonly used one $Y(MeCp)_3$, was set as high as 190℃ in many studies [8-16, 23-25]. High temperature introduces a risk of thermal decomposition, which causes gas reactions and compromises the film quality. The elevated vapor pressure at high temperature increases the waste amount of precursors, especially considering the fact that mostly the concentration of yttrium oxide needed in YSZ is below 10 mol%. Also, annealing is usually needed to eliminate the heterogeneous distribution of yttrium oxide in this method of ALD YSZ fabrication.

In the previous chapter, it has been shown that ALD of yttrium oxide using $Y(MeCp)_3$ in a low vapor pressure condition is applicable for the application of YSZ electrolyte in SOFCs. In this chapter, a new ALD recipe was introduced. The yttrium oxide concentrations in YSZ were manipulated by the pulse width of yttrium precursor in one ALD cycle. As a result, yttrium oxide is homogeneously distributed in the YSZ thin films.

5.2 Experimental

The concentrations of yttrium oxide in YSZ were controlled by the pulse time of yttrium precursor in one ALD cycle, rather than the ratio of zirconium oxide and yttrium oxide cycles. The pulsing sequence of ALD cycles used in this study is shown in Figure 5.1. First, the vapors of yttrium precursor were introduced by short pulses (pulse time of the yttrium precursor, t_1), varied from 1s to 20s. After the following purge pulse t_2 of 15s, 0.1s long of zirconium precursor pulse t_3 was introduced. Another purge pulse t_4 of 10s followed, and then 10s oxygen gas was introduced (pulse time of the oxygen plasma, t_5) into the reaction chamber followed by the ICP plasma ignition. Finally, another purge time (t_6) of 10s was to remove the by-products and oxygen gas residue. In this way, the pulse length of t_1 determines the amount of yttrium precursor molecules adsorbed on the substrate. The remaining active sites at which could be adsorbed were bonded with zirconium precursor with a long enough pulse 0.1s. All the parameters are summarized in Table 5.1.

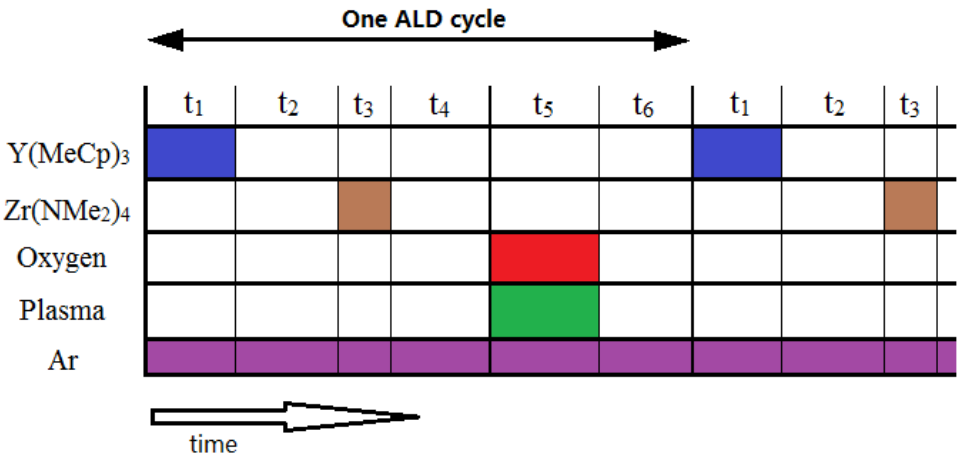

Figure 5.1. The pulsing sequence of ALD cycles.

Table 5.1. Parameters setting of ALD YSZ

t_1(s)	t_2(s)	t_3(s)	t_4(s)	t_5(s)	t_6(s)
variable	fixed	fixed	fixed	fixed	fixed
1-20	15	0.1	10	10	10

With this method, the yttrium oxide is homogeneously distributed in every single molecular layer and throughout the thickness of obtained YSZ thin films, in contrast to the heterogeneous distribution by the conventional method, as shown in Figure 5.2. Therefore, post-annealing is not necessary to homogenize the distribution of yttrium oxide.

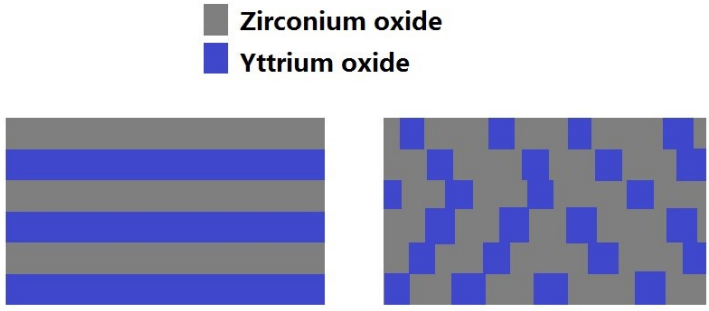

(a) (b)

Figure 5.2. Structural differences of ALD YSZ films made by (a) conventional method and (b) method in this study.

5.3 Results and Discussion

5.3.1 ALD growth of YSZ

100 cycles were run in each recipe. Figure 5.3 shows the GPC versus the pulse time of yttrium precursor in one ALD super cycle. The GPC of a pure zirconium oxide deposition (t_1=0) was imposed in the plot as a reference. From the figure a pattern can be observed that with increasing yttrium precursor pulse time, the GPC decreased from 1.35 Å/cycle to 1.15 Å/cycle. This GPC range is close to 1 Å/cycle [22] and 1.4 Å/cycle [25, 27] from references, and it is lower than the 2 Å/cycle GPC in researches [8-12] with an “exposure mode” [12] being used. In the investigation of Kim [21], the GPCs when using oxygen as oxidant was 0.6 Å/cycle. The almost doubled GPC in this research is probably because of the high reactivity of plasma.

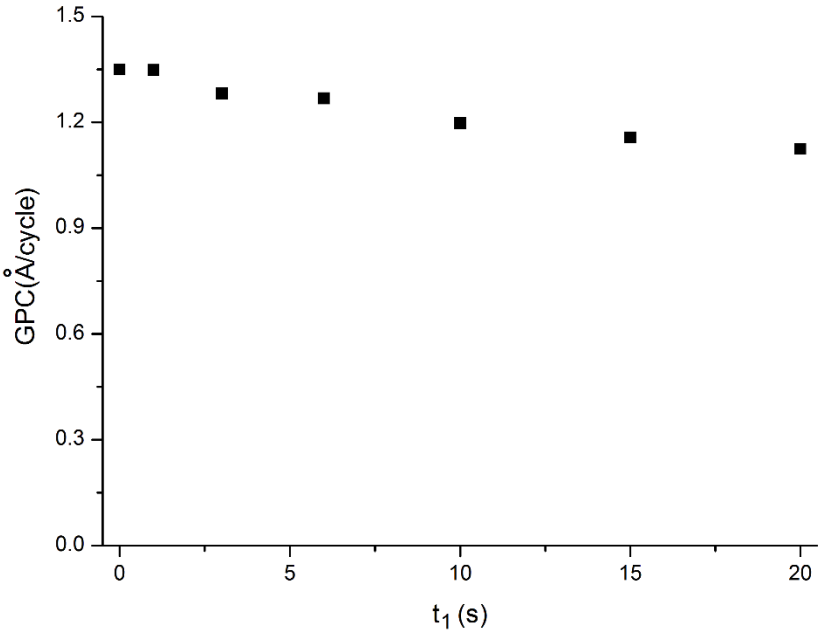

Figure 5.3. The growth per cycle (GPC) when using different yttrium precursor pulse in one ALD cycle.

To understand the pattern in Figure 5.3, an explanation can be made. Although ALD is a self-limiting surface growth technique, in practical after each precursor pulse the active sites on substrates are not completely covered due to the steric hindrance. In this study, after the first pulse of yttrium precursor, some active sites on the surface were occupied, leaving a limited number of sites to the following pulse of zirconium precursor. The number of remaining adsorption sites decreased with elongating yttrium precursor pulse time, leading to a lower GPC owing to the fact that yttrium precursor has a bigger molecular size than that

of zirconium precursor. A density functional theory (DFT) calculation of $Zr(NMe_2)_4$ and $Y(MeCp)_3$ geometry optimization was conducted with Vienna Ab initio Simulation Package (VASP). In this optimization, the density functional with DFT exchange-correlation GGA-PBA was used. The integration scheme was Methfessel-Paxton smearing with width of smearing 0.2eV as default. A conjugate-gradient algorithm is used to relax the ions. Plane cutoffs for $Zr(NMe_2)_4$ and $Y(MeCp)_3$ calculations were 400 eV and 500 eV, respectively. The results showed greatest distances of yttrium and zirconium atoms to carbon atoms are 0.4 nm and 0.3 nm, respectively, indicating that $Y(MeCp)_3$ has a larger molecular size than $Zr(NMe_2)_4$.

5.3.2 Compositional analysis and ionic conductivity of YSZ

The conductivities of ALD YSZ thin films with different yttrium precursor pulse time at 400℃, 500℃, and 600℃ are shown in Figure 5.4. A commercial bulk 8YSZ sample from FCM (Fuelcellmaterials.com) was tested for comparison, with a thickness of 0.275±0.025 mm. It can be seen that ALD YSZ thin films with yttrium pulse higher than 6s exhibited higher levels of conductivity than that of the commercial bulk 8YSZ, and that conductivities in all cases increased with rising the temperature. For ALD YSZ thin films, the conductivity increased with longer t_1, resulting from the fact that longer pulses leading to higher concentrations of yttrium oxide in the YSZ thin films. When t_1

was at 15s, the conductivity reached the maximum. Beyond that, the conductivity of 20s t_1 dropped slightly.

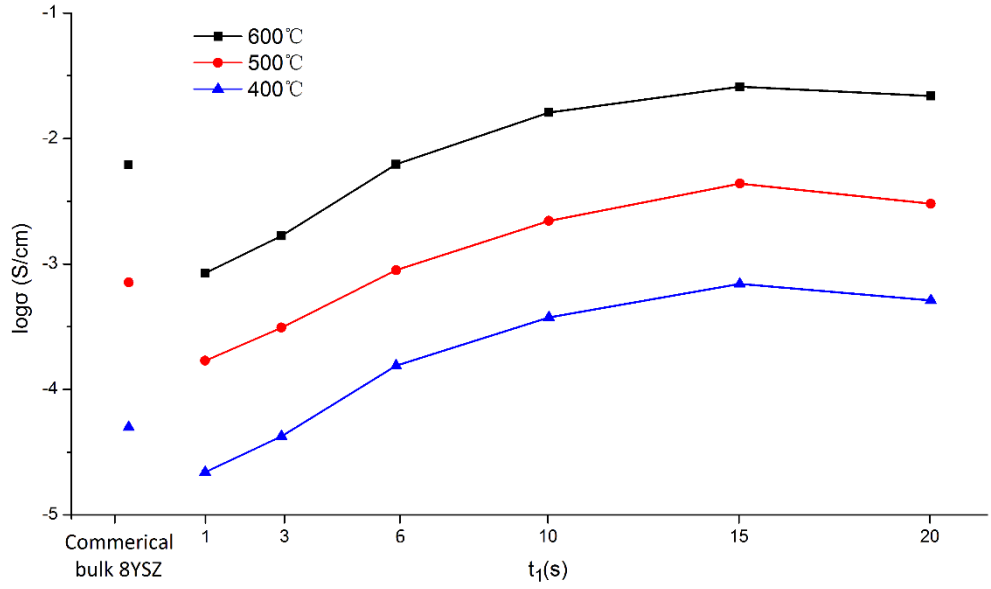

Figure 5.4. Ionic conductivity of samples with different yttrium precursor pulse time and commercial bulk 8YSZ at 400°C, 500°C, and 600°C.

It can be seen from Figure 5.5 that the concentrations of yttrium oxide in YSZ increased with longer t_1 as expected. Yttrium oxide concentration of the 15s t_1 sample was 1.6 mol%, instead of the commonly accepted 8 mol% or 10 mol% for ALD YSZ [9]. In the study of Son [9], 10YSZ shows the highest conductivity as a result of the inhomogeneous distribution of yttrium oxide in the vertical direction of ALD YSZ films, rather than the homogenous doping of bulk YSZ or the YSZ thin films in this study. Ramamoorthy [33] found 3YSZ showed the highest ionic conductivity, attributing it to the effect of grain size. The conclusion

Ramamoorthy [33] made is that the concentration of yttrium oxide in YSZ for coarse-grained YSZ is 8YSZ and for nanocrystalline YSZ is 3YSZ due to the fact that grain boundary effect is dominant in nanocrystalline YSZ. YSZ thin films obtained in this study were determined to be nanocrystalline from the AFM results in section 5.3C.

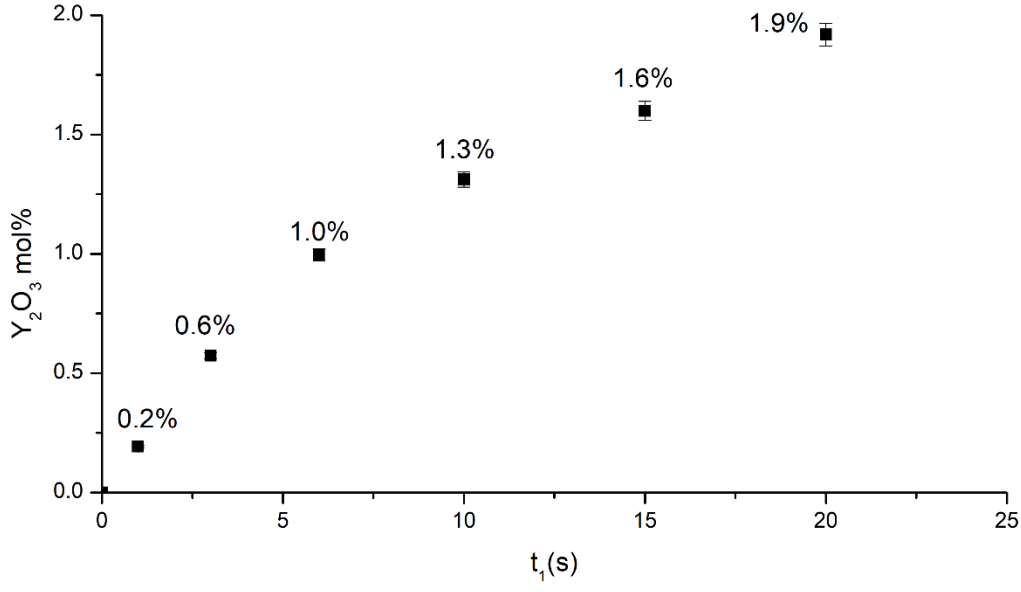

Figure 5.5 Yttrium oxide concentrations in YSZ obtained from different yttrium precursor pulse width.

Peters [34] made an explanation about why YSZ with 8 mol% yttrium oxide shows the highest ionic conductivity for bulk YSZ. When the concentration of Y_2O_3 is lower than 8 mol%, more oxygen vacancies are created with increasing the concentration of Y_2O_3, which is also the conduction mechanism of YSZ. When increasing the Y_2O_3 concentration above 8 mol%, the strong Coulombic

interactions among oxygen vacancies act as a barrier for oxygen ionic conduction, leading to a lower conductivity.

When the grain size goes down to nano-scale, however, the true size effect [35] plays an important role in ionic conductivity of YSZ. The core-space charge layer model [35] was introduced to illustrate the true size effect. According to the model, a grain boundary consists of a grain boundary core and two adjacent SCLs. In the cases that the grain boundary cores are negatively charged, the density of oxygen vacancy increases in SCLs. When the thickness of SCL is high and comparable to the grain size, the ionic conductivity would be improved significantly. According to the definition of Debye length and its correlation with SCL, we can have the following equation of SCL thickness (λ) [36],

$$\lambda = \sqrt{\frac{2\varepsilon_r \varepsilon_0 \Delta\varphi(0)}{ne}} \tag{5.1}$$

where ε_r is the dielectric constant, ε_0 is the permittivity of free space, $\Delta\varphi(0)$ is the grain-boundary space-charge potential, n is the concentration of mobile oxygen vacancies, and e is the elementary charge. From the equation (5.1) it can be observed that SCL width is dependent on the dielectric constant of YSZ thin films, ultimately dependent on yttrium dopant level. Fabbri [37] found that thicker SCLs can be achieved when the electrolyte materials are more lightly doped. In the case of YSZ, lower yttrium dopant level leads to a lower oxygen vacancy concentration n and a denser structure considering the fact that yttrium

ions have lower mass and bigger radius than those of zirconium ions. As a result, SCL thickness in YSZ decreases with increasing yttrium dopant level. For example, SCLs of 8YSZ at 500℃ only exhibited a thickness of 1-4 Å [37].

The lattice mismatch between YSZ thin films and substrates is able to affect the conductivity as well. For a small mismatch, the strain deriving from the lattice constants difference is completely compensated by local elastic strain, forming a coherent interface; while for a large mismatch, it is partially or fully released by the formation of dislocations, generating an incoherent interface [37]. Kosacki [38] deposited YSZ on MgO substrates and a significant enhancement in ionic conductivity was observed. The improvement was ascribed to the mismatch between YSZ and MgO. Janek [39, 40] developed a model to represent the conductivity enhancement in an ionic conductor/insulating substrate system. There is a linear dependence of the logarithm of the interfacial conductivity on the lattice misfit, as followed

$$ln\frac{\sigma_{int}}{\sigma_{bulk}} \sim \Delta V_V^M f_{12} \tag{5.2}$$

where $\sigma_{int}/\sigma_{bulk}$ is the ionic conductivity ratio between the interface area and bulk materials, ΔV_V^M is the volume of migration for the oxygen vacancies, and f_{12} is the lattice mismatch between the ionic conductor and the insulating substrate. The value of ΔV_V^M depends on the local deformation of the lattice during the conduction process. In the case of oxygen ionic conduction in YSZ, it is always

positive. Therefore, only when the conductor is under tensile strain, which means it is showing an appreciably smaller lattice constant than that of the substrate (f_{12}>0), an improved ionic conductivity can be obtained [41]. However, YSZ can be closely matched in the lattice constant to Si(100) substrates [42]. The lattice constants [43, 44] of Si(100) substrates and YSZ are 5.43 Å and 5.14 Å, respectively. Although Putkoneon [6] found the lattice constant of ALD YSZ thin films is different from that of bulk YSZ, in the range from 5.09 Å to 5.28 Å, it is still well matching the lattice constant of Si(100) substrates, with a mismatch from 2.76% to 6.26%. Therefore, in this study the lattice mismatch between ALD YSZ and substrates only plays a negligibly minor role in the conductivity enhancement.

Based on the discussion above, a possible explanation of YSZ with 1.6 mol% yttrium oxide exhibiting the highest ionic conductivity can be made. When yttrium oxide concentration was lower than 1.6 mol%, on one hand, the oxygen vacancies produced by introducing yttrium oxides was limited. Therefore, even though the SCLs in the true size effect are wide the conductivity decreased. On the other hand, when yttrium oxide concentration was higher than 1.6 mol%, more oxygen vacancies were introduced by dopant Y_2O_3. However, the SCLs width in the true size effect reduced to some extent at the same time, and consequently the improvement true size effect became weak. As a result, a low conductivity was observed.

Figure 5.6 is the Arrhenius plot of measured ionic conductivity, and the data of 8YSZ in literature were superimposed as references. It can be seen that the performance of samples in this thesis is better than most of the 8YSZ samples in references. From Figure 5.6 the activation energies of oxygen ionic conduction in each case can be obtained, as summarized in Table 5.2. The activation energies of all ALD YSZ thin films are about 1 eV, lower than that of the commercial bulk 8YSZ. Son [9] obtained high activation energies from ALD YSZ thin films, in the range from 1.1 eV to 1.26 eV. Son [9] ascribed it to the inhomogeneous doping of yttrium oxide resulting from the characteristics of ALD process. The ALD recipe used in this study yielded homogeneously distributed dopants, and it is possibly responsible for the low level of activation energies.

Activation energies of YSZ electrolytes mentioned in literature [12, 45, 46] are smaller than 1.0eV, usually in the range from 0.8eV to 0.9eV due to the high characterization temperature. For example, in a study of Zhang [47], the activation energies of 8YSZ gained at 600 ℃ to 700 ℃ and 700 ℃ to 1000 ℃ were 1.14 eV and 0.85 eV, respectively. Kosacki [38] claimed that when ionic conductivity test is being conducted at high temperature levels (above 650℃), the activation energy of oxygen ionic conduction in YSZ is lower than 1.0 eV, typically 0.9 eV. When the characterization temperature is at low levels (below 650℃), activation energies are commonly higher than 1.0 eV. According to Kosacki [38] and Ramamoorthy [33], the increase in activation energy at lower

temperatures due to the formation of vacancy clusters and defects association in YSZ at test temperatures.

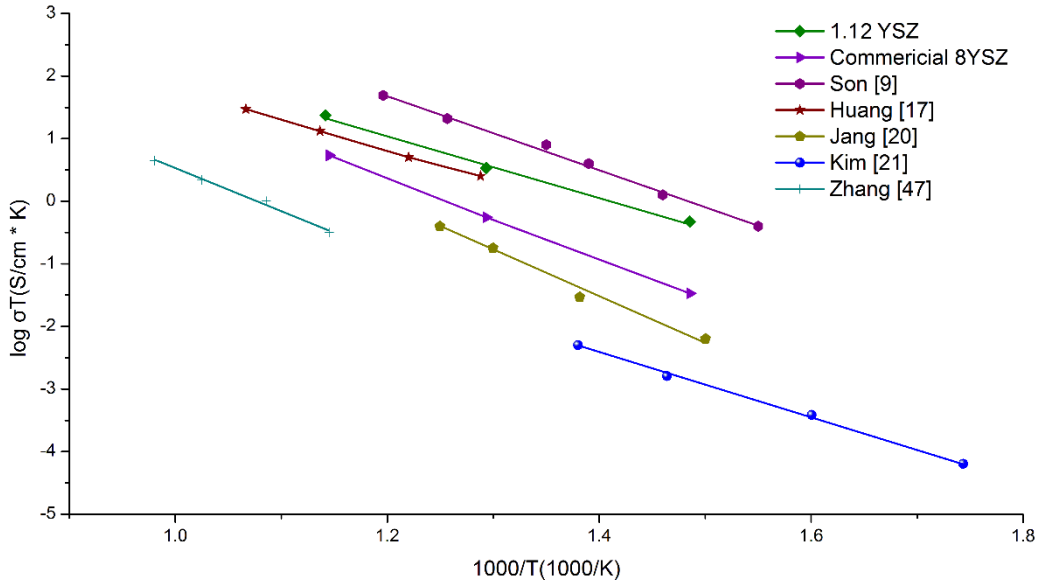

Figure 5.6. Arrhenius plot of the measured ionic conductivity of ALD YSZ samples with different yttrium precursor pulse time in comparison with the commercial bulk 8YSZ and reference data [9, 17, 20, 21, 47].

Table 5.2. Summary of activation energies of oxygen ionic conductance.

t_Y=1s	t_Y=3s	t_Y=6s	t_Y=10s	t_Y=15s	t_Y=20s	Commercial 8YSZ
0.99eV	1.00eV	0.99eV	1.01eV	0.98eV	1.01eV	1.28eV

5.3.3 Optical properties of YSZ thin films

The dispersion functions of substrate Si(100) and native oxide were loaded from the library of the software CompleteEASE. The n(λ) functions of YSZ thin films were approximated by Cauchy's polynomials, described in equation (4.4). The dispersion n(λ) functions of samples with thickness of 12.5±0.5 nm are shown in Figure 5.7. The refractive indices of bulk 12YSZ [48], 3YSZ and 8YSZ thin films [49] at 600 nm are superimposed for comparison.

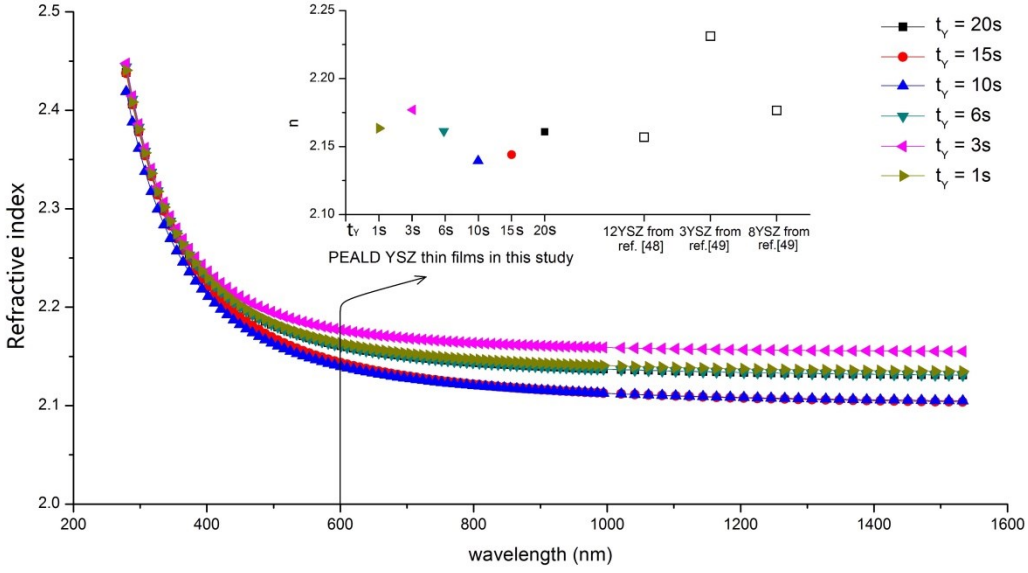

Figure 5.7. Ellipsometry measured refractive index as a function of the wavelength λ and values at 600 nm wavelength.

From Figure 5.7 it can be seen that the refractive indices of YSZ thin film samples are similar to bulk 12YSZ [48] and 8YSZ thin film [49], slightly lower

than that of 3YSZ thin film [49]. It proves that the oxygen vacancy concentrations in these ALD YSZ thin films are comparable with those of bulk 12YSZ and 8YSZ thin film. This finding supports the samples' outstanding electrical properties described in section 5.3C. In literature [49-51], a decreasing trend of YSZ thin films' refractive index with higher concentrations of yttrium oxide was observed. Xiao [49] explained on the one hand, yttrium ions have lower mass and bigger radius than those of zirconium ions; on the other hand, yttrium ions introduce vacancies due to the valence states difference between yttrium and zirconium ions. However, from Figure 5.7 it can be seen that the correlation between Y_2O_3 concentrations in YSZ thin films and their refractive indices is not obvious. The possible explanation is that there is an effect of dislocations and other crystalline defects in samples on the refractive index.

5.3.4 Microstructural and crystallinity characterization

XRD measurement was conducted for both as-deposited and annealed ALD YSZ thin film with 15s t_1, and the results are shown below in Figure 5.8. For the as-deposited film, no noticeable peak was detected. After annealing, characteristic peaks of YSZ can be seen clearly. In section 5.3B, it has been observed that as-deposited YSZ thin films exhibited high ionic conductivities. Therefore, in order to understand the crystalline structure of samples under electrical measurement condition, the XRD pattern of the as-deposited sample

after electrical test was added in Figure 5.8. Clear characteristic peaks were detected, proving that the ALD-YSZ thin films are crystalline during the electrical measurement.

In some studies [12, 24, 26], as-deposited ALD YSZ thin films were already crystalline without any annealing treatment probably because the high deposition temperature. However, it is possible as-deposited samples are crystalline, and no obvious peak presence is because of the weak signals being obtained from low thickness samples. It is supported by the observation of Lin [52] that a significant decrease of XRD peak heights was observed when lowering the sample thickness. In the study of Putkonen [6], the peaks of (111), (220) and (311) were observed only after the thickness of YSZ thin films increased to a certain level.

According to Miikkulainen [53], there is a threshold thickness for ALD to form crystalline ZrO_2. In Miikkulainen's review, the threshold thickness for zirconia is a function of temperature, as shown in Figure 5.9. The substrate temperature in this study was 150℃, and the thickness of XRD tested crystalline sample was 14.7 nm. It can be seen that the condition point (150℃, 14.7 nm) is lower than the threshold thickness to form crystalline. However, varying precursor and substrate materials would yield different threshold thickness. In the same review paper of Miikkulainen [53], it has been mentioned that the threshold value is different when ZrI_4 was used as the precursor material instead of $ZrCl_4$. Kukli [54] attributed the variation to the differences of chemical mechanism of

the crystal growth, kinetics of the phase formation, effect of grain size, and mobility of surface species affecting the nucleation density. Also, the introduction of yttrium oxide dopant would affect the threshold values.

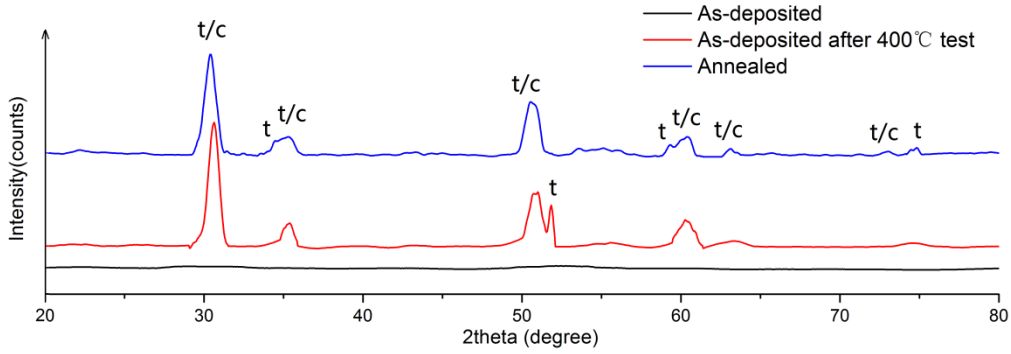

Figure 5.8. XRD patterns of as-deposited and annealed ALD YSZ thin films.

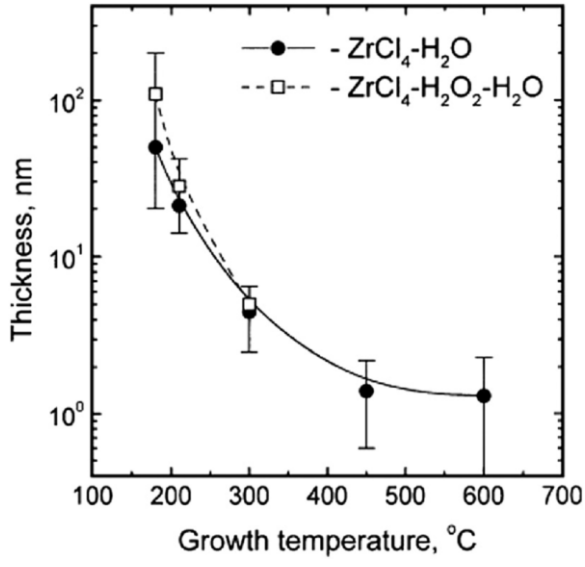

Figure 5.9. The threshold thickness to form ALD ZrO_2 crystallites as a function of temperature [53].

The peaks in Figure 5.8 matched the standard pattern of tetragonal phase (PDF#48-0224), proving the existence of tetragonal phase. However, all the peaks of zirconia cubic diffraction pattern exist in the tetragonal phase diffraction pattern. Therefore, it might be misleading to identify the phase is pure tetragonal according to Figure 5.8. It is noteworthy that the peak at ~30° of the after test as-deposited sample was shifted to higher angles compared with that of the annealed sample. It is probably because lattice parameter difference between tetragonal and cubic phase. The lattice parameter of cubic phase is ~0.517 nm; while the lattice parameters of tetragonal phase are a = 0.361 nm & c = 0.517 nm. There is less cubic phase in the after test as-deposited sample so that it has a low d-spacing and consequently a shift to higher angles was observed. According to the ZrO_2-Y_2O_3 phase diagram [34] Figure 2.2(b), the corresponding phase of 1.6 mol%Y2O3 YSZ at room temperature is pure monoclinic phase. Miikkulainen [53] observed the dependence of phase existence on thickness as a result of energy level variation of ALD thin film materials, which brings a possibility that the phase diagram Figure 2.2(b) might not be applicable for YSZ thin films. More crystallinity studies are needed to investigate this topic.

AFM results for both as-deposited and annealed ALD YSZ thin films with 15s t_1 are shown in Figure 5.10. For comparison, the height scale for both samples was fixed. In Figure 5.10 (a), the surface of as-deposited sample is very smooth with a RMS roughness of 0.289 nm, which has been commonly observed since

ALD produces uniform and homogeneous thin films resulting from its self-limiting nature. In the AFM analysis of Shim [12] and Kim [21], at 250℃ deposition temperature with water as the oxidant, as-deposited ALD YSZ thin films showed much higher RMS roughness of 1.5 nm [12] and 1.79 nm [21], respectively. In another investigation of Paek [26], 0.5 nm RMS roughness of as-deposited ALD YSZ was obtained with O_2 as the oxidant at 250℃ deposition temperature. The variations of oxidant and deposition temperature are possibly responsible for the roughness difference. According to Putkonen [6], the film thickness is also a factor affecting the roughness of ALD YSZ thin films, which has been investigated in a later section of this chapter.

For bulk materials generally, roughness decreases after annealing. However, for thin film materials, the effect of annealing on surface roughness is complex, varying on a case by case basis. In this study, the surface of ALD YSZ thin film was much rougher after annealing, with a RMS roughness of 2.2 nm, as shown in Figure 5.10 (b). Raoufi [55] observed the same effect of annealing on indium tin oxide thin film roughness and suspected that this behavior is due to the native grains aggregation into larger clusters upon annealing.

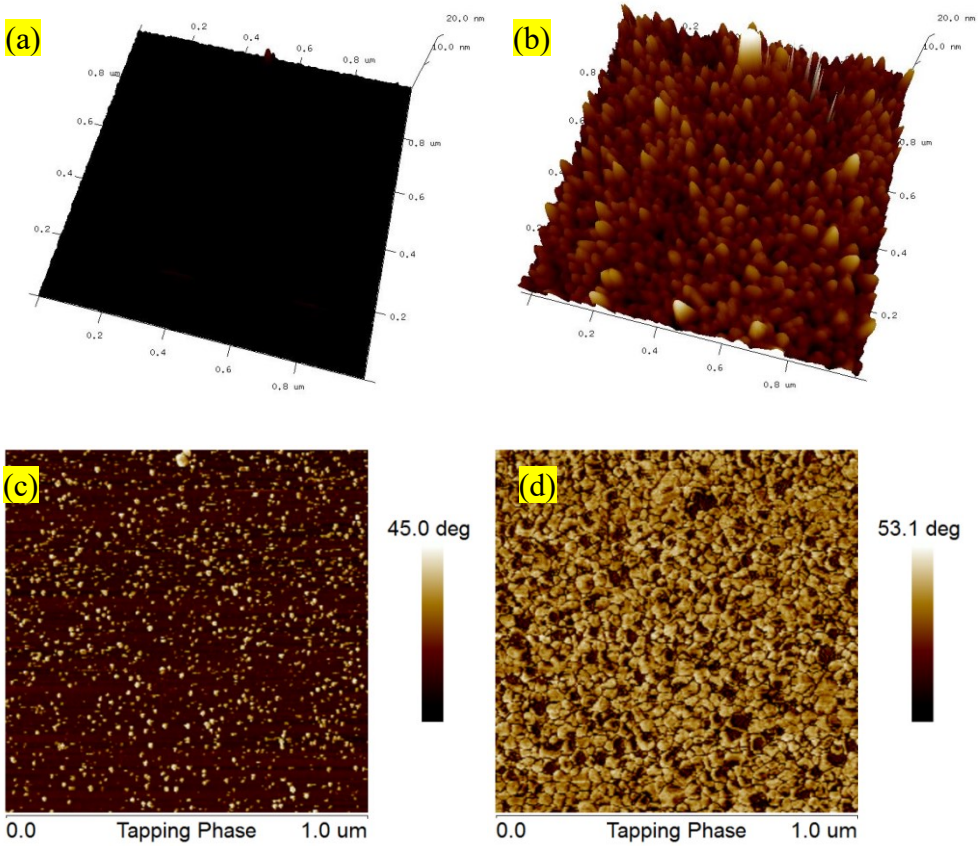

Figure 5.10. AFM topographical 3D images and tapping phase patterns of the as-deposited sample (a), (c), and of the annealed sample (b), (d).

No clear grain boundaries can be observed in the as-deposited sample in this study, as shown in Figure 5.10 (c). After annealing clear grain boundaries were observed. As mentioned in section 3.4.5, the average grain size was measured by the classical line intersection method, obtaining 45.9±1.8 nm. However, in the AFM analysis of Shim [12] and Kim [21], as-deposited ALD YSZ thin films showed nanometer sized grains with well-defined grain boundaries, and high

temperature annealing did not change the size and shape of grains of ALD YSZ thin films significantly. The possible reason is the thickness difference of ALD YSZ films. The thickness of ALD YSZ films in the work of Shim [12] varied from 60 nm to 140 nm, while in this study it is only 14.7 nm. In the research of Ji [27], the average grain sizes for PEALD-YSZ with the thicknesses of 35 nm, 70 nm, 140 nm, and 210 nm are 20 nm, 34 nm, 41 nm, 52 nm, respectively. If the dependence of grain size on thickness in this study followed the trend, the grain size of 14.7 nm thick YSZ thin film would be too small (<10 nm) to be perceived from the AFM images. Therefore, the thickness possibly plays a significant role in the microstructural change. Its effect will be discussed in the later section. Besides, the difference in recipes is probably responsible for this variation to some extent.

5.3.5 Effect of YSZ thickness & annealing on conductivity

It is commonly accepted that according to the definition of conductance, a change in thickness of electrolyte materials only affects conductance of electrolyte materials, not their conductivities. However, it has been found by some researchers [17, 38, 56] that high conductivities were achieved by reducing the thickness of YSZ thin films. This effect is still controversial in literature. Gilardi [56] found that the conductivity was improved by 26.4% when decreasing the thickness from 300 nm to 70 nm. Huang [17] fabricated YSZ thin films with

thickness from 8 nm to 55 nm and found that thinner YSZ exhibited higher ionic conductivities. A substantial increase was observed when thickness was lower than 11 nm. Kosachi [38] observed a similar enhancing effect of lowering YSZ thin film thickness on conductivity, with a broader thickness range from 15 nm to 2 μm. The unique finding of Kosachi [38] was that the enhancing effect only happened when thin YSZ films thickness was lower 60 nm. Both Huang [17] and Kosachi [38] attributed the exceptionally high ionic conductivity to the fact that surface/interface conductivity becomes more dominant upon decreasing YSZ thin film thickness.

In this study, samples of 30 cycles, 60 cycles, 100cycles, 200 cycles, and 300 cycles using the recipe with t_l=15s in Section 5.3A were fabricated to study the effect of thickness. Table 5.3 shows the thickness of different samples obtained from ellipsometric measurements, and Figure 5.11 is the electrical test results of both as-deposited and annealed samples. In Gilardi's work [56], YSZ thin films with thickness lower than 70 nm were not considered, otherwise the conductance could become comparable to that of the bare substrate. Therefore, the conductivity should be very low in our study since Si(100) is insulative to oxygen ionic conduction. However, all samples showed good conduction properties. It can be explained by Elam [57]'s view that the challenge of YSZ thin films (< 10 nm) is to produce a homogeneous and leak free layer, which is an accomplishable feature of ALD thin films.

Table 5.3. Samples thickness with different numbers of cycles.

30 cycles	60 cycles	100 cycles	200 cycles	300 cycles
4.5 nm	8.5 nm	14.7 nm	28.4 nm	42.7 nm

From Figure 5.11 it can be seen that there is a dependence of ionic conductivity on thickness. At all measurement temperatures, thinner YSZ thin film samples performed better than thicker ones. Since the lattice mismatch between YSZ and Si(100) substrate is very small as mentioned above, it is speculated that microstructure differences of samples resulting from the different number of ALD cycles is responsible. It is noteworthy that the conductivities decreased after annealing in all cases. Table 5.4 gives the activation energies of oxygen ionic conductance obtained from the Arrhenius plots. For as-deposited samples, when number of cycles is lower than 100, the activation energies were from 0.96 eV to 0.99 eV; while it became 1.03 eV for samples with 200 and 300 cycles. Annealing increased the activation energies for all samples. A detailed discussion will be conducted later in AFM and XRD results.

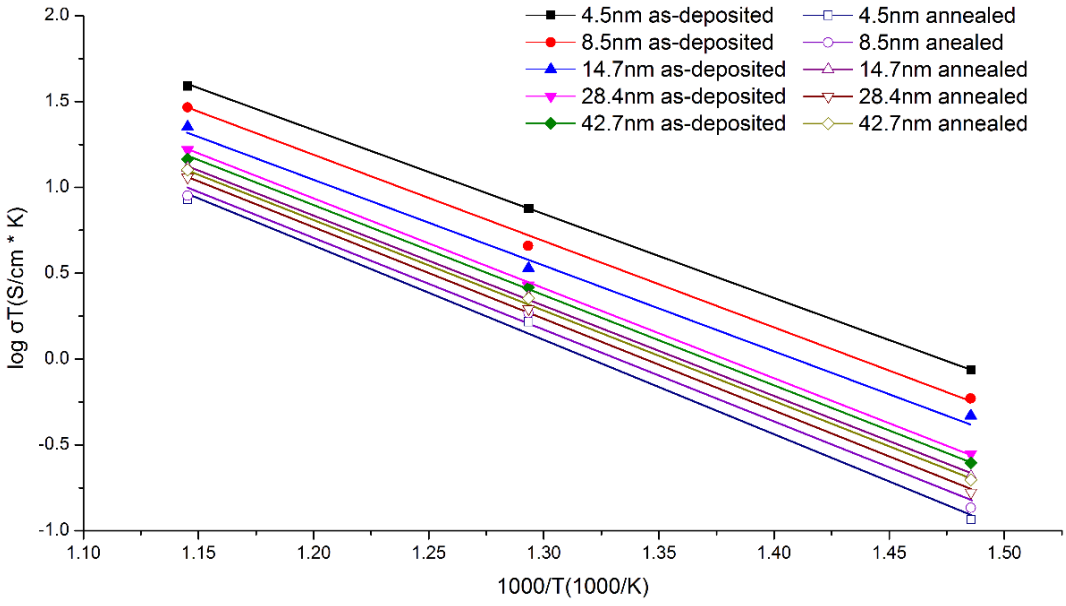

Figure 5.11. Arrhenius plot of the measured ionic conductivity of as-deposited and annealed samples with different numbers of cycle at 400℃, 500℃, and 600℃.

Table 5.4. Summary of activation energies of oxygen ionic conductance.

# of cycles		**30**	**60**	**100**	**200**	**300**
Actvation energy	As-dep.	0.96eV	0.99eV	0.98eV	1.03eV	1.03eV
	Annealed	1.09eV	1.07eV	1.05eV	1.07eV	1.05eV

XRD and AFM investigations were performed in order to study the effect of thickness on crystallinity and microstructure. Figure 5.12 shows the XRD results for both as-deposited (a) and annealed (b) samples.

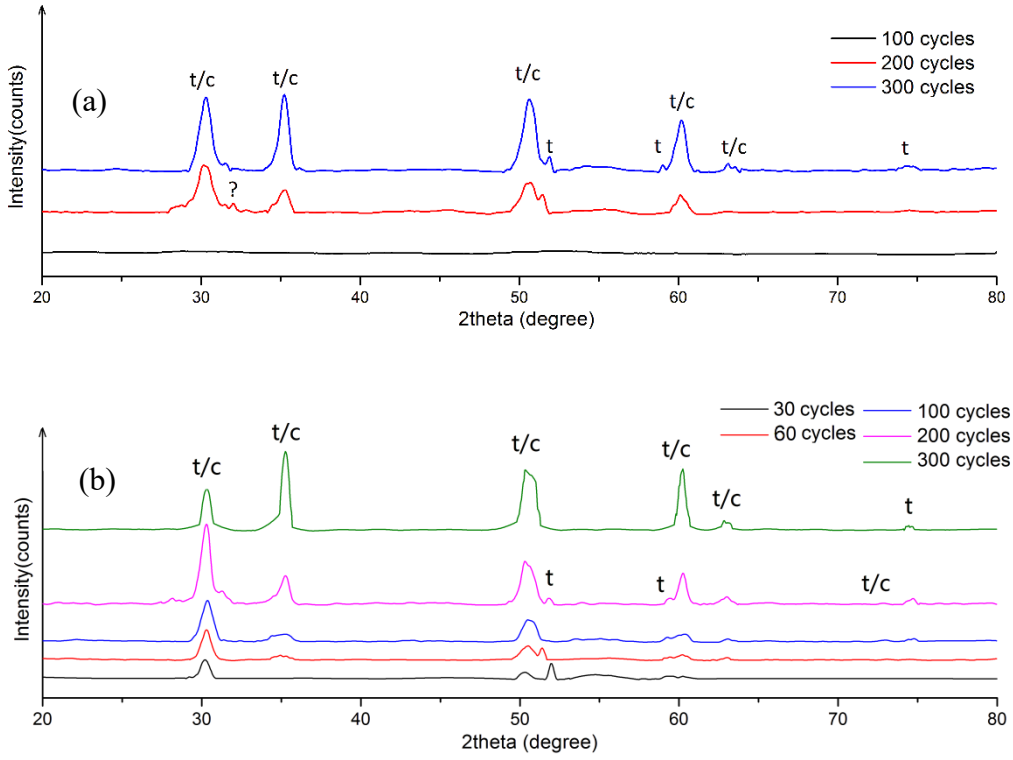

Figure 5.12 XRD patterns of ALD YSZ thin films as-deposited(a) and annealed(b) samples.

It can be observed that for as-deposited samples, no peaks were observed in the results when thickness was lower than 28.4 nm. After annealing, these samples exhibited peaks, indicating higher degree of crystallinity. Peaks at ~63° and ~75° appeared only when the thickness reached 42.7 nm for as-deposited samples. The 42.7 nm sample showed less peaks after annealing, in which the major peaks match the cubic phase pattern, probably because more cubic phase are generated after annealing. On the contrary, for other samples more peaks appeared after annealing. Furthermore, it is noteworthy that there was a weak

peak at ~32° for as-deposited 200-cycle sample. The intensity was weak and comparable to the noise's intensity in the raw data. It could either be the (111) peak from monoclinic phase or merely a noise.

Table 5.5 shows the grain size and roughness values of both as-deposited and annealed samples obtained from AFM tests. As illustrated in section 5.3D, both grain size and roughness of all samples became higher after annealing. It is noteworthy that roughness increased with increasing the number of ALD cycles, which is accordant with the observation in Putkonen's work [58, 59]. An explanation was made by Putkonen's work [58, 59] that higher crystallinity was obtained with a longer deposition cycles, leading to a rougher surface.

Besides, it can be seen that larger average grain size was achieved with increasing the thickness for both as-deposited and annealed samples, resulting from grain growth in a longer deposition time. In an investigation of Ji [27], average grain sizes of 20 nm, 34 nm, 41 nm, 52 nm PEALD-YSZ as-deposited thin films were attained for samples with the thicknesses of 35 nm, 70 nm, 140 nm, and 210 nm, respectively. Also, it is well known that a noticeable increase in grain size can be observed after annealing due to the grain growth.

Table 5.5. Summary of grain size and roughness for as-deposited and annealed samples.

# of cycles		30	60	100	200	300
Grain size (nm)	As-dep.	-	-	-	24.8±0.6	35.0±0.7
	Annealed	66.5±2.8	54.8±1.6	45.9±1.8	50.7±1.7	48.4±2.2
RMS roughness (nm)	As-dep.	0.25	0.47	0.51	0.78	1.86
	Annealed	3.77	2.40	2.07	2.32	2.53

According to the results from XRD and AFM tests, a plausible explanation of conductivity dependence on thickness can be made as follows. Higher thickness was determined by larger number of ALD cycles, which was associated with longer processing time. According to the theory of annealing, increase in either annealing temperature or time will produce coarser grains. Although the processing temperature of ALD was as low as 150℃, larger number of ALD cycles still requires a considerably longer time to complete the process due to the low growth rate of ALD technique. As a result, the average grain size of samples increased with higher thickness, as shown in Table 5.5. Consequently, conductivity improvement from true size effect [35] was weakened according to the description in section 5.3B, leading to lower levels of conductivity.

The effect of annealing is similar, coarsening grains in YSZ thin film samples. Therefore, poorer conductivities and higher activation energy barriers are obtained. It can be seen from Table 5.5 that, the grain coarsening effect of

annealing on as-deposited samples with higher thickness and larger grain size is less severe. For example, for 4.5 nm thick sample, the grain size became 66.5 nm from a size lower than 10 nm; while for 42.7 nm thick one, the grain size only increased from 35 nm to 48.4 nm. It is supported by the finding of Shim [12] that high temperature annealing hardly changed the grain size of YSZ thin films. Annealing is able to increase crystallinity degree and homogenizing the distribution of yttrium oxide in YSZ. However, during electrical test our as-deposited samples are crystalline and homogeneous already. Therefore, annealing is harmful to conductivity of YSZ thin films in this study.

5.4 Conclusions

In summary, YSZ thin films with low yttrium oxide concentrations were fabricated on Si(100) substrates by ALD. Using this ALD recipe, yttrium oxide was homogeneously distributed in YSZ thin films. No annealing is needed to homogenize the distribution of yttrium oxide. The GPC obtained from ellipsometric measurement was from 1.15 Å/cycle to 1.35 Å/cycle, close to the values in literature. Most of the samples exhibited higher ionic conductivity than that of bulk 8YSZ sample. Activation energies were from 0.98 eV to 1.01 eV, lower than most ALD samples in references. The one showing highest conductivity was 1.6YSZ rather than the well-known 8YSZ, with a conductivity

of 0.2 S/cm at 600°C. The strong true size effect with wide SCLs is speculated to be responsible for this change. All samples showed high refractive indices, confirming that these thin films have excellent quality. XRD results proved that YSZ thin films are crystalline although no noticeable peaks were found in thin as-deposited samples. However, it might be misleading to claim they are cubic phase or tetragonal phase because of the high similarity of the XRD patterns of these two. AFM results showed the 1.6YSZ thin film had a very smooth surface with a RMS roughness of 0.29 nm. Furthermore, the effects of thickness and annealing on conductivity were investigated. It was found that the increase in thickness requires more number of ALD cycles, leading to a larger average grain size. Annealing coarsens grains in a very unique way that the larger grain size of the as-deposited sample is, the smaller increase in grain size of annealed sample is. Since both increasing thickness and annealing yield larger grain size, the conductivity became lower due to weaker true size effect. Therefore, with this ALD method annealing should be avoided if possible to maintain the high conductivity resulting from the true size effect.

5.5 References

[1] Stambouli, A. B., & Traversa, E. (2002). Solid oxide fuel cells (SOFCs): a review of an environmentally clean and efficient source of energy. Renewable and sustainable energy reviews, 6(5), 433-455.

[2] Hui, S. R., Roller, J., Yick, S., Zhang, X., Deces-Petit, C., Xie, Y., ... & Ghosh, D. (2007). A brief review of the ionic conductivity enhancement for selected oxide electrolytes. Journal of Power Sources, 172(2), 493-502.

[3] Wu, F., Wu, J. N., Banerjee, S., Blank, O., & Banerjee, P. (2013). Frontiers in applied atomic layer deposition (ALD) research. In Materials Science Forum (Vol. 736, pp. 147-182). Trans Tech Publications.

[4] Larminie, J., Dicks, A., & McDonald, M. S. (2003). Fuel cell systems explained (Vol. 2). Chichester, UK: J. Wiley.

[5] Foroughi-Abari, A., & Cadien, K. (2012). Atomic layer deposition for nanotechnology. In Nanofabrication (pp. 143-161). Springer Vienna.

[6] Putkonen, M., Sajavaara, T., Niinistö, J., Johansson, L. S., & Niinistö, L. (2002). Deposition of yttria-stabilized zirconia thin films by atomic layer epitaxy from β-diketonate and organometallic precursors. Journal of Materials Chemistry, 12(3), 442-448.

[7] Bernay, C., Ringuedé, A., Colomban, P., Lincot, D., & Cassir, M. (2003). Yttria-doped zirconia thin films deposited by atomic layer deposition ALD: a structural, morphological and electrical characterisation. Journal of Physics and Chemistry of Solids, 64(9), 1761-1770.

[8] Bae, K., Son, K. S., Kim, J. W., Park, S. W., An, J., Prinz, F. B., & Shim, J. H. (2014). Proton incorporation in yttria-stabilized zirconia during atomic layer deposition. International Journal of Hydrogen Energy, 39(6), 2621-2627.

[9] Sik Son, K., Bae, K., Woo Kim, J., Suk Ha, J., & Hyung Shim, J. (2013). Ion conduction in nanoscale yttria-stabilized zirconia fabricated by atomic layer deposition with various doping rates. Journal of Vacuum Science & Technology A: Vacuum, Surfaces, and Films, 31(1), 01A107.

[10] Son, K. S., Bae, M. Y., Bae, K., Ha, J. S., & Shim, J. H. (2012). Incorporation of hydroxyl ions and protons in oxide ion vacancies in nanoscale yttria stabilized zirconia during atomic layer deposition. ECS Transactions, 45(1), 155-160.

[11] Chao, C. C., Hsu, C. M., Cui, Y., & Prinz, F. B. (2011). Improved solid oxide fuel cell performance with nanostructured electrolytes. ACS nano, 5(7), 5692-5696.

[12] Shim, J. H., Chao, C. C., Huang, H., & Prinz, F. B. (2007). Atomic layer deposition of yttria-stabilized zirconia for solid oxide fuel cells. Chemistry of Materials, 19(15), 3850-3854.

[13] Park, J. S., Kim, Y. B., Shim, J. H., Kang, S., Gür, T. M., & Prinz, F. B. (2010). Evidence of proton transport in atomic layer deposited yttria-stabilized zirconia films. Chemistry of Materials, 22(18), 5366-5370.

[14] Chao, C. C., Kim, Y. B., & Prinz, F. B. (2009). Surface modification of yttria-stabilized zirconia electrolyte by atomic layer deposition. Nano letters, 9(10), 3626-3628.

[16] Chao, C. C., Park, J. S., Tian, X., Shim, J. H., Gür, T. M., & Prinz, F. B. (2013). Enhanced oxygen exchange on surface-engineered yttria-stabilized zirconia. ACS nano, 7(3), 2186-2191.

[17] Huang, H., Shim, J. H., Chao, C. C., Pornprasertsuk, R., Sugawara, M., Gür, T. M., & Prinz, F. B. (2009). Characteristics of oxygen reduction on nanocrystalline YSZ. Journal of The Electrochemical Society, 156(3), B392-B396.

[18] Hong, S., Bae, J., Koo, B., & Kim, Y. B. (2014). High-performance ultra-thin film solid oxide fuel cell using anodized-aluminum-oxide supporting structure. Electrochemistry Communications, 47, 1-4.

[19] Jang, D. Y., Kim, H., Bae, K., Schlupp, M. V., Prestat, M., & Shim, J. H. (2013). Performance of Atomic-Layer-Deposited Yttria-Stabilized Zirconia Near Room Temperature. ECS Transactions, 57(1), 1103-1106.

[20] Jang, D. Y., Kim, H. K., Kim, J. W., Bae, K., Schlupp, M. V., Park, S. W., ... & Shim, J. H. (2015). Low-temperature performance of yttria-stabilized zirconia prepared by atomic layer deposition. Journal of Power Sources, 274, 611-618.

[21] Kim, H. K., Jang, D. Y., Kim, J. W., Bae, K., & Shim, J. H. (2015). Ionic properties of ultrathin yttria-stabilized zirconia thin films fabricated by atomic layer deposition with water, oxygen, and ozone. Thin Solid Films, 589, 441-445.

[22] Tanveer, W. H., Ji, S., Yu, W., & Cha, S. W. (2015). Characterization of atomic layer deposited and sputtered yttria-stabilized-zirconia thin films for low-temperature solid oxide fuel cells. International Journal of Precision Engineering and Manufacturing, 16(10), 2229-2234.

[23] Ha, S., Su, P. C., & Cha, S. W. (2013). Combinatorial deposition of a dense nano-thin film YSZ electrolyte for low temperature solid oxide fuel cells. Journal of Materials Chemistry A, 1(34), 9645-9649.

[24] Jee, Y., Cho, G. Y., An, J., Kim, H. R., Son, J. W., Lee, J. H., ... & Cha, S. W. (2014). High performance Bi-layered electrolytes via atomic layer deposition for solid oxide fuel cells. Journal of Power Sources, 253, 114-122.

[25] Yu, W., Ji, S., Cho, G. Y., Noh, S., Tanveer, W. H., An, J., & Cha, S. W. (2015). Atomic layer deposition of ultrathin blocking layer for low-temperature solid oxide fuel cell on nanoporous substrate. Journal of Vacuum Science & Technology A: Vacuum, Surfaces, and Films, 33(1), 01A145.

[26] Paek, J. Y., Chang, I., Park, J. H., Ji, S., & Cha, S. W. (2014). A study on properties of yttrium-stabilized zirconia thin films fabricated by different deposition techniques. Renewable Energy, 65, 202-206.

[27] Ji, S., Cho, G. Y., Yu, W., Su, P. C., Lee, M. H., & Cha, S. W. (2015). Plasma-enhanced atomic layer deposition of nanoscale yttria-stabilized

zirconia electrolyte for solid oxide fuel cells with porous substrate. ACS applied materials & interfaces, 7(5), 2998-3002.

[28] Cha, S. W., Cho, G. Y., Lee, Y., Park, T., Kim, Y., & Lee, J. M. (2016). Effects of carbon contaminations on Y 2 O 3-stabilized ZrO 2 thin film electrolyte prepared by atomic layer deposition for thin film solid oxide fuel cells. CIRP Annals-Manufacturing Technology, 65(1), 515-518.

[29] Park, T., Cho, G. Y., Lee, Y. H., Tanveer, W. H., Yu, W., Lee, Y., ... & Cha, S. W. (2016). Effect of anode morphology on the performance of thin film solid oxide fuel cell with PEALD YSZ electrolyte. International Journal of Hydrogen Energy, 41(22), 9638-9643.

[30] Lecordier, L. (2015). Atomic Layer Deposition and in-Situ Characterization of Yttrium Oxide and Yttria-Stabilized Zirconia. ECS Transactions, 69(7), 109-116.

[31] Goodenough, J. B. (2003). Oxide-ion electrolytes. Annual review of materials research, 33(1), 91-128.

[32] Ivers-Tiffée, E., Weber, A., & Herbstritt, D. (2001). Materials and technologies for SOFC-components. Journal of the European Ceramic Society, 21(10), 1805-1811.

[33] Ramamoorthy, R., Sundararaman, D., & Ramasamy, S. (1999). Ionic conductivity studies of ultrafine-grained yttria stabilized zirconia polymorphs. Solid State Ionics, 123(1), 271-278.

[34] Peters, Christoph. Grain-size effects in nanoscaled electrolyte and cathode thin films for solid oxide fuel cells (SOFC). Vol. 15. KIT Scientific Publishing, 2009.

[35] Maier, J. (2003). Nano-ionics: Trivial and non-trivial size effects on ion conduction in solids.

[36] Durá, O. J., de la Torre, M. L., Vázquez, L., Chaboy, J., Boada, R., Rivera-Calzada, A., ... & Leon, C. (2010). Ionic conductivity of nanocrystalline yttria-stabilized zirconia: Grain boundary and size effects. Physical review B, 81(18), 184301..

[37] Fabbri, E., Pergolesi, D., & Traversa, E. (2010). Ionic conductivity in oxide heterostructures: the role of interfaces. Science and Technology of Advanced Materials, 11(5), 054503.

[38] Kosacki, I., Rouleau, C. M., Becher, P. F., Bentley, J., & Lowndes, D. H. (2005). Nanoscale effects on the ionic conductivity in highly textured YSZ thin films. Solid State Ionics, 176(13), 1319-1326.

[39] Schichtel, N., Korte, C., Hesse, D., & Janek, J. (2009). Elastic strain at interfaces and its influence on ionic conductivity in nanoscaled solid electrolyte thin films—theoretical considerations and experimental studies. Physical Chemistry Chemical Physics, 11(17), 3043-3048.

[40] Korte, C., Schichtel, N., Hesse, D., & Janek, J. (2009). Influence of interface structure on mass transport in phase boundaries between different ionic materials. Monatshefte für Chemie-Chemical Monthly, 140(9), 1069-1080.

[41] Peters, A., Korte, C., Hesse, D., Zakharov, N., & Janek, J. (2007). Ionic conductivity and activation energy for oxygen ion transport in superlattices—the multilayer system CSZ (ZrO 2+ CaO)/Al 2 O 3. Solid State Ionics, 178(1), 67-76.

[42] Fukumoto, H., Imura, T., & Osaka, Y. (1989). Heteroepitaxial growth of Y2O3 films on silicon. Applied Physics Letters, 55(4), 360-361.

[43] Hirai, T., Teramoto, K., Koike, H., Nagashima, K., & Tarui, Y. (1997). Initial stage and growth process of ceria, yttria-stabilized-zirconia and ceria-zirconia mixture thin films on Si (100) surfaces. Japanese journal of applied physics, 36(8R), 5253.

[44] Bardal, A., Eibl, O., Matthee, T., Friedl, G., & Wecker, J. (1993). High-resolution electron microscopy of epitaxial YBCO/Y 2 O 3/YSZ on Si (001). Journal of materials research, 8(09), 2112-2127.

[45] Steele, B. C. H. (1995). Interfacial reactions associated with ceramic ion transport membranes. Solid State Ionics, 75, 157-165.

[46] Shim, J. H., Kang, S., Cha, S. W., Lee, W., Kim, Y. B., Park, J. S., ... & An, J. (2013). Atomic layer deposition of thin-film ceramic electrolytes for high-

performance fuel cells. Journal of Materials Chemistry A, 1(41), 12695-12705.

[47] Zhang, C., Li, C. J., Zhang, G., Ning, X. J., Li, C. X., Liao, H., & Coddet, C. (2007). Ionic conductivity and its temperature dependence of atmospheric plasma-sprayed yttria stabilized zirconia electrolyte. Materials Science and Engineering: B, 137(1), 24-30.

[48] Wood, D. L., & Nassau, K. (1982). Refractive index of cubic zirconia stabilized with yttria. Applied Optics, 21(16), 2978-2981.

[49] Xiao, Q. L., Xu, C., Shao, S. Y., Shao, J. D., & Fan, Z. X. (2008). Y 2 O 3 stabilized ZrO 2 thin films deposited by electron-beam evaporation: Optical properties, structure and residual stresses. Vacuum, 83(2), 366-371.

[50] Heiroth, S., Ghisleni, R., Lippert, T., Michler, J., & Wokaun, A. (2011). Optical and mechanical properties of amorphous and crystalline yttria-stabilized zirconia thin films prepared by pulsed laser deposition. Acta Materialia, 59(6), 2330-2340.

[51] Wood, D. L., Nassau, K., & Kometani, T. Y. (1990). Refractive index of Y2O3 stabilized cubic zirconia: variation with composition and wavelength. Applied optics, 29(16), 2485-2488.

[52] Lin, S. S., & Huang, J. L. (2004). Effect of thickness on the structural and optical properties of ZnO films by rf magnetron sputtering. Surface and Coatings Technology, 185(2), 222-227.

[53] Miikkulainen, V., Leskelä, M., Ritala, M., & Puurunen, R. L. (2013). Crystallinity of inorganic films grown by atomic layer deposition: Overview and general trends. Journal of Applied Physics, 113(2), 2.

[54] Kukli, K., Forsgren, K., Aarik, J., Uustare, T., Aidla, A., Niskanen, A., ... & Hårsta, A. (2001). Atomic layer deposition of zirconium oxide from zirconium tetraiodide, water and hydrogen peroxide. Journal of Crystal Growth, 231(1), 262-272.

[55] Raoufi, D., Kiasatpour, A., Fallah, H. R., & Rozatian, A. S. H. (2007). Surface characterization and microstructure of ITO thin films at different annealing temperatures. Applied Surface Science, 253(23), 9085-9090.

[56] Gilardi, E. (2016). Interface effects in Y2Zr2O7 thin films.

[57] Elam, J. W., Dasgupta, N. P., & Prinz, F. B. (2011). ALD for clean energy conversion, utilization, and storage. Mrs Bulletin, 36(11), 899-906.

[58] Putkonen, M., & Niinistö, L. (2001). Zirconia thin films by atomic layer epitaxy. A comparative study on the use of novel precursors with ozone. Journal of Materials Chemistry, 11(12), 3141-3147.

[59] Putkonen, M., Sajavaara, T., Johansson, L. S., & Niinistö, L. (2001). Low‐Temperature ALE Deposition of Y2O3 Thin Films from β‐Diketonate Precursors. Chemical Vapor Deposition, 7(1), 44-50.

Chapter 6

Effect of PEALD recipe on the performance of YSZ thin films

6.1 Introduction

Thin film YSZ has attracted much attention as an electrolyte material for IT-SOFCs [1-5], and ALD has been considered a promising technique to fabricate conformal and pinhole-free YSZ thin films [6]. In chapter 5, PEALD of YSZ thin films were shown to have good film quality and outstanding electrical properties.

In the literature papers [7-32] on the ALD of YSZ thin films, the vast majority of them [8-31] used AOBO (YOZO or ZOYO) type ALD recipes, in which an ALD super-cycle consisting of both Y_2O_3 and ZrO_2 ALD cycles was used. The concentrations of yttrium oxide in YSZ were manipulated by the ratio of the number of yttrium oxide ALD cycles to zirconium oxide ALD cycles in one ALD super-cycle. Putkonen [7], Son [8], and Chao [9,10] have demonstrated detailed analytical relationships between this ratio and yttrium oxide concentrations. The ampoule temperature was set as high as 190℃ in references [8, 9, 13-17, 25-27], in order to provide enough precursor molecules for ALD reactions. In chapter 5, an ABO type PEALD recipe was utilized to fabricate YSZ thin films, taking advantage of the low vapor pressure of the yttrium precursor $Y(MeCp)_3$, with

outstanding electrical properties. Benefits include no gas phase reactions at high temperatures compromising film quality and no need of post-annealing to eliminate the heterogeneous distribution of yttrium oxide in YSZ thin films.

In this chapter, four different ALD recipes (YOZO, ZOYO, YZO, ZYO) with various precursor pulse sequences were conducted for YSZ thin films fabrication. The effect of the recipe variation on the ALD YSZ thin film properties was investigated.

6.2 Experimental

The precursor pulse sequence and pulse widths utilized in this study are shown below in Figure 6.1. The ZOYO and YOZO type recipes are commonly used in literature, in which one ALD super-cycle consists of one ZrO_2 ALD cycle and one Y_2O_3 ALD cycle. The only difference between YOZO and ZOYO is the first ALD cycle, starting with ZrO_2 ALD cycle in the case of ZOYO and with Y_2O_3 ALD cycle in the case of YOZO. The ZYO and YZO recipes were developed in our group, in which both zirconium and yttrium precursor were pulsed into the reaction chamber one following the other (zirconium/yttrium precursor pulse began first in ZYO/YZO recipe) before introducing oxygen plasma in one ALD cycle. In this method, the yttrium oxide is homogeneously distributed in every molecular layer of YSZ thin films according to the ALD reaction mechanism.

Two hundred ALD cycles depositions were performed with each recipe, and after the deposition measurements were conducted to characterize the ALD YSZ thin films. Electrical evaluation of a commercial bulk 8YSZ sample with a thickness in the range from 0.25mm to 0.3mm from FCM (Fuelcellmaterials.com) was conducted for comparison.

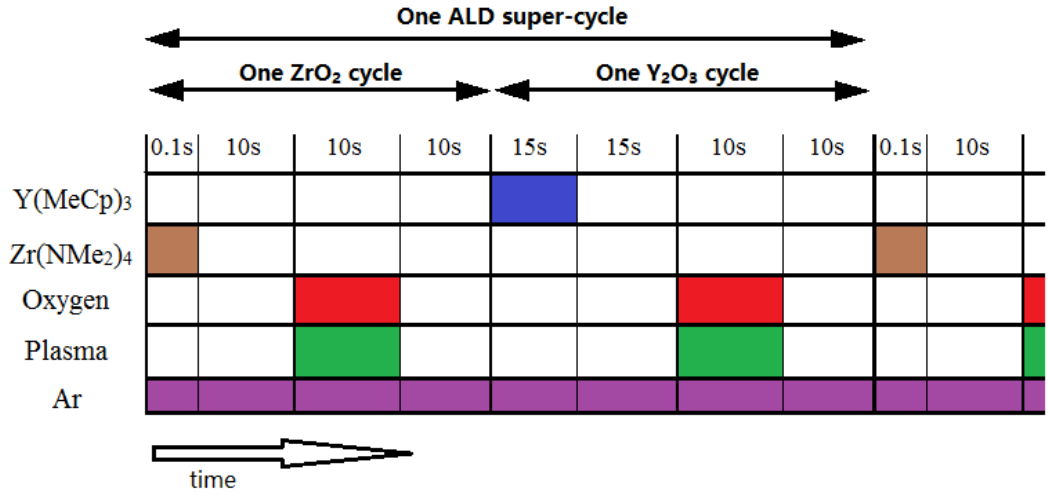

(a) ZOYO recipe

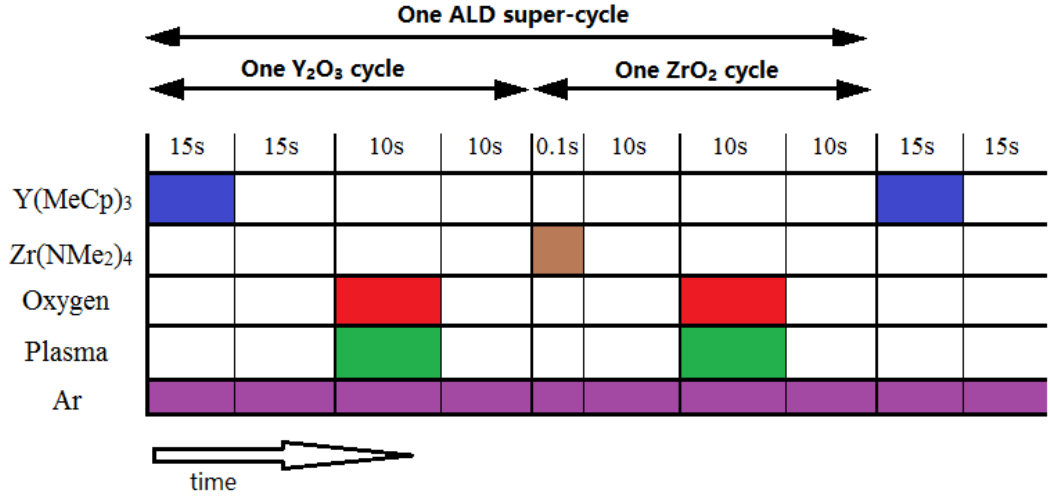

(b) YOZO recipe

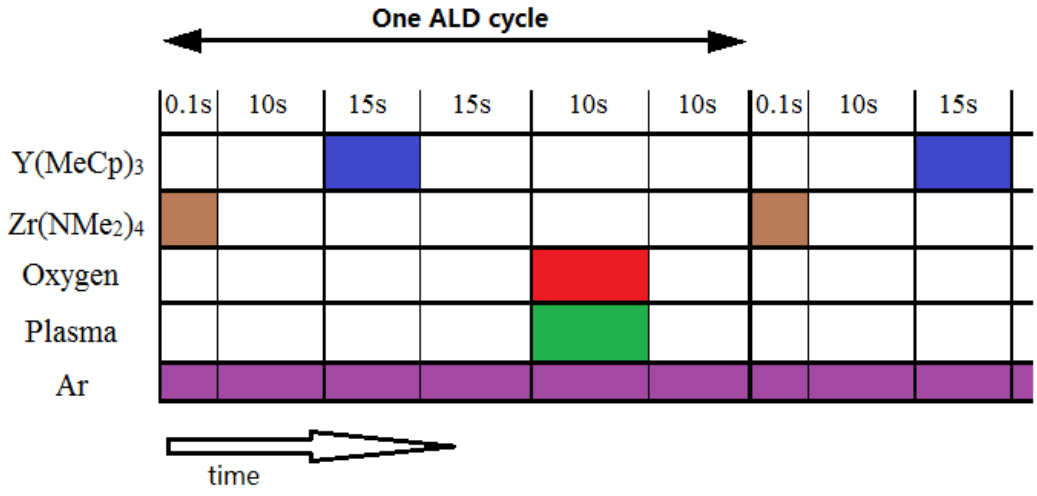

(c) ZYO recipe

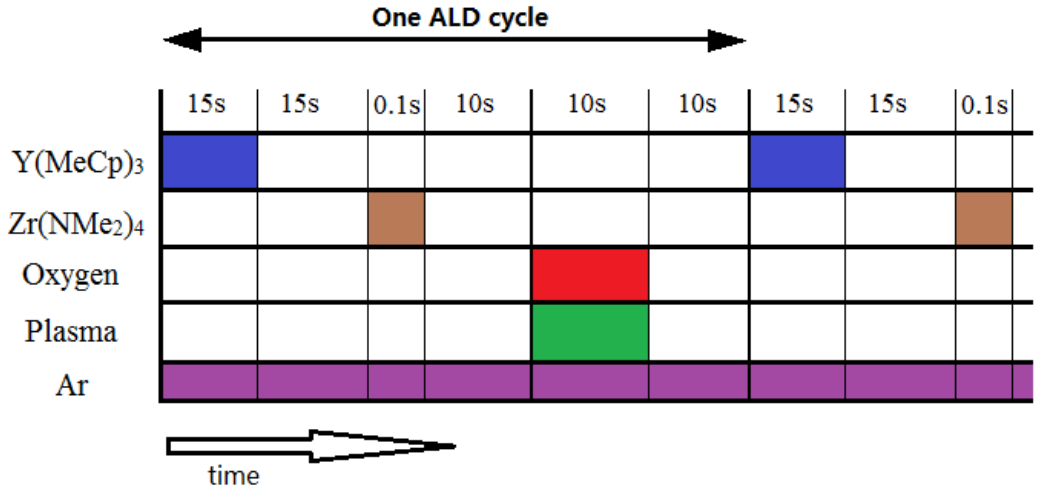

(d) YZO recipe

Figure 6.1. Details of the four ALD recipes used.

A J. A. Woollam M2000DI dynamic in-situ spectroscopic ellipsometer was used to optically characterize the thickness of ALD YSZ thin films and their refractive index (n(λ)) functions were approximated by Cauchy's polynomials, as

illustrated in chapter 3. Annealing was conducted post deposition on some of the samples at 1000℃ for 2 hours to investigate the stability of the thin films.

6.3 Results and Discussion

6.3.1 ALD growth and optical properties

The GPC for each ALD recipe is shown in Figure 6.2. The pure zirconium oxide deposition GPC was superimposed on the plot as a reference. ZYO shows the highest GPC, slightly higher than that of pure zirconium oxide. This can be explained by the mechanism of ALD reactions [33]. Before introducing the $Y(MeCp)_3$ pulse, the size of the $Zr(NMe_2)_4$ chemisorbed molecules decreased because of ligand exchange, dissociation or association in the chemical adsorption process, exposing some reactions that were blocked by steric hindrance. This permits the adsorption of $Y(MeCp)_3$ molecules and additional yttrium oxide growth occurred in the recipe ZYO during each ALD cycle, yielding a higher GPC than that of pure zirconium oxide. Recipe YZO had a lower GPC than that of pure zirconium oxide due to the molecular size difference of $Y(MeCp)_3$ and $Zr(NMe_2)_4$ (detailed information can be found in the previous chapter). It is noteworthy that YOZO and ZOYO recipes exhibited similar GPC which is slightly lower than pure zirconium oxide GPC. A plausible explanation for this is that the growth mechanism of both zirconium oxide and yttrium oxide

is substrate-inhibited growth [33], in which materials favor growth on themselves. It is in agreement with the findings of Shim's work [16] that the GPC of YSZ is lower than that of either yttrium oxide or zirconium oxide.

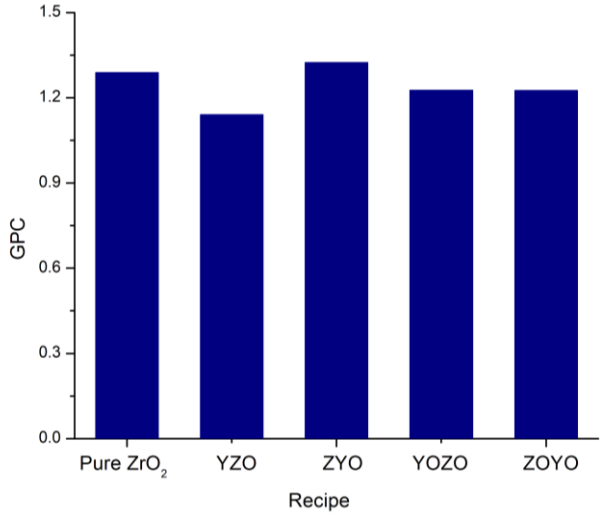

Figure 6.2. GPCs obtained with the four recipes being used.

Refractive indices of ALD thin films at 550 nm were obtained from ellipsometric data and is summarized in Table 6.1. The YZO sample showed the lowest refractive index, very close to that of pure zirconium oxide while the highest refractive index was obtained for recipe YOZO. However, refractive indices of all samples are relatively high and very close to those of bulk YSZ (2.2), and the variation among them is not significant. Electron beam evaporated YSZ thin films in Xiao's work [34] only exhibited refractive indices (550nm) of 1.86 to 1.94. This indicates that ALD is a suitable fabrication technique producing dense SOFC electrolyte thin films.

Table 6.1. Summary of refractive indices of thin film samples at 550 nm.

ALD Recipe	Pure ZrO_2	YZO	ZYO	YOZO	ZOYO
Refractive index	2.139	2.134	2.153	2.165	2.153

6.3.2 Compositional analysis and ionic conductivity

The yttrium oxide concentrations in each YSZ thin film sample are shown in Figure 6.3. Sample YZO has a higher yttrium oxide concentration than that of ZYO. From Figure 6.1 we know that the only difference between ZYO and YZO is the sequence of $Y(MeCp)_3$ and $Zr(NMe_2)_4$ pulses during the ALD cycle. This variation of yttrium oxide concentration in ZYO and YZO can be explained by considering that the first pulse of $Zr(NMe_2)_4$ in the ZYO recipe occupied more active sites on the substrate surface, leaving a lower number of active sites for the following $Y(MeCp)_3$ pulse. On the contrary, $Y(MeCp)_3$ adsorption consumed a number of active sites in YZO recipe. As a result, ZYO thin films were lightly doped. The concentrations of yttrium oxide of sample YOZO and ZOYO are close, higher than that of YZO and ZYO. Considering the discussions (in section 6.3A) that both zirconium oxide and yttrium oxide were substrate-inhibited growth in these two recipes, we can conclude that the growth of zirconium oxide was more inhibited than that of yttrium oxide.

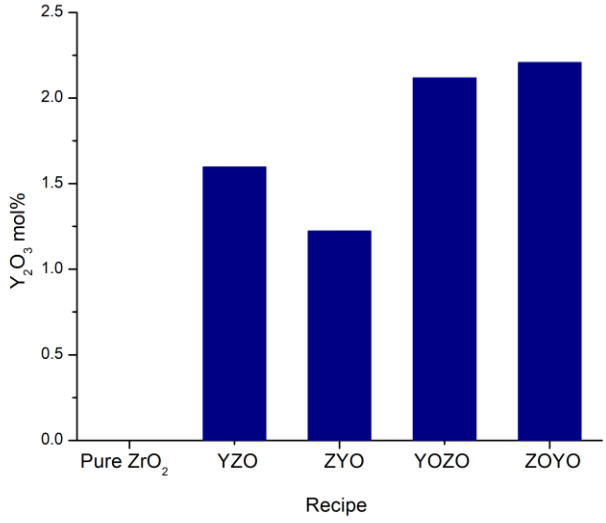

Figure 6.3. The yttrium oxide concentration for different ALD recipes.

The conductivities of each sample were conducted at 400℃, 500℃, and 600℃. Results are shown in Figure 6.4. It can be seen that all samples performed better than the commercial 8YSZ at all test temperatures. The conductivities of YOZO and ZOYO were very close regardless of the test temperature or heat treatment history. However, conductivities of YZO and ZYO were different in all conditions due to the yttrium concentration difference. This shows that the sequence of ZO and YO in the ALD super-cycle does not affect the electrical properties of YSZ thin films with AOBO recipe type; while the effect of pulse sequence (zirconium or yttrium precursor being introduced first) in ABO recipe type is significant.

(a)

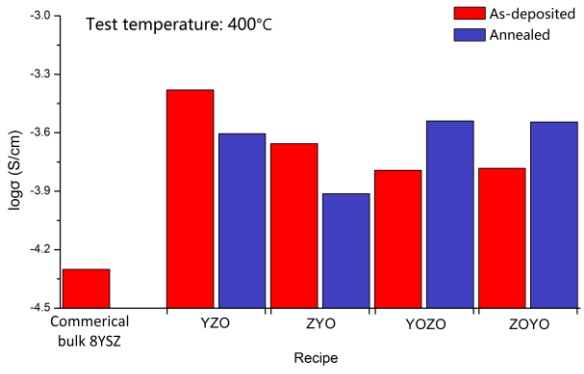

(b)

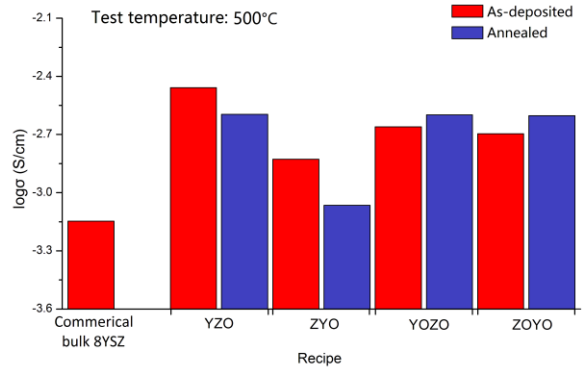

(c)

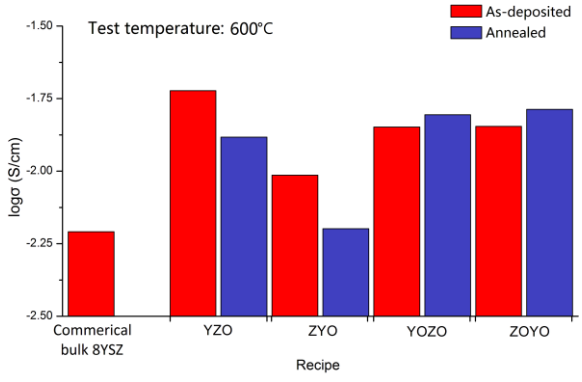

Figure 6.4. Ionic conductivities of both as-deposited and annealed YSZ thin films with different ALD recipes and commercial bulk 8YSZ at 400°C (a), 500°C (b), and 600°C (c).

It is noteworthy that the YZO sample showed the highest ionic conductivity among as-deposited samples at all test temperatures. However, it is not the case for annealed samples. After annealing, conductivities of YOZO and ZOYO increased and became the highest; while ZYO and YZO samples showed reduced conductivities. It can be explained by the finding in Son‘s work [8] that the distribution of yttrium oxide in as-deposited ZOYO or YOZO samples is inhomogeneous. Therefore, annealing homogenized the yttrium oxide distribution, leading to higher conductivities. On the contrary, the yttrium oxide distribution in as-deposited YZO or ZYO is homogeneous. The effect of annealing on YZO and ZYO thin films would be merely grain growth. As a result, as discussed in a previous chapter, as the grain size increased and the true size effect became weaker, and consequently the conductivity decreased.

In addition, at 400℃, as-deposited ZYO showed a higher conductivity than that of YOZO or ZOYO. When the test temperature increased from 500℃ to 600℃, the conductivities of as-deposited ZYO became lower than that of YOZO and ZOYO. During testing the YOZO and ZOYO thin films were annealed and the yttrium oxide was partially homogenized. This is shown by the fact that the increase of ionic conductivity of YOZO and ZOYO after annealing was less when the test temperature is at 500℃ and 600℃ than at 400℃. An Arrhenius plot of the measured ionic conductivities is shown in Figure 6.5, with data of 4YSZ and 2YSZ in literature [8, 35] added for comparison. The yttrium oxide

concentration in YSZ thin films from Ramamoorthy's work [35] is very close to that of YSZ thin films in this study. It is clear from Figure 6.5 that the performance of our YSZ thin films is better regardless of annealing condition. 4YSZ from Son's work [8] showed a higher conductivity level when the test temperature is higher than 500℃, and its conductivity became lower than that of our YSZ thin films at lower test temperatures. This indicates that the 4YSZ in Son's study [8] has a higher activation energy of 1.26 eV.

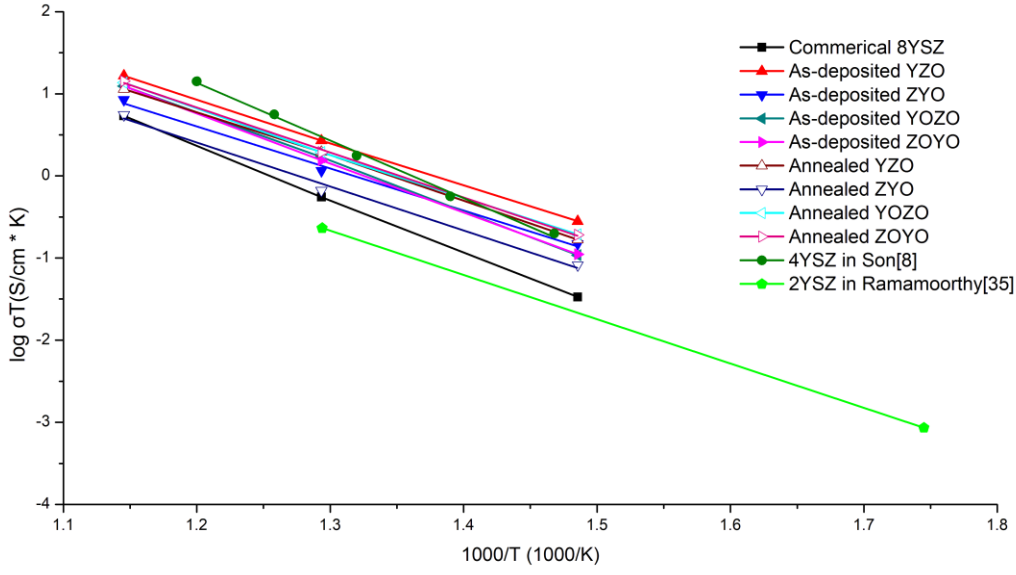

Figure 6.5. Arrhenius plot of the measured ionic conductivities of YSZ thin film samples with different ALD recipes in comparison with reference data [8, 35].

The activation energies of YSZ thin films in our study are summarized in Table 6.2. The activation energy of 2YSZ in Ramamoorthy's work [35] is 0.98

eV, similar with those of as-deposited YZO and ZYO samples. It can be seen that the activation energies of YZO and ZYO samples increased after annealing; while those of YOZO and ZOYO sample decreased. After annealing, activation energies of all four samples were very close. The variation of activation energies indicates that the conduction mechanism changed. This will be discussed more in the following sections.

Table 6.2. Summary of activation energies of oxygen ionic conductance.

	YZO	**ZYO**	**YOZO**	**ZOYO**	**Commercial 8YSZ**
As-deposited sample	1.03eV	1.02eV	1.2eV	1.19eV	1.28eV
Annealed sample	1.07eV	1.06eV	1.08eV	1.09eV	-

6.3.3 Microstructural and crystallinity characterization

X-ray diffraction results are shown in Figure 6.6 for both as-deposited and annealed ALD YSZ thin films. All samples exhibited good crystalline diffraction patterns. As we discussed in the previous chapter, it is misleading to conclude they are cubic phase or tetragonal phase because all the peaks of zirconia cubic diffraction pattern exist in the tetragonal phase diffraction pattern. Also, two peaks at ~28° and ~32° appeared in some of the XRD patterns, which match peaks in the monoclinic phase patter [37]. However, in the raw data the intensity

of these two peaks is comparable to the noise's intensity. They are possibly just noise. It is noteworthy that in the annealed YOZO sample, the peak at ~30° became very weak, indicating the possible existence of preferred orientation.

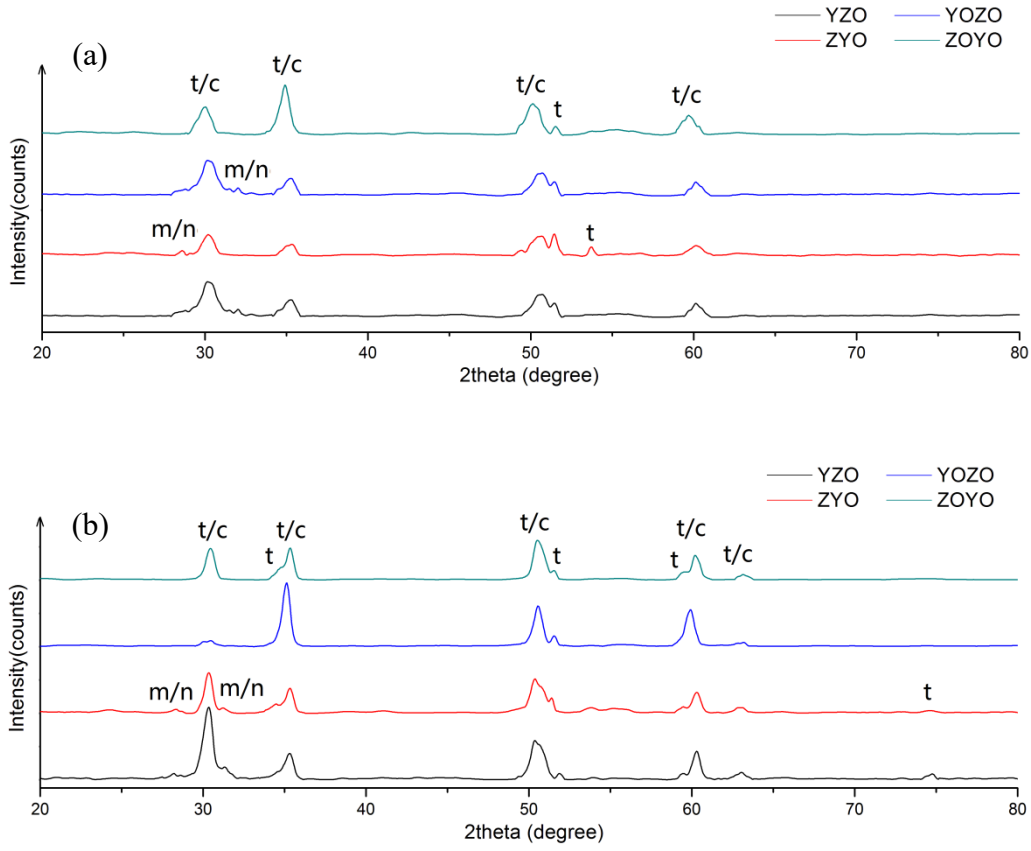

Figure 6.6 XRD patterns of (a) as-deposited and (b) annealed samples.

The roughness of each sample was obtained from AFM measurements, as summarized in Table 6.3. Smooth surfaces were observed for all as-deposited samples with roughness <1 nm, which has been widely observed due to ALD's

self-limiting nature. ALD YSZ thin films in the investigations of Shim [16] and Kim [22] exhibited higher RMS roughness of 1.5 nm [16] and 1.79 nm [22], respectively. The higher deposition temperature of 250℃ is considered to be responsible for this variation. After annealing, roughness in all samples increased significantly due to grain growth.

Table 6.3. Roughness and grain size of as-deposited and annealed samples.

# of cycles		YZO	ZYO	YOZO	ZOYO
RMS roughness (nm)	As-dep.	0.782	0.582	0.592	0.563
	Annealed	2.32	2.58	3.85	2.68
Grain size (nm)	As-dep.	24.8±0.6	23.8±0.9	15.4±0.4	15.2±0.5
	Annealed	50.7±1.7	50.6±1.7	54.7±2.8	53.5±3.3

Topographical 3D images of as-deposited and annealed YZO and YOZO samples are shown in Figure 6.7(a). In Figure 6.7(b), the tapping phase pattern AFM results are shown from which the grain size values were calculated and summarized in Table 6.3. As-deposited YZO and ZYO samples had larger grain size than that of YOZO and ZOYO samples. A possible explanation for this could be that the grain growth in YOZO and ZOYO samples was hindered due to the segregation of zirconium oxide and yttrium oxide in YSZ thin films. According to Zener grain boundary pinning theory [36], higher boundary

energies yield larger pinning pressures. The boundary energies in YOZO and ZOYO samples are higher than in YZO and ZYO samples due to heterogeneous nucleation in YZO and ZYO samples. Consequently, grain size is smaller in YOZO and ZOYO samples.

It is observed that there is a significant increase in grain size after the annealing process. All annealed samples exhibited similar grain size as shown in Table 6.3. This occurs due to the annealing homogenization of the yttrium oxide distribution. For YZO and ZYO samples, grain size growth diminished the true size effect to some extent, leading to higher activation energies. For YOZO and ZOYO samples, annealing introduced a homogeneous distribution of yttrium oxide in YSZ thin films, and this improving effect is dominant over the negative effects of grain growth on the true size effect. Therefore, as noted in section 6.3B, YZO and ZYO experienced a decrease in conductivity and an increase in activation energy after annealing; while the opposite effect was observed for YOZO and ZOYO samples.

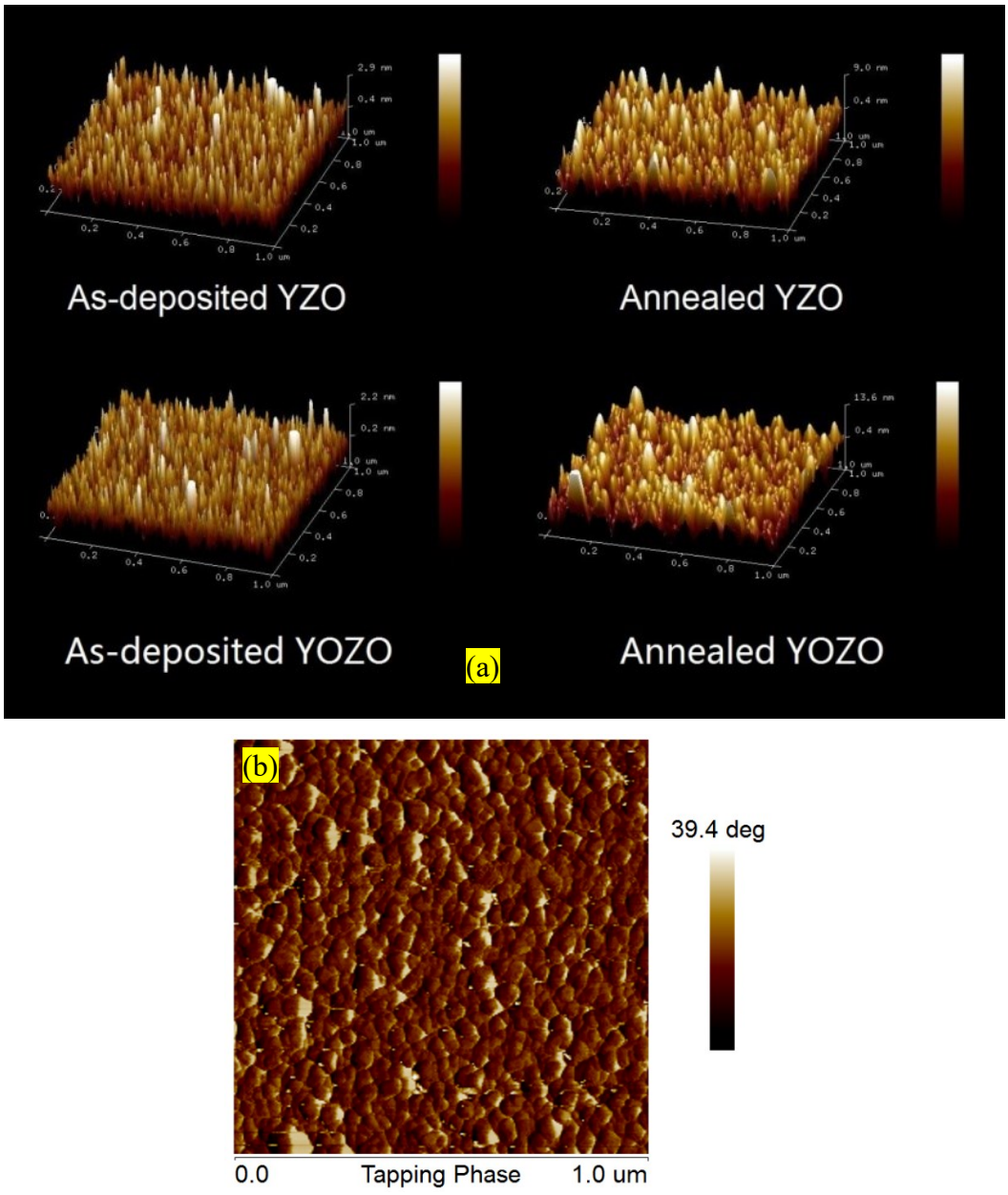

Figure 6.7. AFM results. (a) Topographical 3D images of as-deposited and annealed YZO and YOZO samples; (b) Tapping phase pattern of annealed YOZO sample.

6.4 Conclusions

YSZ thin films with four different ALD recipes were fabricated and evaluated in terms of their microstructure by AFM, crystallinity by XRD, refractive indices by ellipsometry, and conductivity from 400℃ to 600℃. All YSZ thin films, regardless of the recipe being used, exhibited a smooth surface, dense nano-crystalline structure, and good electrical performance. Recipe YOZO and ZOYO produced YSZ thin films without any significant difference. Yttrium oxide concentrations in these two samples were higher because the growth of zirconium oxide is inhibited when deposited on yttrium oxide. The distribution of yttrium oxide in as-deposited samples with the AOBO recipe is inhomogeneous, leading to a smaller grain size due to heterogeneous distribution hindered grain growth.

All samples showed outstanding electrical performance, better than the reference commercial bulk 8YSZ and some data in the literature. For the AOBO recipe samples, annealing is necessary to homogenize the distribution of yttrium oxide and achieve a high conductivity. In contrast, annealing decreases the conductivity of ABO recipe samples due to the decrease in the true size effect resulting from grain growth. The highest conductivity was achieved for conductivity tests performed at low temperature on unannealed YZO recipe samples.

6.5 References

[1] Goodenough, J. B. (2003). Oxide-ion electrolytes. Annual review of materials research, 33(1), 91-128.

[2] Stambouli, A. B., & Traversa, E. (2002). Solid oxide fuel cells (SOFCs): a review of an environmentally clean and efficient source of energy. Renewable and sustainable energy reviews, 6(5), 433-455.

[3] Hui, S. R., Roller, J., Yick, S., Zhang, X., Deces-Petit, C., Xie, Y., ... & Ghosh, D. (2007). A brief review of the ionic conductivity enhancement for selected oxide electrolytes. Journal of Power Sources, 172(2), 493-502.

[4] Wu, F., Wu, J. N., Banerjee, S., Blank, O., & Banerjee, P. (2013). Frontiers in applied atomic layer deposition (ALD) research. In Materials Science Forum (Vol. 736, pp. 147-182). Trans Tech Publications.

[5] Larminie, J., Dicks, A., & McDonald, M. S. (2003). Fuel cell systems explained (Vol. 2). Chichester, UK: J. Wiley.

[6] Foroughi-Abari, A., & Cadien, K. (2012). Atomic layer deposition for nanotechnology. In Nanofabrication (pp. 143-161). Springer Vienna.

[7] Putkonen, M., Sajavaara, T., Niinistö, J., Johansson, L. S., & Niinistö, L. (2002). Deposition of yttria-stabilized zirconia thin films by atomic layer epitaxy from β-diketonate and organometallic precursors. Journal of Materials Chemistry, 12(3), 442-448.

[8] Sik Son, K., Bae, K., Woo Kim, J., Suk Ha, J., & Hyung Shim, J. (2013). Ion conduction in nanoscale yttria-stabilized zirconia fabricated by atomic layer deposition with various doping rates. Journal of Vacuum Science & Technology A: Vacuum, Surfaces, and Films, 31(1), 01A107.

[9] Chao, C. C., Kim, Y. B., & Prinz, F. B. (2009). Surface modification of yttria-stabilized zirconia electrolyte by atomic layer deposition. Nano letters, 9(10), 3626-3628.

[10] Chao, C. C., Park, J. S., Tian, X., Shim, J. H., Gür, T. M., & Prinz, F. B. (2013). Enhanced oxygen exchange on surface-engineered yttria-stabilized zirconia. ACS nano, 7(3), 2186-2191.

[11] Koo, J., Li, Y. K., Choi, H. J., Neoh, K. C., Jang, D. Y., & Shim, J. H. (2016, September). High-Performance Low-Temperature Solid Oxide Fuel Cells By Atomic Layer Deposition of Yttria-Stabilized Zirconia on Silver Cathode. In Meeting Abstracts (No. 39, pp. 2900-2900). The Electrochemical Society.

[12] Bernay, C., Ringuedé, A., Colomban, P., Lincot, D., & Cassir, M. (2003). Yttria-doped zirconia thin films deposited by atomic layer deposition ALD: a structural, morphological and electrical characterisation. Journal of Physics and Chemistry of Solids, 64(9), 1761-1770.

[13] Bae, K., Son, K. S., Kim, J. W., Park, S. W., An, J., Prinz, F. B., & Shim, J. H. (2014). Proton incorporation in yttria-stabilized zirconia during atomic

layer deposition. International Journal of Hydrogen Energy, 39(6), 2621-2627.

[14] Son, K. S., Bae, M. Y., Bae, K., Ha, J. S., & Shim, J. H. (2012). Incorporation of hydroxyl ions and protons in oxide ion vacancies in nanoscale yttria stabilized zirconia during atomic layer deposition. ECS Transactions, 45(1), 155-160.

[15] Chao, C. C., Hsu, C. M., Cui, Y., & Prinz, F. B. (2011). Improved solid oxide fuel cell performance with nanostructured electrolytes. ACS nano, 5(7), 5692-5696.

[16] Shim, J. H., Chao, C. C., Huang, H., & Prinz, F. B. (2007). Atomic layer deposition of yttria-stabilized zirconia for solid oxide fuel cells. Chemistry of Materials, 19(15), 3850-3854.

[17] Park, J. S., Kim, Y. B., Shim, J. H., Kang, S., Gür, T. M., & Prinz, F. B. (2010). Evidence of proton transport in atomic layer deposited yttria-stabilized zirconia films. Chemistry of Materials, 22(18), 5366-5370.

[18] Huang, H., Shim, J. H., Chao, C. C., Pornprasertsuk, R., Sugawara, M., Gür, T. M., & Prinz, F. B. (2009). Characteristics of oxygen reduction on nanocrystalline YSZ. Journal of The Electrochemical Society, 156(3), B392-B396.

[19] Hong, S., Bae, J., Koo, B., & Kim, Y. B. (2014). High-performance ultra-thin film solid oxide fuel cell using anodized-aluminum-oxide supporting structure. Electrochemistry Communications, 47, 1-4.

[20] Jang, D. Y., Kim, H., Bae, K., Schlupp, M. V., Prestat, M., & Shim, J. H. (2013). Performance of Atomic-Layer-Deposited Yttria-Stabilized Zirconia Near Room Temperature. ECS Transactions, 57(1), 1103-1106.

[21] Jang, D. Y., Kim, H. K., Kim, J. W., Bae, K., Schlupp, M. V., Park, S. W., ... & Shim, J. H. (2015). Low-temperature performance of yttria-stabilized zirconia prepared by atomic layer deposition. Journal of Power Sources, 274, 611-618.

[22] Kim, H. K., Jang, D. Y., Kim, J. W., Bae, K., & Shim, J. H. (2015). Ionic properties of ultrathin yttria-stabilized zirconia thin films fabricated by atomic layer deposition with water, oxygen, and ozone. Thin Solid Films, 589, 441-445.

[23] Tanveer, W. H., Ji, S., Yu, W., Cho, G. Y., Lee, Y. H., & Cha, S. W. (2015). Intermediate-temperature solid-oxide fuel cells with a gadolinium-doped ceria anodic functional layer deposited via radio-frequency sputtering. Journal of nanoscience and nanotechnology, 15(11), 8926-8930.

[24] Tanveer, W. H., Ji, S., Yu, W., & Cha, S. W. (2015). Characterization of atomic layer deposited and sputtered yttria-stabilized-zirconia thin films for

low-temperature solid oxide fuel cells. International Journal of Precision Engineering and Manufacturing, 16(10), 2229-2234.

[25] Ha, S., Su, P. C., & Cha, S. W. (2013). Combinatorial deposition of a dense nano-thin film YSZ electrolyte for low temperature solid oxide fuel cells. Journal of Materials Chemistry A, 1(34), 9645-9649.

[26] Jee, Y., Cho, G. Y., An, J., Kim, H. R., Son, J. W., Lee, J. H., ... & Cha, S. W. (2014). High performance Bi-layered electrolytes via atomic layer deposition for solid oxide fuel cells. Journal of Power Sources, 253, 114-122.

[27] Yu, W., Ji, S., Cho, G. Y., Noh, S., Tanveer, W. H., An, J., & Cha, S. W. (2015). Atomic layer deposition of ultrathin blocking layer for low-temperature solid oxide fuel cell on nanoporous substrate. Journal of Vacuum Science & Technology A: Vacuum, Surfaces, and Films, 33(1), 01A145.

[28] Paek, J. Y., Chang, I., Park, J. H., Ji, S., & Cha, S. W. (2014). A study on properties of yttrium-stabilized zirconia thin films fabricated by different deposition techniques. Renewable Energy, 65, 202-206.

[29] Ji, S., Cho, G. Y., Yu, W., Su, P. C., Lee, M. H., & Cha, S. W. (2015). Plasma-enhanced atomic layer deposition of nanoscale yttria-stabilized zirconia electrolyte for solid oxide fuel cells with porous substrate. ACS applied materials & interfaces, 7(5), 2998-3002.

[30] Cha, S. W., Cho, G. Y., Lee, Y., Park, T., Kim, Y., & Lee, J. M. (2016). Effects of carbon contaminations on Y 2 O 3-stabilized ZrO 2 thin film electrolyte prepared by atomic layer deposition for thin film solid oxide fuel cells. CIRP Annals-Manufacturing Technology, 65(1), 515-518.

[31] Park, T., Cho, G. Y., Lee, Y. H., Tanveer, W. H., Yu, W., Lee, Y., ... & Cha, S. W. (2016). Effect of anode morphology on the performance of thin film solid oxide fuel cell with PEALD YSZ electrolyte. International Journal of Hydrogen Energy, 41(22), 9638-9643.

[32] Lecordier, L. (2015). Atomic Layer Deposition and in-Situ Characterization of Yttrium Oxide and Yttria-Stabilized Zirconia. ECS Transactions, 69(7), 109-116.

[33] Puurunen, R. L. (2005). Surface chemistry of atomic layer deposition: A case study for the trimethylaluminum/water process. Journal of applied physics, 97(12), 9.

[34] Xiao, Q. L., Xu, C., Shao, S. Y., Shao, J. D., & Fan, Z. X. (2008). Y2O3 stabilized ZrO2 thin films deposited by electron-beam evaporation: Optical properties, structure and residual stresses. Vacuum, 83(2), 366-371.

[35] Ramamoorthy, R., Sundararaman, D., & Ramasamy, S. (1999). Ionic conductivity studies of ultrafine-grained yttria stabilized zirconia polymorphs. Solid State Ionics, 123(1), 271-278.

[36] Doherty, R. D., Hughes, D. A., Humphreys, F. J., Jonas, J. J., Jensen, D. J., Kassner, M. E., ... & Rollett, A. D. (1997). Current issues in recrystallization: a review. Materials Science and Engineering: A, 238(2), 219-274.

[37] Srinivasan, R., De Angelis, R. J., Ice, G., & Davis, B. H. (1991). Identification of tetragonal and cubic structures of zirconia using synchrotron x-radiation source. Journal of materials research, 6(6), 1287-1292.

Chapter 7

Conclusions and Contributions to Knowledge

- Y_2O_3 PEALD using low vapor pressure yittria precursors was experimentally investigated, and a calculation based on Knudsen effusion and sublimation was introduced to describe the variation of precursor pressures inside the ampoule. The results showed that low vapor pressure precursors (in conventional ampoules) can be used to fabricate composite materials with low concentration components.
- Nano-crystalline YSZ thin films with homogeneously distributed Y_2O_3 dopants were successfully made by PEALD with recipe YZO at substrate temperature of 150℃. GPCs obtained were from 1.15 Å/cycle to 1.35 Å/cycle. High refractive indices (2.15 to 2.3 at 550nm) confirmed thin films' optical quality.
- YZO recipe samples exhibited good electrical performance. YSZ thin films with 1.6 mol% Y_2O_3 showed the highest oxygen ionic conductivity (0.2 S/cm at 600℃) with low activation energy (0.98 eV obtained from 400℃ to 600℃). The strong true size effect with wide space charge layers is considered responsible for this outstanding performance.

- Higher thickness from longer ALD cycles and processing time coarsened the grain size of YSZ thin films, leading to a weakened true size effect. Consequently, conductivities of samples reduced with increasing film thickness.
- The effect of ALD recipe setups on the structure and property of YSZ composite thin films was investigated. Four groups of recipes (YZO, ZYO, YOZO, ZOYO) were considered. All recipes yielded dense nano-crystalline structure, showing better performance than the commercial bulk 8YSZ reference.
- YZO and ZYO samples showed different Y_2O_3 concentrations (1.6 mol% and 1.2 mol% for YZO and ZYO, respectively) due to the fact that the first pulse in the ALD cycle occupied more available adsorption sites.
- YOZO and ZOYO samples exhibited similar Y_2O_3 concentrations (~1.6 mol%). The order of ALD cycles of zirconium or yttrium in the ALD super-cycle does not affect the adsorption of precursors.
- After annealing, the ionic conductivity of YZO and ZYO samples decreased and that of YOZO and ZOYO samples increased. Annealing weakened the true size of YZO and ZYO samples, while it homogenized the distribution of Y_2O_3 in YOZO and ZOYO samples. This is supported by the change in the samples' activation energies before and after annealing.

Chapter 8

Future Directions

In this thesis, a calculation based on Knudsen effusion and sublimation was introduced to describe the variation of precursor pressures inside the ampoule. In this calculation, the carrier gas Ar was assumed to not affect the effusion of precursor molecules. However, the calculated results would be more accurate if the effect of carrier gas was considered. In addition, to complete the systematic simulation of ALD process, the modeling of mass transfer from ampoule to reaction chamber and adsorption of precursor materials on substrates would be of interest.

The concentration of Y_2O_3 in PEALD YSZ thin films was lower than 2 mol%. Although their ionic conductivities and activation energies are better than those of many YSZ thin films in literature, a study of higher concentration Y_2O_3 YSZ thin films would clarify if 2YSZ exhibits the highest conductivity for nano-crystalline YSZ thin films with homogeneously distributed Y_2O_3.

We only qualitatively explained the difference of ALD recipe YZO, ZYO, YOZO, and ZOYO. A quantitative analysis would be of interest. A calculation based on theory of precursor molecules adsorption would illustrate the material growth in each recipe thermodynamically and kinetically.

In the electrical test, we only measured C-V characteristic of the PEALD YSZ thin films on silicon wafer samples at 400℃ to 600℃. Extending the measurement temperature to 300℃ or 200℃ can be interesting. Also, measurement of a fuel cell operating using electrochemical impedance spectroscopy (EIS) can be helpful in investigating the in-service performance of these thin film electrolytes and in understanding the conduction mechanism since the conductivity of grain and grain boundary can be separated in EIS measurements.

Bibliography

Alarcon-Flores, G., Aguilar-Frutis, M. I. G. U. E. L., García-Hipolito, M. A. N. U. E. L., Guzman-Mendoza, J., Canseco, M. A., & Falcony, C. (2008). Optical and structural characteristics of Y2O3 thin films synthesized from yttrium acetylacetonate. Journal of Materials Science, 43(10), 3582-3588.

Aoki, M., Chiang, Y. M., Kosacki, I., Lee, L., Tuller, H., & Liu, Y. (1996). Solute Segregation and Grain-Boundary Impedance in High-Purity Stabilized Zirconia. Journal of the American ceramic society, 79(5), 1169-1180.

Bae, K., Son, K. S., Kim, J. W., Park, S. W., An, J., Prinz, F. B., & Shim, J. H. (2014). Proton incorporation in yttria-stabilized zirconia during atomic layer deposition. International Journal of Hydrogen Energy, 39(6), 2621-2627.

Bardal, A., Eibl, O., Matthee, T., Friedl, G., & Wecker, J. (1993). High-resolution electron microscopy of epitaxial YBCO/Y2O3/YSZ on Si (001). Journal of materials research, 8(09), 2112-2127.

Beckel, D., Bieberle-Hütter, A., Harvey, A., Infortuna, A., Muecke, U. P., Prestat, M., ... & Gauckler, L. J. (2007). Thin films for micro solid oxide fuel cells. Journal of Power Sources, 173(1), 325-345.

Bernay, C., Ringuedé, A., Colomban, P., Lincot, D., & Cassir, M. (2003). Yttria-doped zirconia thin films deposited by atomic layer deposition ALD: a structural, morphological and electrical characterisation. Journal of Physics and Chemistry of Solids, 64(9), 1761-1770.

Boulc'h, F., Djurado, E., & Dessemond, L. (2004). Dopant segregation and space charge effect in nanostructured tetragonal zirconia. Journal of The Electrochemical Society, 151(8), A1210-A1215.

Brett, D. J., Atkinson, A., Brandon, N. P., & Skinner, S. J. (2008). Intermediate temperature solid oxide fuel cells. Chemical Society Reviews, 37(8), 1568-1578.

Brossmann, U., Knoner, G., Schaefer, H. E., & Wurschum, R. (2004). Oxygen diffusion in nanocrystalline ZrO 2. Reviews on Advanced Materials Science, 6(1), 7-11.

Callister, William D., (2009). Materials Science and Engineering: An Introduction, 8th Edition. Wiley.

Cha, S. W., Cho, G. Y., Lee, Y., Park, T., Kim, Y., & Lee, J. M. (2016). Effects of carbon contaminations on Y 2 O 3-stabilized ZrO 2 thin film electrolyte prepared by atomic layer deposition for thin film solid oxide fuel cells. CIRP Annals-Manufacturing Technology, 65(1), 515-518.

Chang, J. P., Lin, Y. S., & Chu, K. (2001). Rapid thermal chemical vapor deposition of zirconium oxide for metal-oxide-semiconductor field effect transistor application. Journal of Vacuum Science & Technology B: Microelectronics and Nanometer Structures Processing, Measurement, and Phenomena, 19(5), 1782-1787.

Chao, C. C., Hsu, C. M., Cui, Y., & Prinz, F. B. (2011). Improved solid oxide fuel cell performance with nanostructured electrolytes. ACS nano, 5(7), 5692-5696.

Chao, C. C., Kim, Y. B., & Prinz, F. B. (2009). Surface modification of yttria-stabilized zirconia electrolyte by atomic layer deposition. Nano letters, 9(10), 3626-3628.

Chao, C. C., Park, J. S., Tian, X., Shim, J. H., Gür, T. M., & Prinz, F. B. (2013). Enhanced oxygen exchange on surface-engineered yttria-stabilized zirconia. ACS nano, 7(3), 2186-2191.

Cheikh, A., Madani, A., Touati, A., Boussetta, H., & Monty, C. (2001). Ionic conductivity of zirconia based ceramics from single crystals to

nanostructured polycrystals. Journal of the European Ceramic Society, 21(10), 1837-1841.

Chen, X. J., Khor, K. A., Chan, S. H., & Yu, L. G. (2002). Influence of microstructure on the ionic conductivity of yttria-stabilized zirconia electrolyte. Materials Science and Engineering: A, 335(1), 246-252.

Cho, G. Y., Noh, S., Lee, Y. H., Ji, S., & Cha, S. W. (2014). Study of Y2O3 thin film prepared by plasma enhanced atomic layer deposition. ECS Transactions, 64(9), 15-21.

De Souza, R. A., Pietrowski, M. J., Anselmi-Tamburini, U., Kim, S., Munir, Z. A., & Martin, M. (2008). Oxygen diffusion in nanocrystalline yttria-stabilized zirconia: the effect of grain boundaries. Physical Chemistry Chemical Physics, 10(15), 2067-2072.

Doherty, R. D., Hughes, D. A., Humphreys, F. J., Jonas, J. J., Jensen, D. J., Kassner, M. E., ... & Rollett, A. D. (1997). Current issues in recrystallization: a review. Materials Science and Engineering: A, 238(2), 219-274.

Durá, O. J., de la Torre, M. L., Vázquez, L., Chaboy, J., Boada, R., Rivera-Calzada, A., ... & Leon, C. (2010). Ionic conductivity of nanocrystalline yttria-stabilized zirconia: Grain boundary and size effects. Physical review B, 81(18), 184301.

Elam, J. W., & George, S. M. (2003). Growth of ZnO/Al2O3 alloy films using atomic layer deposition techniques. Chemistry of Materials, 15(4), 1020-1028.

Elam, J. W., Dasgupta, N. P., & Prinz, F. B. (2011). ALD for clean energy conversion, utilization, and storage. Mrs Bulletin, 36(11), 899-906.

Fabbri, E., Pergolesi, D., & Traversa, E. (2010). Ionic conductivity in oxide heterostructures: the role of interfaces. Science and Technology of Advanced Materials, 11(5), 054503.

Foroughi-Abari, A., & Cadien, K. (2012). Atomic layer deposition for nanotechnology. In Nanofabrication (pp. 143-161). Springer Vienna.

Fujiwara, H. (2007). Spectroscopic ellipsometry: principles and applications. John Wiley & Sons.

Fukumoto, H., Imura, T., & Osaka, Y. (1989). Heteroepitaxial growth of Y2O3 films on silicon. Applied Physics Letters, 55(4), 360-361.

George, S. M. (2009). Atomic layer deposition: an overview. Chemical reviews, 110(1), 111-131.

Gilardi, E. (2016). Interface effects in Y2Zr2O7 thin films.

Goodenough, J. B. (2003). Oxide-ion electrolytes. Annual review of materials research, 33(1), 91-128.

Guo, X., & Maier, J. (2001). Grain boundary blocking effect in zirconia: a Schottky barrier analysis. Journal of the Electrochemical Society, 148(3), E121-E126.

Ha, S., Su, P. C., & Cha, S. W. (2013). Combinatorial deposition of a dense nano-thin film YSZ electrolyte for low temperature solid oxide fuel cells. Journal of Materials Chemistry A, 1(34), 9645-9649.

Haugstad, Greg. (2012). Atomic force microscopy: understanding basic modes and advanced applications. John Wiley & Sons.

Heiroth, S., Ghisleni, R., Lippert, T., Michler, J., & Wokaun, A. (2011). Optical and mechanical properties of amorphous and crystalline yttria-stabilized zirconia thin films prepared by pulsed laser deposition. Acta Materialia, 59(6), 2330-2340.

Hirai, T., Teramoto, K., Koike, H., Nagashima, K., & Tarui, Y. (1997). Initial stage and growth process of ceria, yttria-stabilized-zirconia and ceria-zirconia mixture thin films on Si (100) surfaces. Japanese journal of applied physics, 36(8R), 5253.

Hollahan, J. R. (1962). Molecular effusion: Its newer features and applications. J. Chem. Educ, 39(1), 23.

Hong, S., Bae, J., Koo, B., & Kim, Y. B. (2014). High-performance ultra-thin film solid oxide fuel cell using anodized-aluminum-oxide supporting structure. Electrochemistry Communications, 47, 1-4.

https://www.electronics-airliquide.com/our-brands/aloha

Huang, H., Shim, J. H., Chao, C. C., Pornprasertsuk, R., Sugawara, M., Gür, T. M., & Prinz, F. B. (2009). Characteristics of oxygen reduction on nanocrystalline YSZ. Journal of The Electrochemical Society, 156(3), B392-B396.

Hui, S. R., Roller, J., Yick, S., Zhang, X., Deces-Petit, C., Xie, Y., ... & Ghosh, D. (2007). A brief review of the ionic conductivity enhancement for selected oxide electrolytes. Journal of Power Sources, 172(2), 493-502.

Ivers-Tiffée, E., Weber, A., & Herbstritt, D. (2001). Materials and technologies for SOFC-components. Journal of the European Ceramic Society, 21(10), 1805-1811.

Jang, D. Y., Kim, H. K., Kim, J. W., Bae, K., Schlupp, M. V., Park, S. W., ... & Shim, J. H. (2015). Low-temperature performance of yttria-stabilized zirconia prepared by atomic layer deposition. Journal of Power Sources, 274, 611-618.

Jang, D. Y., Kim, H., Bae, K., Schlupp, M. V., Prestat, M., & Shim, J. H. (2013). Performance of Atomic-Layer-Deposited Yttria-Stabilized Zirconia Near Room Temperature. ECS Transactions, 57(1), 1103-1106.

Jee, Y., Cho, G. Y., An, J., Kim, H. R., Son, J. W., Lee, J. H., ... & Cha, S. W. (2014). High performance Bi-layered electrolytes via atomic layer deposition for solid oxide fuel cells. Journal of Power Sources, 253, 114-122.

Ji, S., Cho, G. Y., Yu, W., Su, P. C., Lee, M. H., & Cha, S. W. (2015). Plasma-enhanced atomic layer deposition of nanoscale yttria-stabilized zirconia electrolyte for solid oxide fuel cells with porous substrate. ACS applied materials & interfaces, 7(5), 2998-3002.

Karthikeyan, A., Chang, C. L., & Ramanathan, S. (2006). High temperature conductivity studies on nanoscale yttria-doped zirconia thin films and size effects. Applied physics letters, 89(18), 183116.

Kim, H. K., Jang, D. Y., Kim, J. W., Bae, K., & Shim, J. H. (2015). Ionic properties of ultrathin yttria-stabilized zirconia thin films fabricated by atomic layer deposition with water, oxygen, and ozone. Thin Solid Films, 589, 441-445.

Kim, S., Jain, P., Avila-Paredes, H. J., Thron, A., van Benthem, K., & Sen, S. (2010). Strong immobilization of charge carriers near the surface of a solid oxide electrolyte. Journal of Materials Chemistry, 20(19), 3855-3858.

Knöner, G., Reimann, K., Röwer, R., Södervall, U., & Schaefer, H. E. (2003). Enhanced oxygen diffusivity in interfaces of nanocrystalline ZrO2· Y2O3. Proceedings of the National Academy of Sciences, 100(7), 3870-3873.

Koo, J., Li, Y. K., Choi, H. J., Neoh, K. C., Jang, D. Y., & Shim, J. H. (2016, September). High-Performance Low-Temperature Solid Oxide Fuel Cells By Atomic Layer Deposition of Yttria-Stabilized Zirconia on Silver Cathode. In Meeting Abstracts (No. 39, pp. 2900-2900). The Electrochemical Society.

Korte, C., Schichtel, N., Hesse, D., & Janek, J. (2009). Influence of interface structure on mass transport in phase boundaries between different ionic materials. Monatshefte für Chemie-Chemical Monthly, 140(9), 1069-1080.

Kosacki, I., Rouleau, C. M., Becher, P. F., Bentley, J., & Lowndes, D. H. (2005). Nanoscale effects on the ionic conductivity in highly textured YSZ thin films. Solid State Ionics, 176(13), 1319-1326.

Kosacki, I., Suzuki, T., Petrovsky, V., & Anderson, H. U. (2000). Electrical conductivity of nanocrystalline ceria and zirconia thin films. Solid State Ionics, 136, 1225-1233.

Kukli, K., Forsgren, K., Aarik, J., Uustare, T., Aidla, A., Niskanen, A., ... & Hårsta, A. (2001). Atomic layer deposition of zirconium oxide from zirconium tetraiodide, water and hydrogen peroxide. Journal of Crystal Growth, 231(1), 262-272.

Kukli, K., Ritala, M., Pore, V., Leskelä, M., Sajavaara, T., Hegde, R. I., ... & Aspinall, H. C. (2006). Atomic Layer Deposition and Properties of Lanthanum Oxide and Lanthanum-Aluminum Oxide Films. Chemical Vapor Deposition, 12(2-3), 158-164.

Larminie, J., Dicks, A., & McDonald, M. S. (2003). Fuel cell systems explained (Vol. 2). Chichester, UK: J. Wiley.

Lecordier, L. (2015). Atomic Layer Deposition and in-Situ Characterization of Yttrium Oxide and Yttria-Stabilized Zirconia. ECS Transactions, 69(7), 109-116.

Liang, M., Yu, B., Wen, M., Chen, J., Xu, J., & Zhai, Y. (2008). The Fabrication Technique of YSZ Electrolyte Film. Progress in Chemistry, 20(7/8).

Lin, S. S., & Huang, J. L. (2004). Effect of thickness on the structural and optical properties of ZnO films by rf magnetron sputtering. Surface and Coatings Technology, 185(2), 222-227.

Maier, J. (2003). Nano-ionics: Trivial and non-trivial size effects on ion conduction in solids.

Miikkulainen, V., Leskelä, M., Ritala, M., & Puurunen, R. L. (2013). Crystallinity of inorganic films grown by atomic layer deposition: Overview and general trends. Journal of Applied Physics, 113(2), 2.

Miyamoto, S. (1933). A theory of the rate of sublimation. Transactions of the Faraday Society, 29(140), 794-797.

Motamedi, P., Dalili, N., & Cadien, K. (2015). A route to low temperature growth of single crystal GaN on sapphire. Journal of Materials Chemistry C, 3(28), 7428-7436.

Motoyama, M., Chao, C. C., An, J., Jung, H. J., Gür, T. M., & Prinz, F. B. (2013). Nanotubular array solid oxide fuel cell. ACS nano, 8(1), 340-351.

Muneshwar, T., & Cadien, K. (2015). Influence of atomic layer deposition valve temperature on ZrN plasma enhanced atomic layer deposition growth. Journal of Vacuum Science & Technology A: Vacuum, Surfaces, and Films, 33(6), 060603.

Muneshwar, T., & Cadien, K. (2015). Low temperature plasma enhanced atomic layer deposition of conducting zirconium nitride films using tetrakis (dimethylamido) zirconium and forming gas (5% H2+ 95% N2) plasma. Journal of Vacuum Science & Technology A: Vacuum, Surfaces, and Films, 33(3), 031502.

Nigara, Y. (1968). Measurement of the optical constants of yttrium oxide. Japanese Journal of Applied Physics, 7(4), 404.

Niinistö, J., Kukli, K., Sajavaara, T., Ritala, M., Leskelä, M., Oberbeck, L., ... & Schröder, U. (2009). Atomic layer deposition of high-permittivity yttrium-doped HfO2 films. Electrochemical and Solid-State Letters, 12(1), G1-G4.

Niinistö, J., Putkonen, M., & Niinistö, L. (2004). Processing of Y2O3 thin films by atomic layer deposition from cyclopentadienyl-type compounds and water as precursors. Chemistry of materials, 16(15), 2953-2958.

Paek, J. Y., Chang, I., Park, J. H., Ji, S., & Cha, S. W. (2014). A study on properties of yttrium-stabilized zirconia thin films fabricated by different deposition techniques. Renewable Energy, 65, 202-206.

Park, J. S., Kim, Y. B., Shim, J. H., Kang, S., Gür, T. M., & Prinz, F. B. (2010). Evidence of proton transport in atomic layer deposited yttria-stabilized zirconia films. Chemistry of Materials, 22(18), 5366-5370.

Park, T., Cho, G. Y., Lee, Y. H., Tanveer, W. H., Yu, W., Lee, Y., ... & Cha, S. W. (2016). Effect of anode morphology on the performance of thin film solid oxide fuel cell with PEALD YSZ electrolyte. International Journal of Hydrogen Energy, 41(22), 9638-9643.

Peters, A., Korte, C., Hesse, D., Zakharov, N., & Janek, J. (2007). Ionic conductivity and activation energy for oxygen ion transport in superlattices—the multilayer system CSZ (ZrO 2+ CaO)/Al 2 O 3. Solid State Ionics, 178(1), 67-76.

Peters, C. (2009). Grain-size effects in nanoscaled electrolyte and cathode thin films for solid oxide fuel cells (SOFC) (Vol. 15). KIT Scientific Publishing.

Putkonen, M., & Niinistö, L. (2001). Zirconia thin films by atomic layer epitaxy. A comparative study on the use of novel precursors with ozone. Journal of Materials Chemistry, 11(12), 3141-3147.

Putkonen, M., Sajavaara, T., Johansson, L. S., & Niinistö, L. (2001). Low-Temperature ALE Deposition of Y2O3 Thin Films from β-Diketonate Precursors. Chemical Vapor Deposition, 7(1), 44-50.

Putkonen, M., Sajavaara, T., Niinistö, J., Johansson, L. S., & Niinistö, L. (2002). Deposition of yttria-stabilized zirconia thin films by atomic layer epitaxy from β-diketonate and organometallic precursors. Journal of Materials Chemistry, 12(3), 442-448.

Puurunen, R. L. (2005). Surface chemistry of atomic layer deposition: A case study for the trimethylaluminum/water process. Journal of applied physics, 97(12), 9.

Ramamoorthy, R., Sundararaman, D., & Ramasamy, S. (1999). Ionic conductivity studies of ultrafine-grained yttria stabilized zirconia polymorphs. Solid State Ionics, 123(1), 271-278.

Raoufi, D., Kiasatpour, A., Fallah, H. R., & Rozatian, A. S. H. (2007). Surface characterization and microstructure of ITO thin films at different annealing temperatures. Applied Surface Science, 253(23), 9085-9090.

Roessler, T., Gluch, J., Albert, M., & Bartha, J. W. (2010). Electrical characterisation of HfYO MIM-structures deposited by ALD. Thin Solid Films, 518(16), 4680-4683.

RUH, R., Mazdiyasni, K. S., Valentine, P. G., & Bielstein, H. O. (1984). Phase Relations in the System ZrO2-Y2O3 at Low Y2O3 Contents. Journal of the American Ceramic Society, 67(9).

Sardela, M. (Ed.). (2014). Practical Materials Characterization. Springer.

Schichtel, N., Korte, C., Hesse, D., & Janek, J. (2009). Elastic strain at interfaces and its influence on ionic conductivity in nanoscaled solid electrolyte thin films—theoretical considerations and experimental studies. Physical Chemistry Chemical Physics, 11(17), 3043-3048.

Shim, J. H., Chao, C. C., Huang, H., & Prinz, F. B. (2007). Atomic layer deposition of yttria-stabilized zirconia for solid oxide fuel cells. Chemistry of Materials, 19(15), 3850-3854.

Shim, J. H., Kang, S., Cha, S. W., Lee, W., Kim, Y. B., Park, J. S., ... & An, J. (2013). Atomic layer deposition of thin-film ceramic electrolytes for high-performance fuel cells. Journal of Materials Chemistry A, 1(41), 12695-12705.

Shim, J. H., Park, J. S., An, J., Gür, T. M., Kang, S., & Prinz, F. B. (2009). Intermediate-temperature ceramic fuel cells with thin film yttrium-doped barium zirconate electrolytes. Chemistry of Materials, 21(14), 3290-3296.

Sik Son, K., Bae, K., Woo Kim, J., Suk Ha, J., & Hyung Shim, J. (2013). Ion conduction in nanoscale yttria-stabilized zirconia fabricated by atomic layer deposition with various doping rates. Journal of Vacuum Science & Technology A: Vacuum, Surfaces, and Films, 31(1), 01A107.

Son, K. S., Bae, M. Y., Bae, K., Ha, J. S., & Shim, J. H. (2012). Incorporation of hydroxyl ions and protons in oxide ion vacancies in nanoscale yttria stabilized zirconia during atomic layer deposition. ECS Transactions, 45(1), 155-160.

Srinivasan, R., De Angelis, R. J., Ice, G., & Davis, B. H. (1991). Identification of tetragonal and cubic structures of zirconia using synchrotron x-radiation source. Journal of materials research, 6(6), 1287-1292.

Stambouli, A. B., & Traversa, E. (2002). Solid oxide fuel cells (SOFCs): a review of an environmentally clean and efficient source of energy. Renewable and sustainable energy reviews, 6(5), 433-455.

Steele, B. C. H. (1995). Interfacial reactions associated with ceramic ion transport membranes. Solid State Ionics, 75, 157-165.

Steele, B. C., & Heinzel, A. (2001). Materials for fuel-cell technologies. Nature, 414(6861), 345-352.

Su, P. C., & Prinz, F. B. (2012). Nanoscale membrane electrolyte array for solid oxide fuel cells. Electrochemistry Communications, 16(1), 77-79.

Su, P. C., Chao, C. C., Shim, J. H., Fasching, R., & Prinz, F. B. (2008). Solid oxide fuel cell with corrugated thin film electrolyte. Nano letters, 8(8), 2289-2292.

Tanveer, W. H., Ji, S., Yu, W., & Cha, S. W. (2015). Characterization of atomic layer deposited and sputtered yttria-stabilized-zirconia thin films for low-temperature solid oxide fuel cells. International Journal of Precision Engineering and Manufacturing, 16(10), 2229-2234.

Tanveer, W. H., Ji, S., Yu, W., Cho, G. Y., Lee, Y. H., & Cha, S. W. (2015). Intermediate-temperature solid-oxide fuel cells with a gadolinium-doped ceria anodic functional layer deposited via radio-frequency sputtering. Journal of nanoscience and nanotechnology, 15(11), 8926-8930.

Triyoso, D. H., Hegde, R. I., Grant, J. M., Schaeffer, J. K., Roan, D., White Jr, B. E., & Tobin, P. J. (2005). Evaluation of lanthanum based gate dielectrics deposited by atomic layer deposition. Journal of Vacuum Science & Technology B: Microelectronics and Nanometer Structures Processing, Measurement, and Phenomena, 23(1), 288-297.

Tuller, H. L. (2000). Ionic conduction in nanocrystalline materials. Solid State Ionics, 131(1), 143-157.

Watts, J. F., & Wolstenholme, J. (2003). An introduction to surface analysis by XPS and AES. Wiley.

Wiktorczyk, T., Biegański, P., & Serafińczuk, J. (2016). Optical properties of nanocrystalline Y 2 O 3 thin films grown on quartz substrates by electron beam deposition. Optical Materials, 59, 150-156.

Wood, D. L., & Nassau, K. (1982). Refractive index of cubic zirconia stabilized with yttria. Applied Optics, 21(16), 2978-2981.

Wood, D. L., Nassau, K., & Kometani, T. Y. (1990). Refractive index of Y2O3 stabilized cubic zirconia: variation with composition and wavelength. Applied optics, 29(16), 2485-2488.

Wu, F., Wu, J. N., Banerjee, S., Blank, O., & Banerjee, P. (2013). Frontiers in applied atomic layer deposition (ALD) research. In Materials Science Forum (Vol. 736, pp. 147-182). Trans Tech Publications.

Xiao, Q. L., Xu, C., Shao, S. Y., Shao, J. D., & Fan, Z. X. (2008). Y 2 O 3 stabilized ZrO 2 thin films deposited by electron-beam evaporation: Optical properties, structure and residual stresses. Vacuum, 83(2), 366-371.

Xu, R., Selvaraj, S. K., Azimi, N., & Takoudis, C. G. (2013). Growth Characteristics and Properties of Yttrium Oxide Thin Films by Atomic Layer Deposition from Novel Y (iPrCp) 3 Precursor and O3. ECS Transactions, 50(13), 107-116.

Yamamoto, O. (2000). Solid oxide fuel cells: fundamental aspects and prospects. Electrochimica Acta, 45(15), 2423-2435.

Yashima, M., Kakihana, M., & Yoshimura, M. (1996). Metastable-stable phase diagrams in the zirconia-containing systems utilized in solid-oxide fuel cell application. Solid State Ionics, 86, 1131-1149.

Yu, W., Ji, S., Cho, G. Y., Noh, S., Tanveer, W. H., An, J., & Cha, S. W. (2015). Atomic layer deposition of ultrathin blocking layer for low-temperature solid oxide fuel cell on nanoporous substrate. Journal of Vacuum Science & Technology A: Vacuum, Surfaces, and Films, 33(1), 01A145.

Zhang, C., Li, C. J., Zhang, G., Ning, X. J., Li, C. X., Liao, H., & Coddet, C. (2007). Ionic conductivity and its temperature dependence of atmospheric plasma-sprayed yttria stabilized zirconia electrolyte. Materials Science and Engineering: B, 137(1), 24-30.